Friedrich-Alexander-Universität
Faculty of Sciences

Master's thesis

02-03-2026

Frederik Andersen

Supervisors: PD Dr. Thomas Eberl, Dr. Rodrigo Gracia Ruiz

Integration of the NEUT Neutrino Interaction Model into the KM3NeT/ORCA Simulation Framework

Abstract

Neutrino interaction models determine the multiplicity, composition, and kinematics of final-state particles in neutrino-nucleus scattering. The final-state particle content determines the Cherenkov photon yield in the detector and thus sets the reconstructed observables entering the oscillation analysis. Differences between the description of neutrino-matter interactions from different models therefore propagate through the simulation chain up to reconstructed energy-zenith distributions, where subtle distortions encode the oscillation signal.

In the energy range from $\mathcal{O}(1\,\mathrm{GeV})$ to $\mathcal{O}(10\,\mathrm{GeV})$ relevant for the KM3NeT/ORCA, nuclear effects and multi-nucleon processes strongly influence the visible state. Different theoretical assumptions can lead to distinct energy partitions between leptonic and hadronic components and to modified kinematic correlations, even when inclusive cross sections are similar. A detector-specific evaluation is required to quantify their impact.

This thesis investigates generator-dependent effects within the ORCA simulation and reconstruction chain. A key contribution is the integration of the NEUT event generator into the ORCA Monte Carlo framework, otherwise based on the GENIE/`gSeaGen` architecture. The dedicated interface `km3neut` enables event generation followed by identical vertex placement, light simulation, trigger processing, and reconstruction.

Comparisons are performed at generator, light-simulation, and reconstruction level. At generator level, notable differences are observed in inelasticity and hadronic energy distributions in the few-GeV region. Detector effects partially reduce these variations; however, residual shifts persist in reconstructed energy and event-class composition. These distortions potentially modify the reconstructed parameter distribution relevant for oscillation measurements and indicates that generator choice represents a non-negligible systematic input for ORCA analyses.

Contents

1. Introduction

1.1. Neutrinos

Neutrinos are electrically neutral, weakly interacting fermions originally postulated by Pauli in 1930 to restore energy and momentum conservation in beta decays [1]. Following Chadwick's discovery of the neutron [2], Fermi introduced the name "neutrino" and incorporated the particle into his theory of beta decay [3, 4]. Despite Pauli's initial skepticism regarding the experimental detectability of the neutrino [5], the first direct observation of antineutrinos was achieved in 1956 through inverse beta decay reactions [6] by Clyde L. Cowan and Frederick Reines. This landmark discovery was made during Pauli's lifetime and was subsequently recognized with the Nobel Prize in Physics [7].

The subsequent identification of the muon neutrino in 1962 [8, 9] and the tau neutrino in 2000 [10] established the existence of three active neutrino flavors. Precision measurements of the Z^0 boson width at LEP confirmed that only three light neutrino species couple to the weak interaction [11].

A major milestone in neutrino physics was the resolution of the solar neutrino problem. Pioneering radiochemical measurements [12], followed by the Sudbury Neutrino Observatory's observation of flavor conversion [13], established that neutrinos oscillate and hence possess non-zero mass. This discovery, central to modern particle physics, was awarded by the 2015 Nobel Prize [14]. Neutrino oscillations are sensitive to mass ordering, mixing parameters, and potential physics Beyond Standard Model (BSM) [15, 16, 17, 18, 19, 20], motivating experiments capable of precision measurements over a broad energy and baseline range.

Atmospheric neutrinos provide baselines up to the Earth's diameter and energies from a few hundred MeV to several TeV, making them ideal probes of oscillation

phenomena because this broad L/E coverage spans the oscillation maxima and minima for Δm^2_{31} and Δm^2_{21}. For the Kilometer^3 Neutrino Telescope (KM3NeT)/Oscillation Research with Cosmics in the Abyss (ORCA), upward-going neutrinos additionally traverse dense Earth matter, where coherent forward scattering on electrons induces energy- and zenith-dependent resonances in the few-tens of GeV range, enhancing sensitivity to the neutrino mass ordering and to deviations from standard three-flavor mixing.

Extracting oscillation parameters from atmospheric data, however, requires accurate modeling of neutrino-matter interactions, atmospheric fluxes, and detector response. Consequently, the modeling of neutrino-nucleon interactions play a central role in oscillation analyses. Their underlying models describing the physics of the nucleons, the properties of the final states or the cross-sections, introduce systematic uncertainties that are increasingly critical as experiments reach an increasing level in precision.

1.2. KM3NeT

If not otherwise noted information is taken from [21].

KM3NeT is a neutrino observatory under construction in the Mediterranean Sea. Building on the technological heritage of ANTARES [22] and complementing the sky coverage of IceCube [23], KM3NeT is designed to address two core objectives: (i) the detection of high-energy astrophysical neutrinos and (ii) precision measurements of atmospheric neutrino oscillations, including the determination of the neutrino mass ordering.

1.2.1. Detection of Cherenkov Radiation in Seawater

KM3NeT uses Cherenkov radiation to detect charged particles produced in neutrino interactions. When relativistic charged particles traverse a dielectric medium like seawater, Cherenkov radiation is emitted if $\beta \cdot n > 1$, where n is the refractive index

and β the velocity. The emission angle satisfies

$$\cos\theta_C = \frac{1}{\beta n}\,. \tag{1.1}$$

For seawater ($n \simeq 1.33$), relativistic particles produce a characteristic cone with $\theta_C \approx 41°$. The effect is interpreted as the coherent superposition of wavefronts generated as the medium becomes polarized by the passing particle, forming a propagating shock front [24]. Cherenkov light, primarily in the blue and UV region, is detected by arrays of Photomultiplier Tubes (PMTs) distributed throughout the instrumented volume.

1.2.2. Detector architecture

For photon detection, KM3NeT uses Digital Optical Modules (DOM), a 17-inch glass sphere containing 31 3" PMTs arranged to provide directional sensitivity and improved background rejection compared to designs such as the ANTARES or IceCube modules, which included a single 10" PMT. Each PMT exhibits a quantum efficiency of roughly 20-28%, a typical dark noise rate around 1.5 kHz, and a transit-time spread of ~ 4.5 ns. A set of internal instruments including a compass, tilt-meter, acoustic sensors, and LEDs enable precise calibration of orientation, timing, and position.

The DOMs are mounted on flexible vertical Detection Units (DUs), anchored to the sea floor and held taut by buoyancy. Many such units form a three-dimensional array, creating the large volumes required for neutrino astronomy and oscillation studies.

1.2.3. ARCA

Astroparticle Research with Cosmics in the Abyss (ARCA) targets astrophysical neutrinos from the TeV to PeV range. The detector geometry has been optimized for the detection of neutrinos from Galactic sources. ARCA complements IceCube by providing excellent visibility of the Southern Hemisphere sky, including the Galactic

Centre region. Its recent identification of an ultra-high-energy event, KM3-230213A, demonstrates the detector's capability for high-energy neutrino astronomy [25].

1.2.4. ORCA

ORCA is optimized for the detection of atmospheric neutrinos in the few GeV range. Its denser geometry allows for the reconstruction of short tracks and cascades with high efficiency, enabling precise determination of oscillation parameters and providing sensitivity to the neutrino mass ordering. Because these oscillation analyses rely heavily on neutrino nucleus interactions modelling, ORCA provides a natural environment to study generator-induced systematics. Accurate cross-section modelling as well as of the kinematics of the final particle state is crucial, as mismodeling can bias reconstructed observables and in turn affects the inferred oscillation parameters.

1.2.5. Systematic Uncertainties in ORCA

In ORCA, systematic uncertainties reflect incomplete knowledge of atmospheric neutrino fluxes, neutrino-nucleus interactions, and detector response. They can modify predicted event rates, spectral shapes, and flavour compositions, and are therefore implemented as nuisance parameters in analysis. A nuisance parameter is a parameter that is not of direct inferential interest but must be included in the statistical model to ensure valid inference on the parameters of interest. These parameters are varied within physically motivated ranges and marginalized over to obtain constraints on oscillation parameters [21, 26].

Systematics can be grouped into three main categories:

Uncertainties in primary cosmic rays and hadronic interactions in the atmosphere affect the normalization, energy dependence, zenith-angle distribution, and flavour ratios of the neutrino flux. These effects primarily distort the overall rate and broad spectral features [21].

In the few-tens of GeV range, uncertainties in neutrino-nucleon interactions as

well as nuclear effects, impact both total cross sections and the reconstruction of neutrino observables. They propagate to flavour classification and kinematic distributions [26].

The response of the multi-PMT optical modules, including photon detection efficiency, timing calibration, and angular acceptance, introduces additional uncertainties. The optical properties of seawater (absorption and scattering) affect light propagation and event reconstruction [21, 26].

1.3. Motivation of this Work

This thesis aims to investigate how the choice of interaction models influences oscillation analyses for the KM3NeT/ORCA detector. Atmospheric neutrino oscillations are analyzed by inferring energies and directions of the incoming neutrinos from Cherenkov light. Interaction models determine the predicted final-state topologies, kinematic distributions, and hadronic energy deposition, all of which directly impact the event reconstruction, flavour classification, and can therefore be a source of systematic uncertainties.

Previous studies, notably Coloma et al. (2014) [27] and Coyle et al. (2022) [28], have demonstrated that uncertainties in neutrino-nucleus interaction modelling can lead to significant biases in oscillation analyses. Coloma et al. studied a Tokai to Kamioka (T2K)-like ν_μ disappearance experiment using water Cherenkov detectors and showed that fitting data generated with one event generator using a different nuclear model can induce biases of up to $1 - 3\,\sigma$ in the extracted oscillation parameters. These effects originate from different modelling of final-state interactions, multi-nucleon processes, and energy reconstruction, and were found not to be mitigated by near-detector constraints. More recently, Coyle et al. investigated the impact of cross-section mismodeling and near-detector tuning procedures in long-baseline experiments and demonstrated that tuning can partially absorb modelling deficiencies, potentially biasing both standard oscillation measurements and searches for new physics. Together, these studies highlight that relying on a single

interaction model, or on data-driven tuning alone, can mask underlying nuclear uncertainties and introduce unquantified systematic effects. Neglecting this issue in the KM3NeT/ORCA analysis may therefore bias the inferred oscillation parameters and limit the achievable physics sensitivity.

This thesis is organized as follows. chapter 2 presents the theoretical foundations of neutrino event generators and surveys widely used implementations. chapter 3 reviews neutrino interaction channels, relevant kinematic variables, and detector-level observables. chapter 4 details the integration of `NEUT` into the Monte Carlo simulation chain.

chapter 5 introduces the statistical methodology employed in the subsequent analyses. A comparison of event-level distributions, their correlations, and particle multiplicities is given in chapter 6, followed by a study of optical observables in chapter 7 and an assessment of reconstruction performance in chapter 8. The thesis concludes with a summary and outlook in chapter 9.

2. Neutrino Event Generators

If not otherwise noted, information from this chapter is taken from [29, 30]. Neutrino event generators are essential computational tools employed to simulate neutrino interactions in detector materials, playing a crucial role in contemporary neutrino physics research and provide a quantitative link between the microscopic neutrinonucleus interaction and the experimentally observable final state.

2.1. Foundations of Neutrino Event Generators

Neutrino event generators facilitate the interpretation and analysis of data collected by neutrino oscillation experiments such as T2K, NuMI Off-axis ν_e Appearance (NOνA), Deep Underground Neutrino Experiment (DUNE), and others by predicting the outcomes of neutrino interactions with nuclear targets based on theoretical models. Since modern oscillation analyses rely on reconstructed observables, generators form an integral part of both physics extraction and detector simulation.

Due to the complexity of neutrinonucleus interactions, these tools employ approximations and theoretical frameworks that encapsulate the current understanding but also reflect existing knowledge gaps in nuclear physics. A neutrino interaction with a nucleus is not a simple two-body process. Instead, the neutrino interacts with a bound nucleon embedded in a correlated many-body system. The struck nucleon can be correlated with others, and the produced hadrons propagate through nuclear matter before leaving the nucleus.

The underlying theoretical basis typically involves solving transport equations derived from nuclear many-body theories, incorporating quantum mechanical principles into semi-classical approximations to manage computational complexity. In practice, this often means that the initial interaction is described using microscopic cross sections,

while the propagation of hadrons inside the nucleus is treated within transport theory [29].

Modern generator frameworks also reflect developments from high-energy physics, where fixed-order calculations of the hard interaction are combined with phenomenological models for hadronization and final-state dynamics [30]. Although neutrino energies are typically lower than collider energies, the same conceptual structure applies: a primary interaction, followed by radiation, hadron formation, and possible re-interactions in nuclear matter.

2.2. Relevance for Oscillation Experiments in the Few-GeV Range

For experiments operating in the few-GeV energy range and using dense nuclear media as targets, event generators are not auxiliary tools but an integral part of the analysis chain. In such experiments the incoming neutrino energy is not known for an individual event. Instead, it must be reconstructed from the observed final state. This reconstruction depends directly on the assumed interaction mechanism and on the modelling of the hadronic system produced inside the nucleus.

At neutrino energies of a few GeV, several reaction mechanisms contribute simultaneously, which are described in chapter 3. These processes overlap strongly in energy and momentum transfer and cannot be cleanly separated experimentally. Even a relatively narrow neutrino flux leads to a broad distribution in true interaction kinematics. As a result, measured observables always contain a mixture of different underlying reaction types. A realistic generator must therefore describe all relevant channels within a consistent theoretical framework [29].

Since oscillation analyses are, among other observables, based on the reconstructed neutrino energy spectrum, any mismatch between true and reconstructed energy directly propagates into the determination of oscillation parameters. In the few-GeV regime relevant for atmospheric neutrinos traversing the Earth, matter effects

introduce characteristic energy-dependent distortions in the oscillation probability. A shift in the reconstructed energy scale or an incorrect modelling of specific interaction channels can mimic or distort these effects. For this reason, the modelling of nuclear dynamics and reaction mechanisms is tightly connected to the achievable precision on parameters such as the mass ordering.

Event generators are also essential for detector simulations and efficiency studies. The angular and energy distributions of leptons and hadrons determine the pattern of Cherenkov photons and therefore the reconstruction performance [29].

2.3. Overview of Prominent Generators

Although this work concentrates on `NEUT` and Generates Events for Neutrino Interaction Experiments (GENIE), additional neutrino event generators are included for completeness.

2.3.1. GENIE

GENIE [31, 32] is widely adopted due to its versatility and its comprehensive list of available physics models. It provides detailed modelling of neutrinonucleus interactions.

GENIE employs predominantly phenomenological and empirical models, tuned against data from neutrino experiments, making it adaptable for diverse experimental conditions and target nuclei. Tuning neutrino event generators such as within experimental uncertainties of physical input can reduce cross-section uncertainties, but adjusting parameters or arbitrarily modifying model components can undermine theoretical consistency [29]. GENIE is widely used in long-baseline and atmospheric neutrino experiments, including applications within KM3NeT and IceCube, where its flexibility and broad validation are advantageous for large-scale simulations.

2.3.2. GiBUU

Giessen Boltzmann-Uehling-Uhlenbeck (GiBUU) [33] distinguishes itself with a fully consistent theoretical framework based on nuclear transport theory, rigorously treating nuclear effects and Final State Interactions (FSIs). Transport theory is a framework used to describe how a many-particle system changes in time and space under the influence of mean fields and individual collisions between particles. Instead of tracking exact quantum states, it follows the evolution of a distribution of particles in phase space, similar to a generalized version of a classical particle density that also accounts for interactions and scattering. Unlike `NEUT` (subsection 2.3.4) and GENIE, GiBUU employs semi-classical transport equations that describe particle propagation and interaction dynamics within nuclei. This provides a self-consistent treatment of both initial and final-state nuclear effects.

GiBUU's strength lies in its ability to simulate detailed particle spectra and nuclear responses, thereby offering insight into systematic uncertainties originating from nuclear modeling. Its unified description of different reaction channels makes it particularly suited for studies where the interplay of processes is relevant.

2.3.3. NuWro

NuWro [34, 35] is a neutrinonucleus event generator developed within the Wrocław Neutrino Group. Like other modern neutrino generators, it provides access to individual interaction channels within a flexible simulation framework.

In NuWro, this flexibility is realized through a modular architecture in which specific interaction mechanisms can be enabled, modified, or replaced with minimal technical overhead. NuWro emphasizes theoretical clarity and rapid prototyping of new physics models. It is widely used in phenomenological studies and sensitivity analyses for oscillation experiments such as T2K, Main Injector Neutrino ExpeRiment to study ν-A interactions (MINERνA), and future long-baseline programs.

2.3.4. NEUT

NEUT [36, 37, 38] is the primary neutrino interaction generator used by the T2K and Super Kamiokande (SK) experiment. It features phenomenological models tuned using experimental data, especially from low-energy neutrino interactions relevant to accelerator-based experiments.

It also implements nuclear effects such as spectral functions and final-state interactions, typically with simplified assumptions to maintain computational efficiency. In contrast to the other mentioned generators, NEUT is not open-source software and is available only upon request. Some modes implemented in NEUT, notably parts of the Meson Exchange Current (MEC) sector which is discussed in chapter 3, are adapted from NuWro.

2.3.5. Achilles

Achilles [39, 40] is a modern neutrino event generator framework designed with a strong emphasis on theoretical consistency, modularity, and transparency. It aims to provide a flexible platform in which different microscopic models for neutrinonucleon and neutrinonucleus interactions can be implemented and systematically compared. In contrast to other generators, notably NEUT, that evolved over decades, Achilles is built with a modern software architecture that facilitates the separation between physics components and technical infrastructure. This allows for controlled implementation of new interaction models and for systematic studies of theoretical uncertainties. Particular emphasis is placed on a clear treatment of nuclear effects and on the consistent description of different interaction regimes within a unified framework.

2.4. PYTHIA

PYTHIA is a Monte Carlo event generator for high-energy particle collisions that provides an exclusive description of final states at the level of stable particles. It

models the complete event evolution, from the perturbative hard scattering through parton shower development to non-perturbative hadronization.

In neutrino interactions, the primary weak vertex on nucleons or nuclei is simulated by dedicated generators. `PYTHIA` is predominantly employed in the Deep Inelastic Scattering (DIS) regime, where the neutrino interacts with an individual quark. The resulting quark system is transferred to `PYTHIA` for initial- and final-state radiation, parton showering, and string fragmentation, producing hadronic final states (e.g. π, K, N). Event generators such as GENIE and `NEUT` interface to `PYTHIA` for this purpose. The predicted hadron multiplicities and kinematic distributions propagate directly into detector-response simulations and neutrino reconstruction [41, 42, 43].

3. Neutrino-Nucleon Interactions

This chapter introduces the fundamentals of neutrino-nucleon interactions. The relevant interaction channels are first described, followed by a definition of the key kinematic observables. The definitions are used throughout this thesis.

3.1. Interaction Mechanisms

Interaction mechanism are grouped according to their final state particles, underlying hadronic dynamics and typical energy transfer.

3.1.1. Elastic, Quasielastic and Meson-Exchange Processes

Processes typically not involving the creation of mesons are Charged Current Quasi Elastic (CCQE), Neutral Current Elastic (NCEL) scattering and MEC interactions [44].

CCQE scattering corresponds to a charged-current interaction in which a neutrino or antineutrino scatters elastically from a single nucleon. At the nucleon level, the process is given by

$$\nu_\ell(\bar{\nu}_\ell) + n(p) \rightarrow \ell^-(\ell^+) + p(n)\,. \tag{3.1}$$

While this interaction is elastic for a free nucleon, its manifestation in nuclei is modified by initial-state effects such as binding energy, Fermi motion, and Pauli blocking (section 3.2), which smear the outgoing-lepton kinematics relative to free scattering.

NCEL scattering proceeds similarly but retains the final-state neutrino. Because the outgoing neutrino is unobserved, event characterization relies on nucleon recoil

and hence on the same nuclear dynamics that shape CCQE-like observables and therefore is mainly invisible in KM3NeT.

MEC interactions arise when the neutrino interacts with an exchange meson mediating between nucleons. The dominant two particles-two holes (2p2h) channel involves pion- and ρ-exchange currents and medium-modified Δ excitation followed by pion reabsorption. Although no pion appears, energy-momentum is redistributed within a correlated pair, producing non-CCQE kinematics. Subleading three particles-three holes (3p3h) excitations, often originating from non-pionic Δ decays or re-scattering, contribute at the $\mathcal{O}(20\%)$ level of 2p2h for $E_\nu \gtrsim 1$ GeV.

3.1.2. Resonant, Coherent and Diffractive Production

Single-meson production in neutrinonucleus interactions can be classified according to the microscopic interaction mechanism and the degree to which the nucleus participates collectively in the process.

In Resonant (RES) production, the neutrino interacts with an individual bound nucleon and excites it to an intermediate baryonic resonance. The most prominent contribution at low energies arises from the $\Delta(1232)$, while higher-mass N^* and Δ^* states become increasingly relevant as the available energy increases. The excited resonance subsequently decays, most commonly into a nucleonpion final state. Because the interaction occurs on a single nucleon embedded in the nuclear medium, the residual nucleus is generally left in an excited state and may fragment. The outgoing hadrons can undergo intranuclear re-scattering, absorption, or charge exchange before exiting the nucleus. Although non-strange channels dominate, associated strangeness production such as $\Lambda + K$ can also occur, albeit with smaller probability.

In Coherent (COH) production, the neutrino couples to the nucleus as a whole rather than to an individual nucleon. The interaction proceeds coherently over all nucleons, and the nucleus remains in its ground state after the interaction. As a consequence, the process is restricted to kinematic configurations in which the

nucleus receives only a small recoil. The produced meson therefore carries most of the transferred energy and is emitted predominantly in the forward direction. For pion production, the interaction is largely governed by the axial component of the weak current and is commonly described using Partially Conserved Axial Vector Current (PCAC)-based models [45]. In charged-current reactions, the finite mass of the outgoing charged lepton reduces the accessible phase space at low neutrino energies, leading to a suppression relative to the corresponding neutral-current channel.

In Diffractive (DIF) production, the neutrino interacts with a single nucleon and produces a meson while leaving the nucleon itself intact. The process shares similarities with coherent scattering in that the recoil of the target system is small and the produced mesons are typically forward-directed. However, in contrast to coherent production, the interaction is localized on a single nucleon and does not require the nucleus to remain in its ground state. In nuclear targets, diffractive processes overlap experimentally with both resonant and coherent channels, and their separation requires careful treatment of nuclear screening and absorption effects.

3.1.3. Shallow and Deep Inelastic Scattering

Two main mechanism contribute to multi meson and hadron production. At sufficiently high neutrino energies, the probe resolves the internal quark structure of the nucleon rather than interacting with it as a whole baryonic degree of freedom. The Shallow Inelastic Scattering (SIS) describes the transition region between resonance-dominated dynamics and fully developed quark scattering. In this regime, multi-hadron final states become common, and individual resonance contributions overlap strongly. The hadronic system may contain several pions and heavier mesons, and no single intermediate resonance dominates the interaction. Modeling this region requires a consistent interpolation between hadronic resonance descriptions and quark-level approaches.

The DIS corresponds to scattering from individual quarks inside the nucleon. The neutrino interacts with a quark via exchange of a weak gauge boson, and the struck quark subsequently hadronizes, producing a multi-particle final state that can exhibit jet-like structure at high energies. The inclusive cross section is expressed in terms of nucleon structure functions, which encode the distribution functions of quarks and gluons. In practical applications, quarkhadron duality is often invoked to relate averaged resonance contributions to the scaling behavior observed in DIS [46].

3.2. Nuclear Effects

In neutrinonucleus scattering, the elementary neutrinonucleon interaction occurs in a bound many-body system. Nuclear structure therefore modifies both the kinematically accessible phase space at the primary vertex and the composition of the observable final state.

3.2.1. Initial-State Nuclear Effects

In a nuclear environment, nucleons occupy bound quantum states in a mean-field potential and are neither free nor at rest. The binding energy [47] denotes the separation energy required to remove a nucleon from the nucleus. In neutrinonucleus scattering, it reduces the energy available at the primary vertex, modifies kinematic thresholds, and induces systematic shifts in reconstructed energies relative to free-nucleon interactions.

Fermi motion [47] arises from the intrinsic momentum distribution of bound nucleons, bounded by a characteristic Fermi momentum determined by the local nuclear density. The unknown initial-state momentum on an event-by-event basis leads to a convolution of the elementary interaction with the nuclear momentum distribution, broadening outgoing-lepton and hadronic kinematics. Consequently, reconstructed observables exhibit an irreducible smearing, independent of detector resolution.

Pauli blocking [48] further restricts the available phase space. Final states in which the outgoing nucleon would occupy an already filled state below the Fermi surface

are forbidden by the Pauli exclusion principle. This suppresses interactions at low momentum transfer and reduces the cross section when the nucleon momentum lies below the local Fermi momentum.

Short-range correlations and multi-nucleon dynamics extend beyond the independent-particle approximation. Correlated nucleon pairs or triplets can participate coherently in the interaction, redistributing energy and momentum among multiple nucleons and modifying both the final-state topology and the effective kinematics at the vertex.

3.2.2. Final-State Interactions

FSI [29] comprise all strong-interaction processes experienced by hadrons after the primary weak vertex and before they exit the nuclear medium. While the initial interaction is governed by the weak interaction, the subsequent propagation of produced hadrons is described by hadronnucleon interactions embedded in a nuclear potential.

The interaction vertex can occur at any location within the nuclear volume. The produced hadrons propagate through the residual nucleus and may undergo elastic scattering, which alters their momentum without changing particle identity, or inelastic scattering, including baryon excitation and secondary particle production. Pions are particularly sensitive to intranuclear transport: they can be absorbed on correlated nucleon pairs ($\pi NN \rightarrow NN$), effectively removing them from the observable final state, or undergo charge exchange, such as $\pi^+ + n \rightarrow \pi^0 + p$, thereby modifying the hadronic composition.

Throughout this transport, the nuclear mean field continuously alters hadron energies and trajectories. Final-state interactions therefore redistribute energy and modify particle multiplicities without changing the total four-momentum transferred at the primary vertex. They play a central role in shaping experimentally observed topologies and in connecting microscopic interaction mechanisms to detector-level observables.

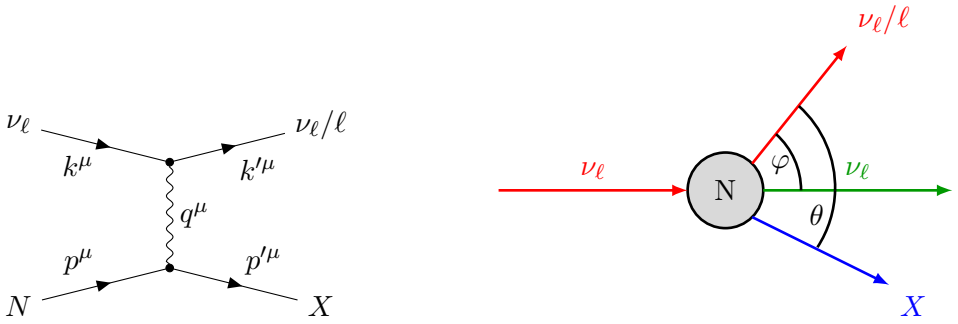

Figure 3.1.: Kinematic description of neutrino-nucleus scattering: diagrammatic representation (left) and definition of scattering angles φ and hadronic angle θ (right).

Because these effects alter the relationship between the primary four-momentum transfer and the observable final state, it is useful to introduce the Lorentz-invariant kinematic variables that characterize the interaction at the vertex.

3.3. Kinematics in Neutrino Scattering

Figure 3.1 illustrates the geometric and diagrammatic structure of neutrino-nucleon scattering. Vectors like x^μ (x_μ) denote four-vectors and $\vec{x}$ denote three-vectors. An incoming neutrino of four-momentum $k^\mu = (E_\nu, \vec{k})$ scatters off a (bound) nucleon with four-momentum $p^\mu = (E, \vec{p})$, where binding and Fermi motion imply $E \approx M$ and $|\vec{p}| \ll M$ but nonzero. The outgoing charged lepton carries momentum $k'^\mu = (E_\ell, \vec{k}')$, and the four-momentum transfer given by

$$q^\mu = k^\mu - k'^\mu \tag{3.2}$$

$$Q^2 = -q^\mu q_\mu > 0. \tag{3.3}$$

The Lorentz-invariant kinematic variables x and y are central across all interaction

regimes:

$$x = \frac{Q^2}{2\, p^\mu q_\mu}, \tag{3.4}$$

$$y = \frac{p^\mu q_\mu}{p^\mu k_\mu} \approx 1 - \frac{E_\ell}{E_\nu}. \tag{3.5}$$

The Bjorken x parameter from Equation 3.4 parametrizes the longitudinal momentum fraction of the struck parton where $x = 1$ for elastic scattering, $0 < x < 1$ in DIS, and for multi-nucleon and resonant processes in nuclei may exceed $x > 1$. Small values of x probe sea quarks and gluons, while larger x is dominated by valence quarks. The region $x > 1$ arises in nuclei due to short-range correlations and multi-nucleon dynamics that effectively provide more longitudinal momentum than a single free nucleon. For experiments such as ORCA, which operate at neutrino energies starting at few GeV, the event rates and kinematic distributions depend sensitively on the x-dependence of the nucleon structure functions, making an accurate description of Bjorken x essential for predicting cross sections, modeling nuclear effects, and reconstructing the incoming neutrino energy from the observed lepton and hadronic final state.

The Bjorken inelasticity y, defined in Equation 3.5, measures the fraction of the incoming neutrino energy transferred to the hadronic system, where E_ℓ is the energy of the outgoing charged lepton and E_{had} the hadronic energy deposition. The approximation is exact when Fermi-momentum is neglected, or in other words if the struck nucleon is at rest. Low values of y correspond to events in which most of the neutrino energy is carried by the charged lepton, while high y indicates dominant energy transfer to the hadronic shower. The inelasticity is therefore directly correlated with both the charged-lepton scattering angle and the relative light yield of the lepton track and hadronic cascade. This quantity is commonly referred to as Bjorken y.

Measured inelasticity distributions for ν_μ and $\bar{\nu}_\mu$ are shown in Figure 3.2. Although KM3NeT cannot identify the separate neutrino vs anti neutrino interactions on

an event-by-event basis, the y distributions differ statistically between neutrinos and antineutrinos due to their distinct differential cross sections. Consequently, the reconstructed inelasticity provides statistical sensitivity to the $\nu/\bar{\nu}$ composition of the event sample [21].

While the Bjorken variables x and y are rigorously defined for deep-inelastic scattering on a single free nucleon, their kinematic construction can be generalized to interaction mechanisms such as MEC and COH, where the probe couples to multiple nucleons. In this case, an effective target four-momentum is introduced,

$$p^{\mu}_{\text{eff}} = \sum_i p^{\mu}_i \,, \tag{3.6}$$

where the sum extends over all participating nucleons.

Replacing the nucleon four-momentum by p^{μ}_{eff} in the standard definitions yields

$$x = \frac{Q^2}{2\, p^{\mu}_{\text{eff}} q_{\mu}}, \tag{3.7}$$

$$y = \frac{p^{\mu}_{\text{eff}} q_{\mu}}{p^{\mu}_{\text{eff}} k_{\mu}} \approx 1 - \frac{E_{\ell}}{E_{\nu}}, \tag{3.8}$$

thereby defining effective Bjorken variables that remain confined to the interval $(0, 1)$ by construction.

The formulation in Equation 3.7 and Equation 3.8 is inspired by [49, 50]. However, it does not constitute a direct definition or formal prescription from those references.

3.4. Experiment-Oriented Observables

The oscillation analysis relies on reconstructed observables, which are derived from a limited set of detector-level observables. The following quantities are therefore selected because they control the mapping between true and reconstructed kinematics and are sensitive to generator-dependent modeling of hadronic dynamics.

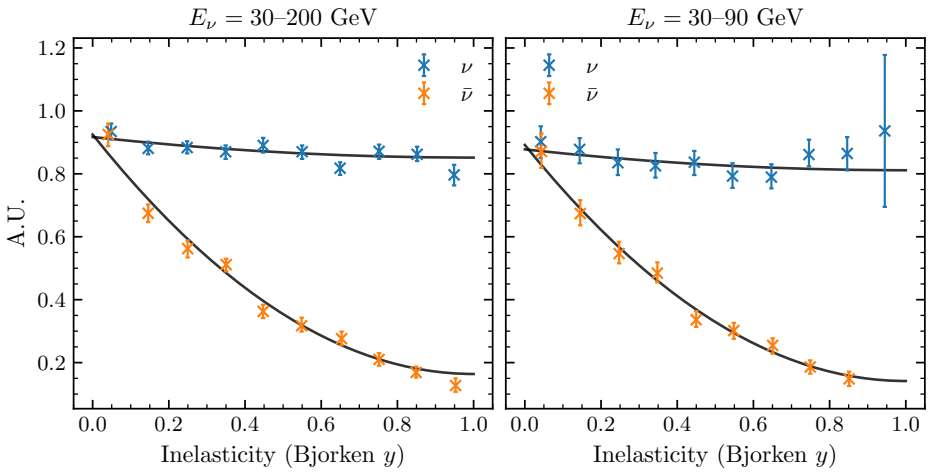

Figure 3.2.: Measured Bjorken y distributions for ν_μ and $\bar{\nu}_\mu$, data taken from [51].

3.4.1. Leptonic Scattering and Hadronic Angle

The lepton scattering angle φ is defined as the angle between the incoming neutrino momentum $\vec{k}$ and the outgoing charged-lepton momentum $\vec{k}'$,

$$\cos\varphi = \frac{\vec{k}\cdot\vec{k}'}{|\vec{k}|\,|\vec{k}'|}. \tag{3.9}$$

The lepton scattering angle φ is primarily sensitive to the primary interaction kinematics and is directly linked to the neutrino energy through quasi-elastic and deep-inelastic scattering relations. It therefore provides a constraint on the reconstructed neutrino direction and energy with minimal dependence on hadronic modeling.

The hadronic angle θ characterizes the orientation of the hadronic system relative to the outgoing lepton. An effective hadronic momentum vector is constructed as

$$\vec{p}_X = \sum_i \hat{p}_i\, E_i, \tag{3.10}$$

where $\hat{p}_i$ denotes the directional unit vector of particle i, and E_i represents either its kinetic energy or its visible energy, as defined in subsection 3.4.2 in the next section. When E_i is taken as the kinetic energy, $\vec{p}_X$ reflects the true event kinematics. When

E_i is taken as the visible energy, $\vec{p}_X$ encodes the detector-level response. The hadronic angle is then given by

$$\cos\theta = \frac{\vec{p}_X \cdot \vec{k}'}{|\vec{p}_X|\,|\vec{k}'|}. \tag{3.11}$$

A schematic illustration of the lepton and hadronic angles is shown in Figure 3.1. Both angles probe complementary aspects of neutrinonucleon interactions and enter energy and topology reconstruction in distinct ways.

The hadronic angle θ encodes information on the energymomentum transfer to the nuclear system and is sensitive to final-state interactions, particle multiplicities, and intranuclear transport. At detector level, it governs the spatial distribution of visible energy and thus affects event classification, containment, and resolution. Jointly analyzing φ and θ allows generator differences in primary interaction modeling and hadronic final-state dynamics to be disentangled, which is essential for controlling systematic uncertainties in oscillation measurements.

3.4.2. Visible Energy

When neutrinos interact with nucleons, secondary particles are produced that lose energy mainly through Cherenkov emission, bremsstrahlung, and e^+e^- pair production. To quantify the energy detectable by the instrument-and thus relevant for energy reconstruction-the visible energy is estimated analytically. In the one-particle approximation used in this work, the visible energy of a particle is defined as the energy of an electron producing the same amount of photons. Mainly electromagnetically interacting and decaying particles (electrons, photons, π^0, η) are assigned a visible energy of their kinetic energy, while neutrinos contribute no visible energy. Muons are treated separately: their visible energy is obtained from the energy loss along the muon track in seawater, computed from the muon range and normalized to the average electromagnetic light yield per unit track length. For hadrons ($\pi^{\pm}, K, p, n$), the visible energy fraction of the particles energy depends on particle type and energy and is parametrized using GEANT simulations. At high energies,

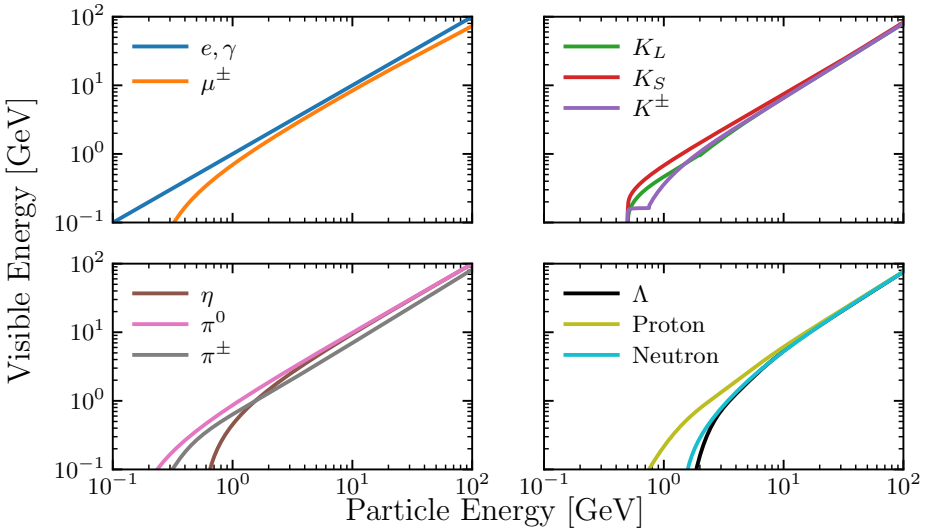

Figure 3.3.: Visible energy response used in this work for single-particle final states with the energy of the corresponding particle on the x axis and the visible energy on the y axis. The four panels group particles by category: electrons/photons and muons (upper left), kaons (upper right), light mesons (lower left), and baryons (lower right).

all hadronic species asymptotically approach a common electromagnetic scaling due to the dominance of π^0-induced subshowers, consistent with the formulation of the one-particle approximation developed for Astronomy with a Neutrino Telescope and Abyss environmental RESearch project (ANTARES) [52] and further refined for KM3NeT. The resulting visible energy for different particle species are shown in Figure 3.3. The event-level visible energy is defined as the sum of the visible contributions of all secondary particles,

$$E_{\text{vis}} = \sum_i E_{i,\text{vis}}, \tag{3.12}$$

where $E_{i,\text{vis}}$ denotes the visible energy associated with particle i.

The visible energy ratio quantifies the observable fraction of the incoming neutrino energy,

$$R_{\text{vis}} = \frac{E_{\text{vis}}}{E_\nu} = \frac{\sum_i E_{i,\text{vis}}}{E_\nu}, \tag{3.13}$$

with E_ν the energy of the incident neutrino.

Differences in visible energy between neutrino generators therefore reflect differences in final-state composition and energy partitioning, in particular the relative electromagnetic and hadronic components.

In KM3NeT, such differences translate into shifts in the reconstructed cascade energy scale and resolution, influence event classification, and constitute a generator-dependent source of systematic uncertainty.

All of these quantities enter oscillation analyses through reconstruction of neutrino observables and generator-dependent modeling of nuclear effects.

4. The Monte Carlo Simulation Chain

This chapter describes the simulation and processing chain employed to produce detector-level observables from `NEUT`-generated neutrino interactions.

The Monte Carlo simulation [53] chain comprises sequential, interdependent stages, orchestrated by `snakemake` [54], a rule-based workflow manager that encodes task dependencies to guarantee reproducible and scalable execution. It is configured by metadata describing the simulated run, detector geometry, and calibration constants, which define the inputs to all subsequent components.

First, primary neutrino interactions are generated at the event-generator level. The resulting final-state particles are then propagated through the detector medium, accounting for energy loss and secondary interactions, followed by photon production and transport.

Detector effects are subsequently applied, including optical photon collection by the PMTs, electronic response, background overlay, and trigger simulation. The simulated signals are then processed by the reconstruction algorithms, and the reconstructed observables are written to a summary file (DST) file. A schematic overview of the full chain is shown in Figure 4.1.

4.1. Event Generation and External-Generator Integration

The Monte Carlo simulation chain follows the native GENIE architecture, with the primary neutrino-nucleus event generator replaced by `NEUT`. All subsequent stages of the simulation chain remain consistent with the standard GENIE-based workflow, ensuring compatibility with detector response and reconstruction modules.

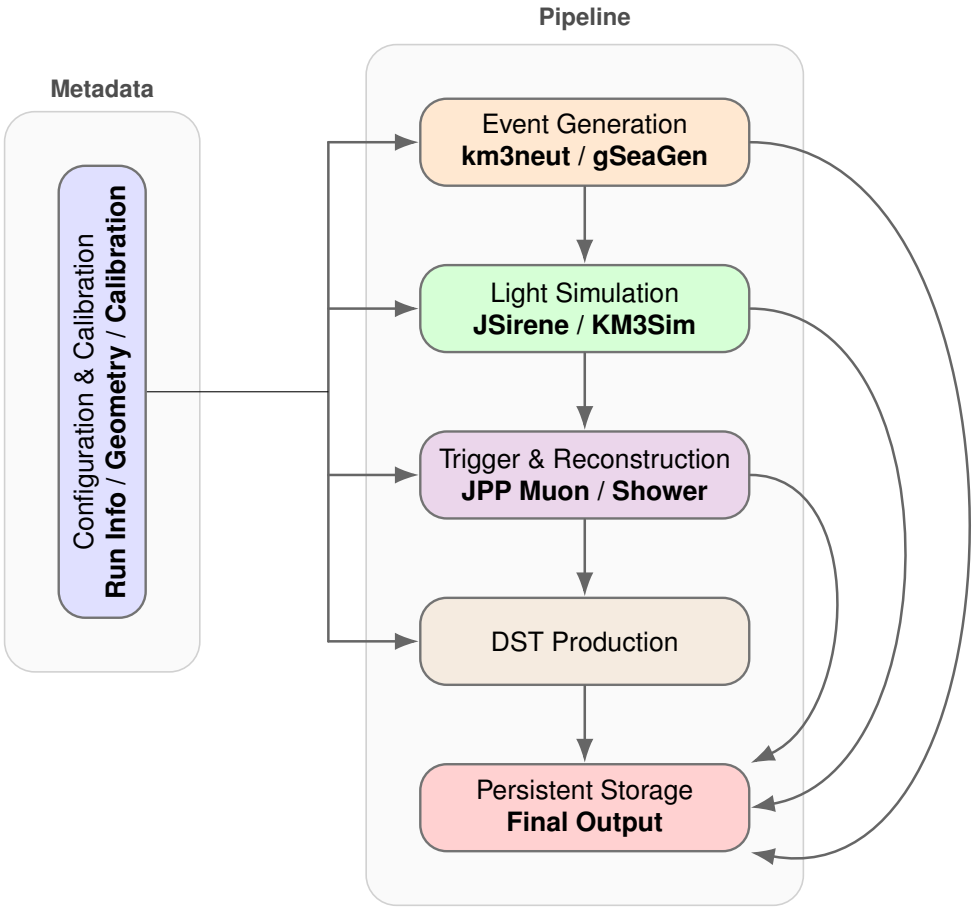

Figure 4.1.: A schematic overview of the Monte Carlo simulation pipeline.

4.1.1. Standard GENIE-based Architecture

Within the standard simulation chain, GENIE is not invoked directly. Instead, the wrapper framework `gSeaGen` [55] acts as an abstraction layer between user-defined steering parameters and the underlying physics components. It interfaces with the selected flux driver to sample the incident neutrino flux in energy, direction, and flavor and applies the corresponding interaction probabilities. It also handles the detector geometry by sampling interaction vertices within the instrumented volume or the surrounding generation region and by accounting for the target material composition.

4.1.2. Integration of `NEUT` via `km3neut`

To enable the processing of events generated with `NEUT`, several software-level extensions were implemented to support the simulation of DIS ν_τ interactions, the treatment of hydrogen as an explicit target, and the handling of stable FSI (described in Appendix A). These modifications do not alter the underlying NEUT physics models. For this purpose, the dedicated wrapper software `km3neut` [56] was developed.

Events are generated by `NEUT` and processed through `km3neut`, which translates a `gSeaGen`-like configuration into the corresponding `NEUT` jobcards and random seeds, including the definition of the neutrino energy spectrum. Events failing internal consistency checks or terminating with error codes are discarded and regenerated. The wrapper also manages medium composition and target treatment. For composite materials such as sea water, interactions are generated separately for each relevant nuclear target. These target-specific samples are subsequently merged according to their relative contribution to the expected interaction rate, accounting for both elemental abundances and the flux averaged cross section. During merging, additional consistency checks are applied and incomplete or invalid events are filtered and the final interaction records are converted to the `km3net-dataformat` [57], including the generation weights defined below. The resulting files are passed to the `gSeaGen` external generator interface for vertex placement and further detector-level processing. Generation parameters are summarized in Table B.3.

A central difference between `km3neut` and `gSeaGen` lies in the energy-sampling prescription. In `km3neut`, the generated number of events follows

$$\mathrm{d}N \propto E^{-\gamma}\,\sigma(E)\,\mathrm{d}E, \tag{4.1}$$

where E denotes the neutrino energy, γ the spectral index, and $\sigma(E)$ the neutrino-nucleus interaction cross section. The explicit inclusion of $\sigma(E)$ enhances the relative contribution of higher-energy interactions and suppresses lower-energy ones.

In contrast, `gSeaGen` samples according to

$$\mathrm{d}N \propto E^{-\gamma}\,\mathrm{d}E, \tag{4.2}$$

independent of the cross section, apart from the kinematic suppression of ν_τ interactions below threshold.

When reweighting events to a uniform reference spectrum in energy, this difference requires an additional factor $\sigma(E)^{-1}$ for `km3neut` samples. The corresponding energy-generation weights are therefore

$$\mathrm{EG}(E) = \begin{cases} E^{\gamma}, & \text{for } \texttt{gSeaGen}, \\ E^{\gamma}\sigma(E)^{-1}, & \text{for } \texttt{km3neut}. \end{cases} \tag{4.3}$$

To obtain comparable statistics per energy bin after detector-level processing, `km3neut` samples are generated internally with a shifted spectral index $\gamma \to \gamma + 1$, reflecting the approximately linear rise of $\sigma(E)$ at higher energies. The resulting expected interaction rates are shown in Figure 4.2. For ν_e, $\bar{\nu}_e$, ν_μ, $\bar{\nu}_\mu$, ν_{NC}, and $\bar{\nu}_{\mathrm{NC}}$, both generators yield comparable rates. For ν_τ and $\bar{\nu}_\tau$, however, differences in cross-section modeling produce a reduced rate near threshold in `km3neut` and an enhanced rate above $E_\nu \gtrsim 10\,\mathrm{GeV}$, reaching deviations of up to one order of magnitude at 100 GeV.

All samples are reweighted to a neutrino-energy–uniform spectrum, eliminating generator-induced spectral biases such that residual differences in reconstructed observables reflect interaction modeling and detector response. The procedure is illustrated in Figure 4.3 for spectral indices $\gamma \in \{0, 1.4, 2, 3\}$ with 5×10^6 events per configuration.

In the `km3neut` samples, residual deviations at low energies originate from elevated rejection rates and generation failures during internal consistency checks. The differing sampling strategies are also evident in the statistical uncertainties: for `km3neut`, uncertainties increase toward low energies relative to `gSeaGen`, whereas

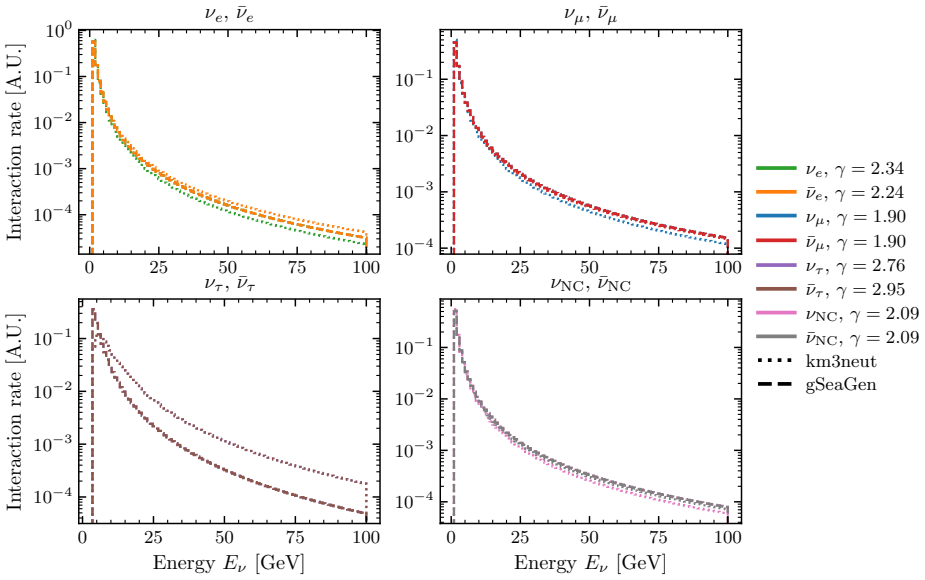

Figure 4.2.: Expected interaction rates for `km3neut` and `gSeaGen`, grouped by neutrino species, using the spectral indices applied in `gSeaGen`. For `km3neut`, the generator uses a spectral index of $\gamma + 1$. In both samples, the ν_τ contribution is largely obscured by $\bar{\nu}_\tau$.

for `gSeaGen` they rise more steeply at high energies.

In `km3neut`, neutrino energies are sampled from a discretized flux histogram with 100 bins. A bin is selected according to its integrated weight, and the energy is drawn uniformly within that interval. The weight in (4.3) is evaluated at the sampled continuous energy. This combination of piecewise-constant sampling and continuously evaluated weights introduces a mild aliasing effect, which can generate residual structures if very fine analysis binning is applied. In the present analysis, coarser binning than the generation histogram is used, rendering such effects negligible.

4.1.3. Vertex placement and interaction probability

To integrate pre-generated neutrino interactions into the KM3NeT simulation chain, a dedicated driver is used that reads interaction records from an input file and turns them into fully placed detector events. Rather than producing interactions internally, it treats the file as the generated events for the final-state particle content and their kinematics. For each record, it constructs an event object, transfers the

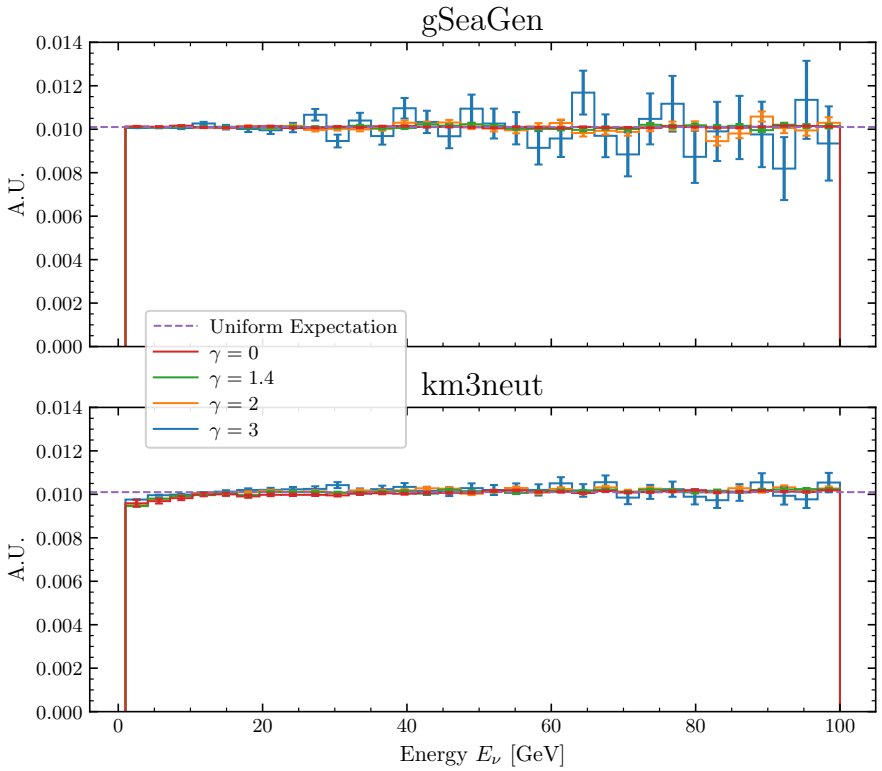

Figure 4.3.: Energy distributions after reweighting. The upper panel corresponds to `gSeaGen`, the lower panel to `km3neut`. The dashed line indicates the expected uniform distribution.

relevant interaction metadata and reads the particle list in the `km3net-dataformat`. A key task of the driver is to distribute the interaction vertices in a volume centred around the detector where it assigns each imported interaction a time and space vertex within the detector and surrounding medium. Externally generated events are defined in a local interaction frame with the neutrino direction aligned to the positive z-axis and the interaction vertex at the origin. During vertex placement, the full event is rotated and translated into detector coordinates. The incoming neutrino direction and time are sampled from the configured flux description and detector geometry. Direction and time are sampled from the configured flux description, while the neutrino energy is taken from the imported interaction record to preserve the external kinematics.

Since the interaction probability depends on the material-dependent column density traversed by a given neutrino trajectory, not all sampled flux neutrinos yield a

physically admissible vertex within the relevant target volume. Vertex generation therefore employs an accept-reject scheme adapted from GENIE's event placement algorithm.

For each trial, a neutrino is drawn from the flux and propagated through the geometry to determine the density-weighted path length $\int \rho(s)\,\mathrm{d}s$ in the target material. The corresponding interaction probability is computed from this column density and normalized to a precomputed upper bound set to the maximum column density within the generation volume. A uniform random number $r \in (0, 1)$ is then compared to the normalized probability. If r exceeds this value, the candidate is rejected and a new flux neutrino is sampled, otherwise, an interaction vertex is placed along the trajectory.

After vertex placement, secondary $\mu^{\pm}$ are propagated through the detector geometry and subjected to containment criteria, events failing these requirements are rejected, as they cannot yield a detectable signature.

4.2. Light Simulation, Detector Response and Reconstruction

After vertex placement, the detector response is simulated in two stages: optical photon production and transport, followed by modelling of the PMTs and electronic response.

Photon propagation in sea water is handled by two complementary tools. For neutrino energies below 100 GeV, `KM3Sim` [58] performs a full Monte Carlo simulation including absorption, scattering, and wavelength-dependent effects. At higher energies, where events are more extended and photon statistics increase, `JSirene` [59] is used. It employs parameterized light emission and transport to reproduce the relevant timing and spatial distributions at reduced computational cost.

At the detector level, photons are converted into photoelectrons according to the wavelength-dependent quantum efficiency of the PMTs, including angular acceptance,

collection efficiency, and transit-time spread. Dark noise and optical background from ^{40}K decays and bioluminescence are overlaid using run-dependent calibration constants. The electronic response digitizes the signals into time and charge measurements.

Trigger algorithms select events with temporally and spatially correlated hit patterns compatible with track-like or shower-like topologies. Accepted events are reconstructed independently of the neutrino flavour hypothesis using dedicated algorithms for track-like (Charged Current (CC) ν_μ) and shower-like (ν_e and Neutral Current (NC)) interactions.

The reconstructed observables are stored in DST files containing high-level quantities for physics analyses. Intermediate generator-, light-, and reconstruction-level outputs are retained for validation and studies.

5. Statistical Methods

Comparisons of neutrino event generators are only meaningful if the statistical interpretation is at least as controlled as the underlying physics modeling. Generator differences may manifest as localized distortions in restricted regions of phase space, subtle shape variations, or discrepancies that become visible only once statistical fluctuations are properly quantified. Without rigorous treatment, apparent deviations risk being misidentified as model deficiencies, while genuine tensions may remain obscured by finite Monte Carlo precision.

The full implementation details and data handling procedures are documented in [60].

5.1. Event Representation and Binning

All observables are represented as a binned representation of underlying probability density functions. Events are accumulated in multidimensional histograms $H(\vec{x})$ defined over a set of observables $\vec{x}$, where each bin content corresponds to the weighted sum of events falling within a hyper-rectangular phase-space element. Binning is fixed a priori and common to all generators to ensure bin-wise comparability.

After binning, selections are implemented as axis-aligned rectangular cuts in observable space. Projections onto lower-dimensional subspaces are then performed by marginalization over the remaining dimensions, yielding one- or two-dimensional histograms. Throughout the analysis, bins are treated as statistically independent estimators.

For combined $\nu+\bar{\nu}$ histograms, the $\bar{\nu}$ contribution is rescaled such that its total weight matches that of the corresponding ν distribution separately for each generator. The same rescaling factor is applied to both the $\bar{\nu}$ yields and their statistical uncertainties

before summing the two contributions.

5.2. Normalization

Projected histograms are normalized to approximate probability density functions. For a one-dimensional histogram with bin contents N_i and bin widths Δx_i, the normalized density is given by

$$p_i = \frac{N_i}{\sum_j N_j \, \Delta x_j} \,, \tag{5.1}$$

with an analogous definition in two dimensions including the bin area $\Delta x_i \Delta y_j$. This normalization ensures that integrals over the histogram approximate unity. Empty bins are excluded from the normalization sum to avoid bias from ill-defined uncertainties.

5.3. Statistical Uncertainties

All histograms are treated as weighted event counts. The statistical uncertainty on a bin content N is given by

$$\Delta N = \sqrt{\sum_{i \in \text{bin}} w_i^2} \,, \tag{5.2}$$

where w_i denotes the event weight. In the special case $w_i = 1$ for all events, this reduces to the standard Poisson uncertainty $\Delta N = \sqrt{N}$. This estimator assumes independent events and neglects correlations introduced by reweighting.

When neutrino and antineutrino samples are combined, their contributions are treated as statistically independent, and uncertainties are added in quadrature,

$$\Delta N_{\nu+\bar{\nu}} = \sqrt{\Delta N_\nu^2 + \Delta N_{\bar{\nu}}^2} \,. \tag{5.3}$$

After normalization, uncertainties are propagated using the same normalization

factor, preserving relative bin-wise uncertainties.

5.4. One-Dimensional Comparisons

To quantify differences between generators, bin-wise ratios of normalized distributions are constructed,

$$R_i = \frac{N_{A,i}}{N_{B,i}}\,, \tag{5.4}$$

where $N_{A,i}$ and $N_{B,i}$ denote the normalized bin contents of generators A and B, respectively.

Statistical uncertainties on the ratio are obtained via Gaussian error propagation,

$$\Delta R_i = \sqrt{\left(\frac{\Delta N_{A,i}}{N_{B,i}}\right)^2 + \left(\frac{N_{A,i}\,\Delta N_{B,i}}{N_{B,i}^2}\right)^2}\,, \tag{5.5}$$

assuming no statistical correlation between the generators. Bins with vanishing content are excluded from ratio plots.

The ratio transforms under the exchange $A \leftrightarrow B$,

$$R_i = \frac{N_{A,i}}{N_{B,i}} \xrightarrow{A\leftrightarrow B} R_i' = \frac{N_{B,i}}{N_{A,i}} = \frac{1}{R_i}. \tag{5.6}$$

On a logarithmic scale this corresponds to

$$\log R_i \xrightarrow{A\leftrightarrow B} -\log R_i, \tag{5.7}$$

i.e. a reflection about $\log R_i = 0$ ($R_i = 1$), which is the fixed point of the transformation. Values $R_i > 1$ ($R_i < 1$) indicate a relative excess of generator A (generator B) in bin i.

Assuming uncorrelated statistical uncertainties and Gaussian error propagation,

$$\Delta R_i = \sqrt{\left(\frac{\Delta N_{A,i}}{N_{B,i}}\right)^2 + \left(\frac{N_{A,i}\,\Delta N_{B,i}}{N_{B,i}^2}\right)^2}. \tag{5.8}$$

Using $R_i = N_{A,i}/N_{B,i}$ this can be written in relative form as

$$\Delta R_i = R_i \sqrt{\left(\frac{\Delta N_{A,i}}{N_{A,i}}\right)^2 + \left(\frac{\Delta N_{B,i}}{N_{B,i}}\right)^2}. \tag{5.9}$$

Under $A \leftrightarrow B$ one obtains

$$\Delta R_i \xrightarrow{A\leftrightarrow B} \Delta R_i' = \frac{\Delta R_i}{R_i^2}, \tag{5.10}$$

reflecting the nonlinearity of the inversion $R_i \mapsto 1/R_i$. While the absolute uncertainty is therefore not invariant, the relative uncertainty satisfies

$$\frac{\Delta R_i'}{R_i'} = \frac{\Delta R_i}{R_i}, \tag{5.11}$$

and is thus invariant under the exchange.

Exchanging numerator and denominator does not alter the statistical interpretation of the comparison. The transformation $R_i \to 1/R_i$ corresponds to a reflection about $R_i = 1$ (or $\log R_i = 0$), preserving the deviations in logarithmic space and their relative uncertainties. While the absolute uncertainty rescales, the relative uncertainty and the bin-wise assessment of compatibility with $R_i = 1$ remain unchanged. The choice of which generator appears in the numerator is therefore statistically arbitrary and affects only the visual representation, not the information content.

If a ratio value lies outside the interval (1/2, 2), this is indicated by a triangle pointing in the corresponding direction. The associated error bars are still shown if they extend into the interval (1/2, 2).

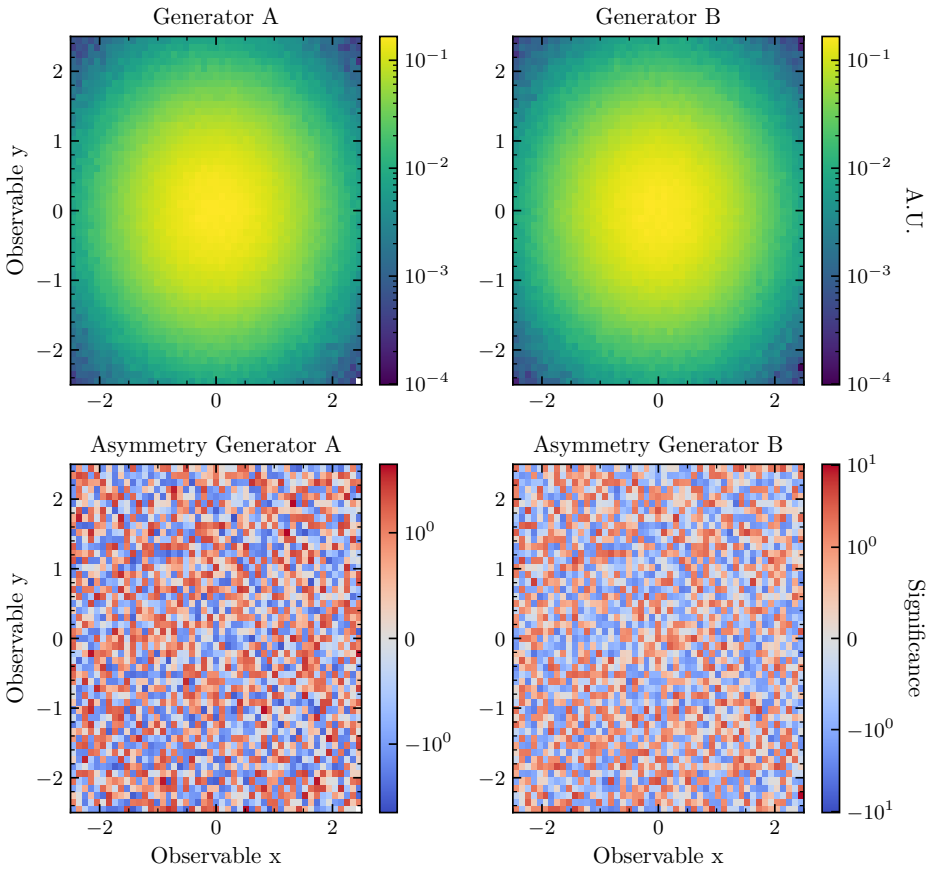

Figure 5.1.: Asymmetry plot obtained when using Gaussian distributions with $\sigma = 1$ and $\mu_A = \mu_B(0, 0)$. Upper left: event density for generator A. Upper right: event density for generator B. Lower left: asymmetry relative to generator A. Lower right: asymmetry relative to generator B.

5.5. Two-Dimensional Comparisons and Asymmetry Plots

To study differences in correlated observables, asymmetry maps are constructed. The asymmetry of distribution A with respect to B is defined bin-wise as

$$\mathcal{A}_{i,j} = \frac{N_{B,i,j} - N_{A,i,j}}{\sigma_{A,i,j}}\,, \tag{5.12}$$

where $N_{A,i,j}$ and $N_{B,i,j}$ are the normalized contents of the two-dimensional histograms and $\sigma_{A,i,j}$ is the statistical uncertainty of $N_{A,i,j}$.

Each bin of the asymmetry map thus represents the signed deviation between the two generators expressed in units of the statistical uncertainty of the reference

distribution A. Values $|\mathcal{A}| \approx 1$ correspond to deviations at the level of one standard deviation, while values close to zero indicate statistical compatibility. If both distributions match and for sufficiently large counts per bin, according to the central limit theorem, the asymmetry values do not show prominent structures but follow a Gaussian shape centred around zero.

An example asymmetry map obtained from identical input distributions is shown in Figure 5.1, while the case of different distributions is presented in Figure 5.2. The corresponding distribution of asymmetry values is displayed in Figure 5.3.

The asymmetry definition is not symmetric under the exchange of generators A and B because of the normalization to σ_A. As a result, $\mathcal{A}_{A \leftarrow B}$ and $\mathcal{A}_{B \leftarrow A}$ may differ substantially in magnitude. Such differences primarily reflect variations in the relative statistical precision of the two samples rather than inconsistencies in the underlying event generation. Consequently, a deviation is regarded as significant only if the asymmetry is large when evaluated with respect to both generator A and generator B.

The significance quantifies the level of compatibility between the two datasets and is strongly influenced by the event statistics in the corresponding phase-space bin. In particular, increasing the number of events in a given bin generally leads to a higher significance. Therefore, large significance values do not necessarily indicate large fractional differences between generators, but rather that one generator fails to reproduce the event yield predicted by the other within the available statistical precision in that region of phase space.

Negative asymmetry values indicate an excess of events relative to the chosen reference generator, whereas positive values correspond to a deficit.

For improved readability, asymmetry distributions are displayed on a symmetric logarithmic scale, with a linear region spanning the interval $(-1, 1)$.

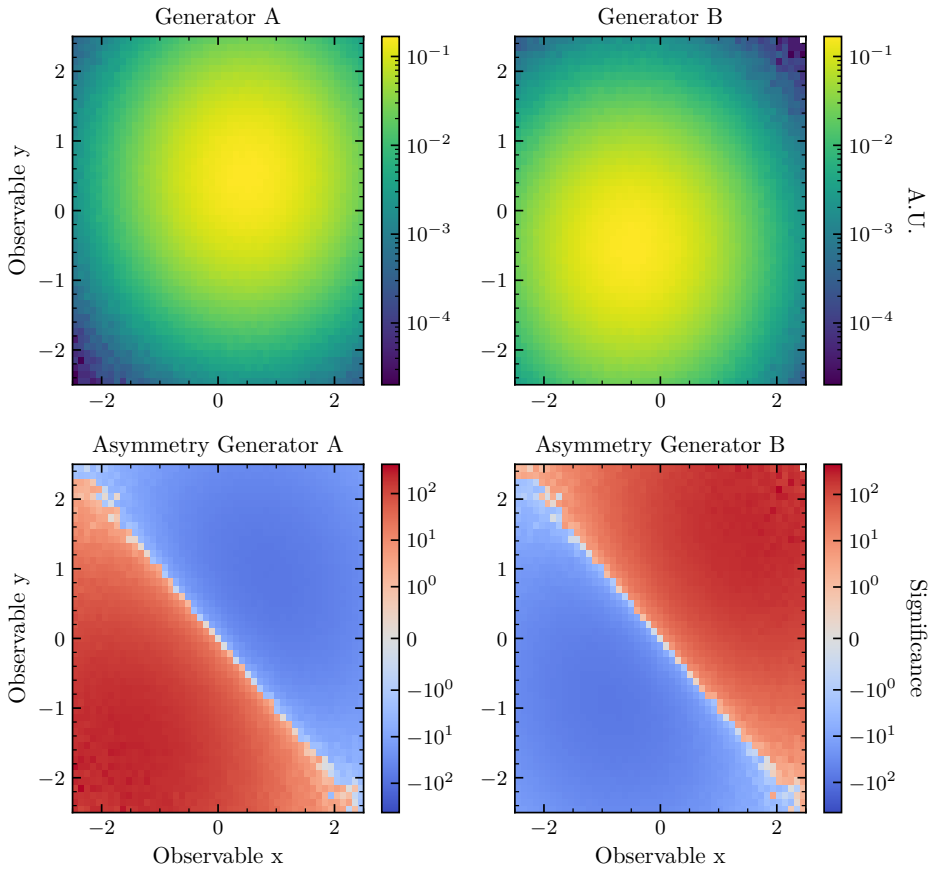

Figure 5.2.: Asymmetry plot obtained when using Gaussian distributions with $\sigma = 1$ and $\mu_A = (0.5, 0.5)$ and $\nu_B = (-0.5, -0.5)$. Upper left: event density for generator A. Upper right: event density for generator B. Lower left: asymmetry relative to generator A. Lower right: asymmetry relative to generator B.

5.6. Conditional Profiles

A profile is a plot that shows the average value of one quantity as a function of another variable, computed by grouping events into bins of the second variable and taking the mean in each bin.

Consider an event-level observable y, defined once per event. The observable is studied as a function of a control variable x. For each bin b in x, the quantity of interest is the conditional mean

$$\langle y \rangle_b \equiv \mathbb{E}[y \mid x \in b]. \tag{5.13}$$

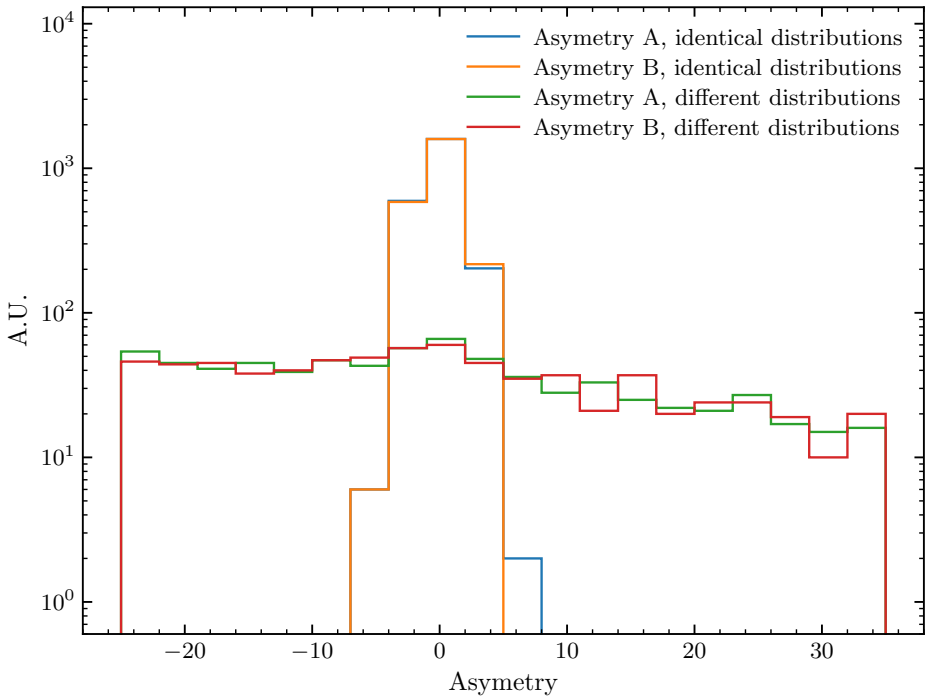

Figure 5.3.: Histogram of asymmetry values obtained from Figure 5.1 and Figure 5.2.

Each event contributes exactly one entry to the bin corresponding to its value of x. If n_b events fall into bin b and their observable values are $\{y_k\}_{k=1}^{n_b}$, the profile bin content is estimated as

$$\hat{\mu}_b \equiv \langle y \rangle_b \simeq \frac{1}{n_b} \sum_{k=1}^{n_b} y_k. \tag{5.14}$$

The statistical uncertainty on the estimated conditional mean is derived from the sample variance,

$$s_b^2 = \frac{1}{n_b - 1} \sum_{k=1}^{n_b} (y_k - \hat{\mu}_b)^2 \,, \tag{5.15}$$

yielding the standard error

$$\Delta\hat{\mu}_b = \frac{s_b}{\sqrt{n_b}} \qquad (n_b \geq 2), \tag{5.16}$$

while bins with insufficient population ($n_b < 2$) are left undefined. This estimator

assumes statistical independence of events and a binning in x fixed independently of the observed values of y.

If each event carries a statistical weight w_k, the conditional mean in bin b is defined as the weighted expectation

$$\langle y \rangle_b \equiv \frac{\mathbb{E}[w\, y \mid x \in b]}{\mathbb{E}[w \mid x \in b]}. \tag{5.17}$$

For a sample of n_b events in bin b with values $\{y_k, w_k\}_{k=1}^{n_b}$, the estimator becomes

$$\hat{\mu}_b^{(w)} = \frac{\sum_{k=1}^{n_b} w_k\, y_k}{\sum_{k=1}^{n_b} w_k}. \tag{5.18}$$

The corresponding weighted sample variance can be written as

$$s_{b,w}^2 = \frac{\sum_{k=1}^{n_b} w_k \left(y_k - \hat{\mu}_b^{(w)}\right)^2}{\sum_{k=1}^{n_b} w_k} \cdot \left(1 - \frac{\sum_{k=1}^{n_b} w_k^2}{\left(\sum_{k=1}^{n_b} w_k\right)^2}\right)^{-1}, \tag{5.19}$$

which reduces to the usual unbiased estimator for $w_k = 1$.

The statistical uncertainty on the weighted mean can be expressed in terms of the effective number of entries

$$n_{\mathrm{eff},b} = \frac{\left(\sum_{k=1}^{n_b} w_k\right)^2}{\sum_{k=1}^{n_b} w_k^2}, \tag{5.20}$$

yielding

$$\Delta\hat{\mu}_b^{(w)} = \frac{s_{b,w}}{\sqrt{n_{\mathrm{eff},b}}}. \tag{5.21}$$

The quantity $n_{\mathrm{eff},b} \leq n_b$ quantifies the loss of statistical power induced by weight fluctuations; equality holds only for uniform weights. As in the unweighted case, these expressions assume statistical independence of events and binning in x fixed independently of y.

Unlike histogrammed densities, no normalization factor related to the bin width enters these definitions, since the profile estimator targets the conditional expectation

$\mathbb{E}[y \mid x]$ rather than a probability density in x. Comparisons between models are therefore performed directly on the conditional means $\hat{\mu}_b$ and their associated uncertainties as functions of x.

6. Generator-Level Kinematic Comparisons

To characterize the differences between the neutrino event generators `km3neut` and `gSeaGen`, the comparison proceeds in three steps: first at the level of interaction cross sections, then in terms of distributions of relevant observables and their correlations, and finally with respect to particle multiplicities.

Studying these quantities prior to detector simulation isolates intrinsic model differences from detector and reconstruction effects, enabling a controlled assessment of how generator-dependent physics assumptions propagate through the simulation chain.

6.1. Cross Sections

The code used to obtain these results is available at [61]. The cross sections shown correspond to the predictions of the implemented interaction models; effective values after event selection may differ and can be modified by stochastic fluctuations during event generation as well as by failed or rejected generation attempts. The cross sections are extracted directly from `NEUT`, while the GENIE predictions used in `gSeaGen` are obtained from spline evaluations.

In the following, `NEUT` interaction modes are grouped according to Table B.1 and compared to their GENIE counterparts for hydrogen and oxygen targets. Representative grouped cross sections for `NEUT` RES and DIS interactions are shown in Figure 6.1. An example comparison is provided in Figure 6.2, and the complete set of cross-section plots is presented in section C.2. The discussion covers $E_\nu \in [0.1, 100]\,\mathrm{GeV}$ for ν_e and ν_μ, and $E_\nu \in [3.5, 100]\,\mathrm{GeV}$ for ν_τ.

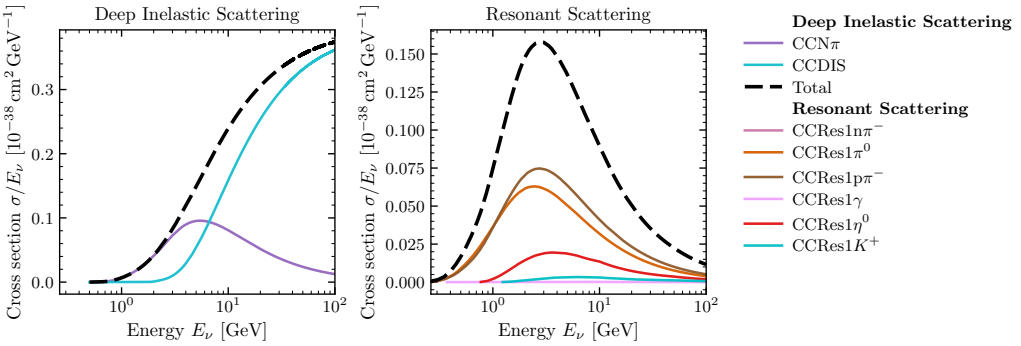

Figure 6.1.: Example of the composed `km3neut` cross section for ν_e scattering on hydrogen, for DIS (left) and RES (right) interactions.

Hydrogen and oxygen are used as effective proxies for sea water, as they constitute its dominant components and thus largely determine the overall cross-section behaviour.

6.1.1. Hydrogen

On free protons, the dominant model differences arise from the relative treatment of RES, DIS, and DIF. GENIE activates DIS at lower energies and predicts a substantially larger DIF component, while `NEUT` exhibits a delayed and strongly suppressed diffractive contribution. As a consequence, GENIE enhances the low- and intermediate-energy cross section in channels where RES and early DIS contribute, whereas `NEUT` overtakes at high energies due to its stronger DIS normalization.

For $\bar{\nu}_e$ and $\bar{\nu}_\tau$, the interplay between CCQE on free protons and DIS leads to multiple crossings of the total cross sections. `NEUT`s larger low-energy CCQE strength increases the cross section below a few GeV, while GENIE becomes dominant once DIS takes over. In the ν_τ sector, discrepancies up to $\mathcal{O}(15\%)$ around threshold energies indicate different treatments of the RES region and mass effects, directly impacting appearance-channel rates.

Overall, on hydrogen targets, the generators differ structurally: GENIE emphasizes early DIS onset and sizable diffraction, whereas `NEUT` enhances low-energy CCQE and high-energy DIS. These differences modify both normalization and inelasticity distributions in an energy-dependent manner.

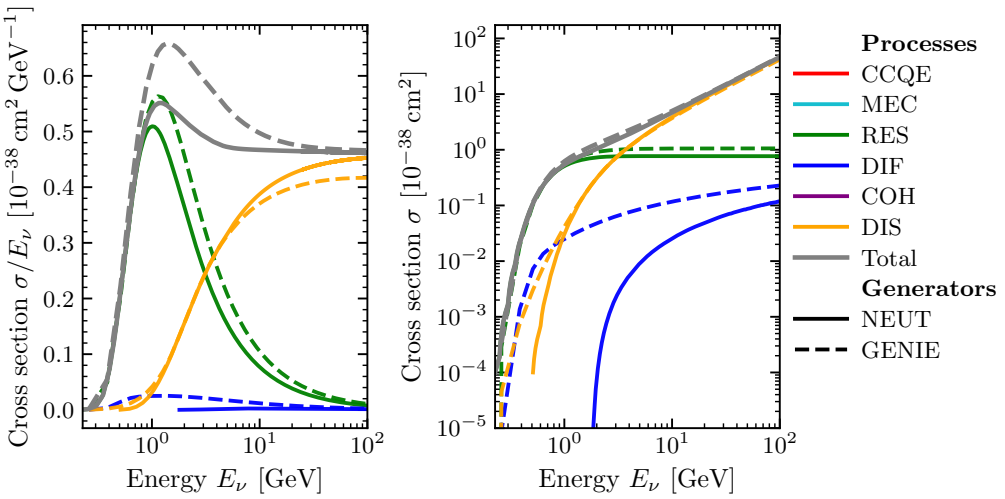

Figure 6.2.: Total charged-current cross section for electron neutrinos on hydrogen. Left: σ/E_ν in $10^{-38}\,\mathrm{cm}^2\,\mathrm{GeV}^{-1}$ versus E_ν in GeV. Right: σ in $10^{-38}\,\mathrm{cm}^2$ versus E_ν in GeV (logarithmic y-axis). The curves show the contributions from the different interaction categories and their sum, comparing `NEUT` (solid) and GENIE (dashed).

6.1.2. Oxygen

On oxygen, nuclear effects introduce additional model dependencies. For charged-current ν_e and ν_μ interactions, `NEUT` predicts a larger CCQE contribution, while GENIE supplements it with an explicit MEC component featuring a sharp threshold and termination. This produces step-like structures in the total cross section and enhances GENIE in the intermediate-energy region. Cross-section crossings around $\sim 25\,\mathrm{GeV}$ reflect different DIS normalizations and transition schemes.

For neutral-current interactions, the absence of MEC in `NEUT` yields systematically smaller cross sections below $\sim 700\,\mathrm{MeV}$ compared to GENIE. Differences are more pronounced in σ/E_ν, indicating modified energy scaling rather than simple normalization shifts. Across all channels, GENIE activates DIS at lower energies, while `NEUT` exhibits more pronounced internal structure, partly smoothed in the spline-based GENIE implementation used in `gSeaGen`.

6.1.3. Implications

In the ORCA energy range, spanning the RES-DIS transition and the τ production threshold, these structural differences propagate directly to rate predictions and inelasticity distributions. The enhanced RES and earlier DIS onset in GENIE increase event yields and shift the y distribution at intermediate energies, whereas `NEUT`s stronger high-energy DIS modifies the tail of the spectrum.

In the ν_τ appearance channel, generator differences at the level of $\mathcal{O}(10-15\%)$ can bias expected rates. For antineutrinos, the reduced model spread limits the impact, though the energy-dependent transition between CCQE and DIS remains relevant. In neutral-current channels, GENIEs larger DIF and earlier DIS enhance high-inelasticity configurations, potentially affecting flavour misidentification and background estimates. Since ORCA analyses rely on $\sigma(E_\nu)$ over a broad energy range in water, the treatment of MEC, the RES parametrization, and the DIS transition scheme must be incorporated as correlated systematic variations rather than absorbed into a single normalization uncertainty.

6.2. Kinematic Distributions and Generator-Level Observables

To suppress statistical fluctuations at generator level, dedicated high-statistics samples were produced using configurations identical to the nominal setup. For each neutrino flavour, 2 000 independent runs with 10^4 events per run were generated. The total number of events entering the generator-level analysis is summarized in Table 6.1.

Note that differences may originate not only from the generator itself but may also from the processing of `km3neut` events by `gSeaGen`, which places vertices and filters events that do not produce a detectable signature, meaning neither the vertex not a lepton is contained in the detector can. The following focuses on events with $3.5\,\mathrm{GeV} < E_\nu < 100\,\mathrm{GeV}$ for $\nu_\tau, \bar{\nu}_\tau$ and $1\,\mathrm{GeV} < E_\nu < 100\,\mathrm{GeV}$ otherwise.

Channel	km3neut	gSeaGen
ν_e	19 539 862	14 964 094
$\bar{\nu}_e$	17 012 365	14 967 335
ν_μ	3 820 737	1 614 790
$\bar{\nu}_\mu$	2 630 687	1 672 141
ν_τ	1 388 732	1 500 997
$\bar{\nu}_\tau$	1 244 303	1 531 324
ν_{NC}	15 504 962	14 963 310
$\bar{\nu}_{\mathrm{NC}}$	12 736 655	14 966 599

Table 6.1.: Total number of generated events entering the generator-level analysis.

A generator-level analysis of Bjorken-x and Bjorken inelasticity y is essential, as these variables encode the underlying interaction dynamics and nuclear modeling, directly constraining the partition of energy between the outgoing lepton and the hadronic system. The hadronic and lepton scattering angles determine the angular separation of final-state particles, which strongly affect light emission patterns and reconstruction performance.

The following discussion refers to DIS interactions for Bjorken-x, and to the full interaction sample for all other observables.

6.2.1. Bjorken x

The Bjorken-x distributions for DIS interactions, separated by current type and neutrino flavour, are shown in Figure 6.3.

For $x \gtrsim 0.6$, `km3neut` exhibits a markedly stronger suppression than `gSeaGen` for ν_e, ν_μ, and $\bar{\nu}_{\mathrm{NC}}$ interactions. The `km3neut`/`gSeaGen` ratio decreases monotonically toward $x \to 1$, indicating a reduced population of large parton momentum fractions in `km3neut`. In contrast, for ν_τ, $\bar{\nu}_\tau$, and ν_{NC} interactions, the distributions are shifted to higher x, with a suppression at low x and an enhancement around $x \simeq 0.7$ of up to a factor two, followed again by suppression at the kinematic endpoint. This non-uniform pattern implies flavor- and channel-dependent differences in the implementation of structure functions and the transition between shallow- and deep-inelastic regimes.

At low $x \lesssim 0.05$, `gSeaGen` consistently predicts higher rates across CC and NC

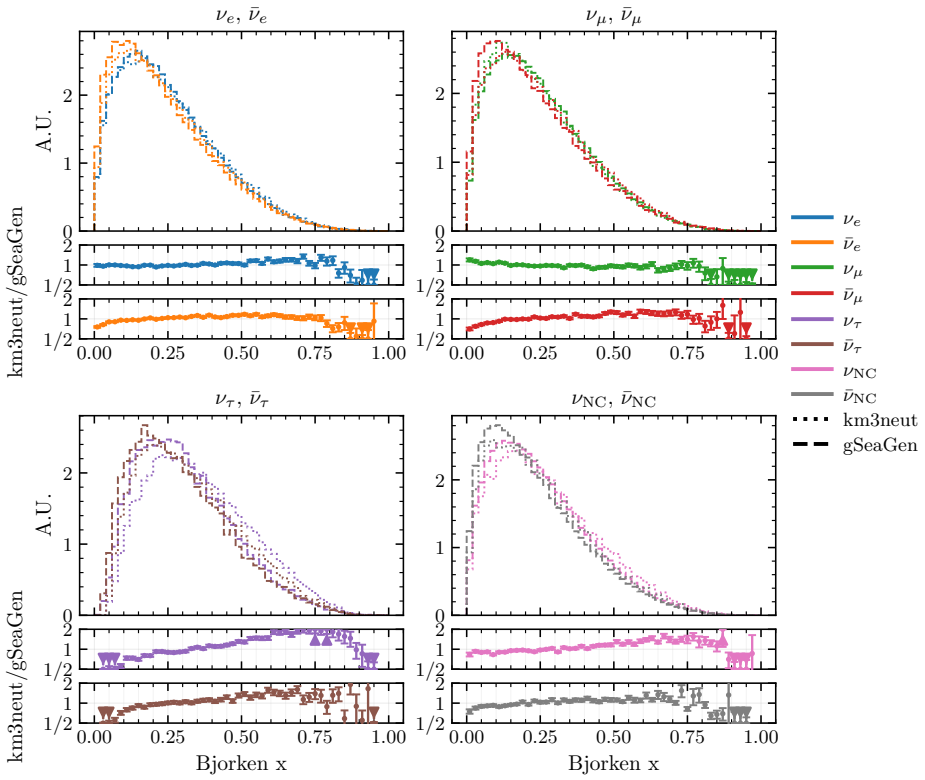

Figure 6.3.: Bjorken-x distributions for DIS interactions, separated by neutrino flavor for CC and for NC interactions. The lower panels show the ratio `km3neut/gSeaGen`.

channels. The persistence of this feature indicates a systematic difference in the treatment of small-x parton dynamics, rather than a statistical fluctuation.

Overall, `gSeaGen` populates both the low- and high-x extremes more strongly, whereas `km3neut` concentrates events in the intermediate-x region. Such differences modify the hadronic invariant mass and inelasticity distributions and therefore propagate to secondary-particle spectra and visible-energy deposition. A potential contributor is the distinct modelling of the shallow-inelastic-scattering regime in `km3neut` and the use of Pythia 5.7, compared to the `gSeaGen` configuration based on Pythia 8.3, implying generator-dependent hadronization dynamics.

A systematic suppression of high-x events ($x \gtrsim 0.6$) in `km3neut`for both CC and NC interactions, accompanied by an excess of very low-x events in `gSeaGen`, indicates materially different treatments of large momentum-fraction scattering and of the transition between the SIS and DIS regimes. Since high-x events correspond, at

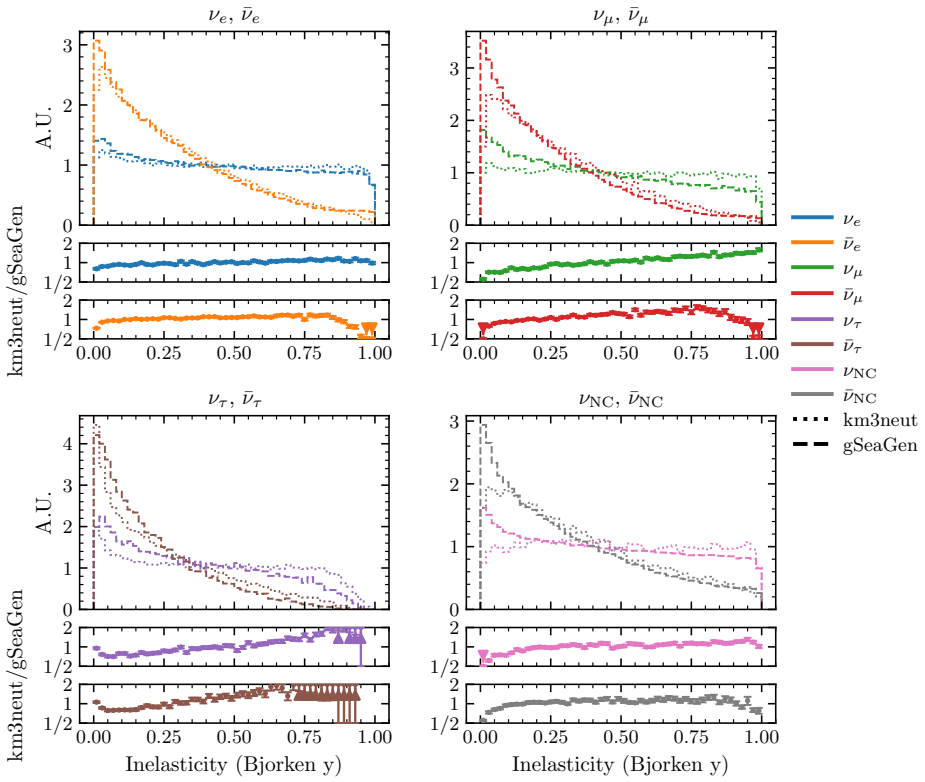

Figure 6.4.: Bjorken-y distributions for CC and NC interactions. The lower panels show the ratio `km3neut/gSeaGen`.

fixed neutrino energy, to larger momentum transfer Q^2 or lower inelasticity y, their suppression in `km3neut`reduces the population of interactions producing energetic and collimated hadronic systems.

6.2.2. Bjorken y

Figure 6.4 demonstrates that the generators predict systematically different inelasticity spectra across several channels, with implications beyond purely differential rate effects.

For CC $\bar{\nu}_e$, $\bar{\nu}_\mu$, and $\bar{\nu}_{\mathrm{NC}}$ interactions, `km3neut` yields a narrower y distribution, suppressing both low- and high-inelasticity events relative to `gSeaGen` and enhancing the intermediate region. This redistribution modifies the balance between leptonic and hadronic energy, directly affecting visible-energy calibration and reconstruction performance.

In the ν_μ channel, the y spectrum predicted by `km3neut` leads to a deficit over most of the inelasticity range and an excess at large y. Such a shift toward higher inelasticities implies a softer outgoing muon spectrum and increased hadronic energy deposition, with consequences for track length, angular resolution, and light yield. The compatibility of the ν_e distributions within uncertainties suggests that flavor-dependent modeling differences dominate the observed effects.

For NC interactions, the suppression of low-y events in `km3neut` indicates a global shift of hadronic energy toward higher fractions of E_ν. The absence of MEC contributions in `NEUT` and its presence in the `gSeaGen` configuration may further enhance this effect, altering the expected shower-energy response and flavor misidentification rates.

The most pronounced deviations occur in the ν_τ channel, where `km3neut` predicts systematically larger inelasticities. This enhances hadronic activity while softening the charged-lepton spectrum, potentially biasing energy reconstruction and flavour classification in a regime already limited by statistics.

Overall, generator-dependent y distributions modify the partition of neutrino energy between leptonic and hadronic components. This affects angular reconstruction, light production, and statistical neutrino-antineutrino separation. Consequently, such differences can propagate into oscillation parameter extraction, mass-ordering sensitivity, and searches for Beyond Standard Model (BSM) physics if not consistently modelled.

6.2.3. Lepton Scattering Angle

The lepton scattering-angle distributions, presented in Figure 6.5, reveal generator-dependent shape differences that are channel specific. For ν_e CC and $\bar{\nu}_{\mathrm{NC}}$ interactions, the agreement over the full angular range indicates consistent modelling of the underlying leptonic kinematics.

In contrast, sizable discrepancies occur for $\bar{\nu}_e$ and $\bar{\nu}_\mu$ at large scattering angles $\varphi > 1$, where `gSeaGen` predicts more than twice the rate of `km3neut`. For ν_μ, the

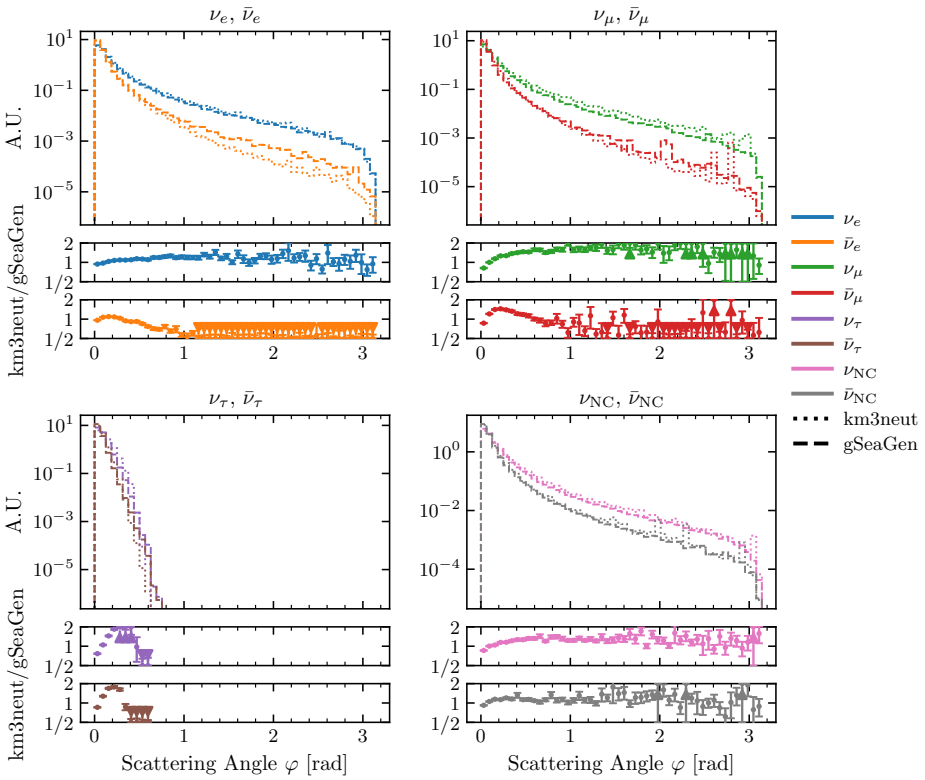

Figure 6.5.: Lepton scattering angle distributions for CC and NC interactions, summed over neutrinos and antineutrinos. The lower panels show the ratio `km3neut/gSeaGen`.

excess is reversed, with `km3neut` exceeding `gSeaGen` by up to a factor two. Beyond normalization effects, `km3neut` systematically depletes the first angular bin for ν_μ and $\bar{\nu}_\mu$, accompanied by an enhancement in the adjacent bins. This bin-to-bin redistribution broadens the effective angular response and points to differences in the treatment of momentum transfer and lepton kinematics. A similar, though weaker, pattern is observed for ν_{NC}, indicating that the effect is not limited to charged-current channels.

For ν_τ and $\bar{\nu}_\tau$, the sharp cutoff at $\varphi > 0.6\,\mathrm{rad}$ reflects kinematic constraints from the τ mass. In this region, the alternating over- and under-prediction by `km3neut` relative to `gSeaGen` suggests different implementations of threshold and phase-space effects. Given the direct relation between scattering angle and neutrino direction reconstruction, these generator-dependent distortions can propagate into angular

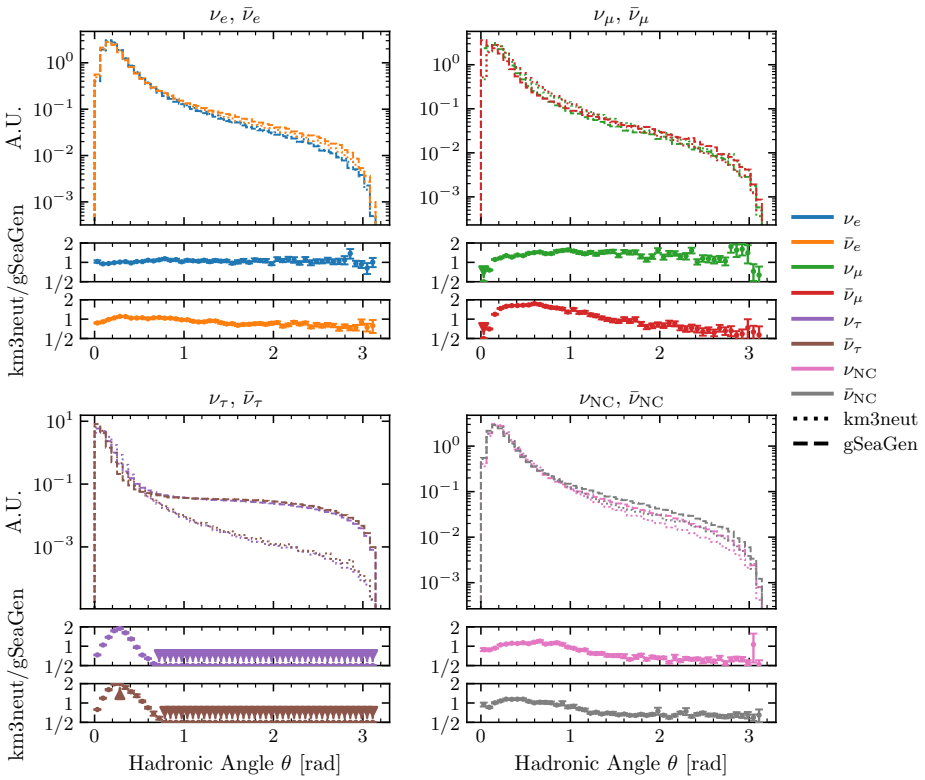

Figure 6.6.: Hadronic angle distributions for CC and NC interactions. The lower panels show the ratio `km3neut/gSeaGen`.

resolution and oscillation-sensitive observables.

6.2.4. Hadronic Angle

The hadronic-angle distributions are shown in Figure 6.6. Generator-dependent differences are most pronounced for NC interactions. For $\theta \gtrsim 1\,\text{rad}$, `gSeaGen` predicts up to twice the rate obtained with `km3neut`, implying systematically broader hadronic systems. Such differences directly affect the angular light pattern and may bias shower-direction reconstruction and flavor classification.

For ν_μ and $\bar{\nu}_\mu$ CC channels, both normalization and shape discrepancies are observed. The suppression at $\theta = 0$ indicates a reduced fraction of events with hadronic activity collinear to the charged lepton, altering the track–shower separation phase space. The opposite trends between ν_μ and $\bar{\nu}_\mu$ at large θ further point to model-dependent differences in hadronic recoil treatment, which can propagate to reconstructed zenith

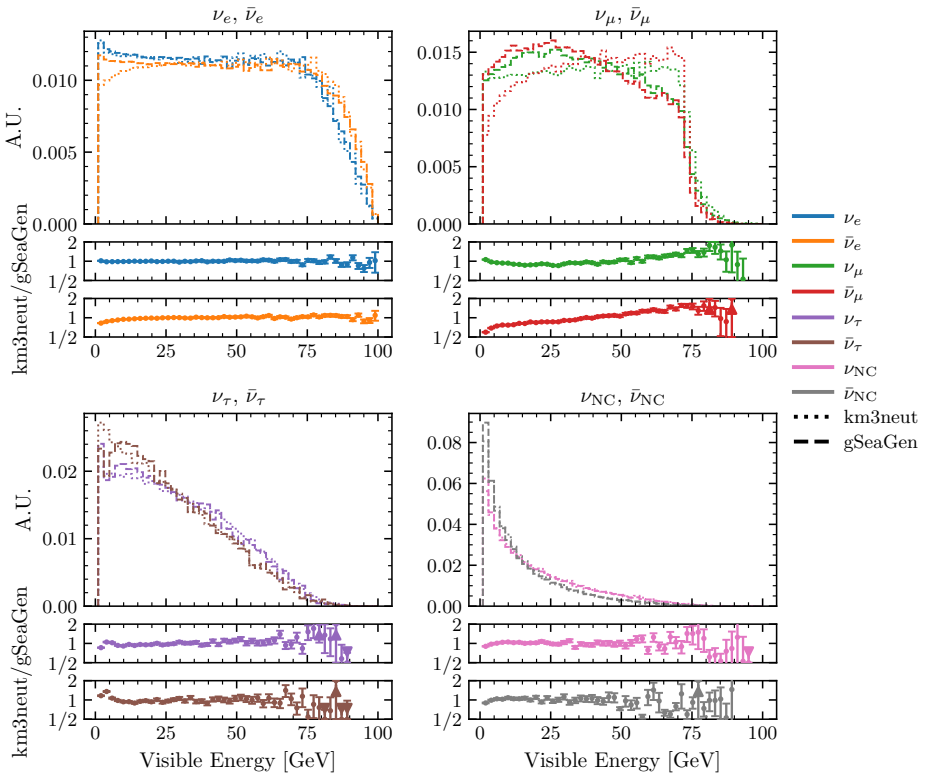

Figure 6.7.: Visible energy distributions for CC and NC interactions. The lower panels show the ratio `km3neut/gSeaGen`.

distributions and thus impact oscillation parameter inference.

The ν_e channel shows only minor deviations within uncertainties, suggesting limited sensitivity to the underlying hadronic model. In contrast, the ν_τ and $\bar{\nu}_\tau$ channels exhibit discrepancies of up to two orders of magnitude for $\theta \gtrsim 0.5\,\text{rad}$. Given that the default `NEUT` configuration lacks full support for ν_τ DIS interactions, these deviations likely reflect incomplete model coverage rather than physical differences.

6.2.5. Visible Energy

Figure 6.7 demonstrates that generator-dependent effects are channel specific. For NC interactions, the agreement in spectral shape implies a comparable modeling of hadronic energy deposition at the level relevant for E_{vis}. In contrast, the enhancement of high-E_{vis} events in ν_μ CC interactions for `km3neut` indicates a higher visible-energy response. This behavior points to differences in the treatment of the

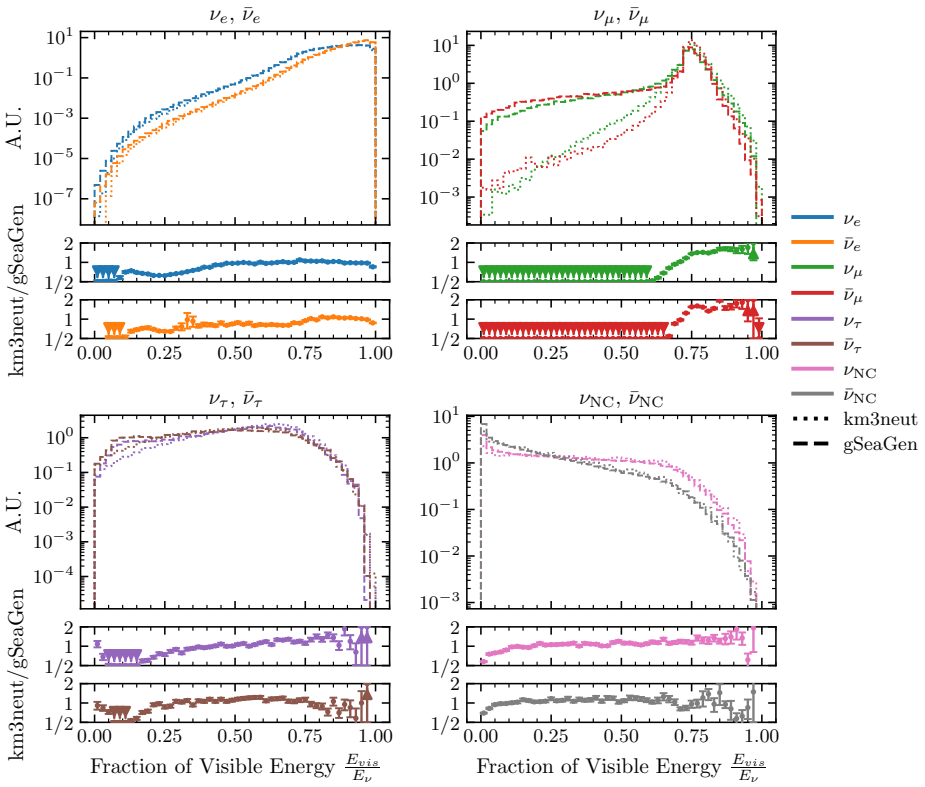

Figure 6.8.: Distribution of the fraction of visible energy E_{vis}/E_ν. The lower panels show the ratio `km3neut/gSeaGen`.

hadronic system and/or energy transfer at large momentum exchange. If confirmed with higher statistics, such a shift would bias reconstructed energy spectra and consequently affect oscillation parameter extraction.

For ν_τ interactions, the agreement below 50 GeV suggests no substantial difference in the bulk kinematics. At higher visible energies, the spectra are dominated by statistical fluctuations, preventing a quantitative comparison.

The distributions of E_{vis}/E_ν in Figure 6.8 provide a more differential view of energy transfer. The pronounced deficit of `km3neut` at low visible-energy fractions for ν_e and ν_μ CC interactions indicates a reduced probability for highly inelastic configurations compared to `gSeaGen`. Since low visible-energy fractions correspond to large invisible energy carried by hadrons or neutrinos, this discrepancy reflects systematic differences in the modeling of inelasticity and secondary particle production. Although the affected region contributes weakly to the total rate, its persistence

across flavors implies a structural generator effect.

For ν_μ CC interactions, the overall shift of the distribution toward larger visible-energy fractions in `km3neut` corresponds to a lower average inelasticity. This directly modifies the mapping between true and reconstructed neutrino energy and can induce a channel-dependent bias in oscillation analyses. The analogous but smaller shift for ν_e interactions suggests that the effect is interaction-model driven rather than reconstruction specific.

For ν_τ interactions, fluctuations dominate. The alternating excess between generators across E_{vis}/E_ν does not exhibit a coherent trend and remains statistically inconclusive, preventing a quantitative assessment of generator-induced biases in this channel.

6.3. Angular Correlations

This section compares two-dimensional correlations of kinematic observables predicted by `gSeaGen` and `km3neut`. All asymmetry distributions follow the definition in section 5.5. The discussion is restricted to statistically well-populated regions. Correlations between the hadronic angle and the charged-lepton scattering angle are shown for the combined $\nu + \bar{\nu}$ sample, as no appreciable neutrino-antineutrino differences are observed.

6.3.1. Electron Neutrino Charged-Current Interactions

The (y, θ) correlation in Figure 6.9 indicates a systematic shift of `km3neut` toward larger inelasticities across most angular bins, consistent with a harder hadronic energy fraction at fixed θ. The low-θ and $y < 0.6$ region shows no significant structure beyond statistical fluctuations, implying comparable modeling in the quasi-elastic and low-transfer regime. The enhancement at large y suggests differences in the treatment of multi-hadron final states.

In the (y, φ) plane (Figure 6.10), the diagonal structure reflects the underlying kinematic constraint between energy transfer and lepton deflection. The sign-

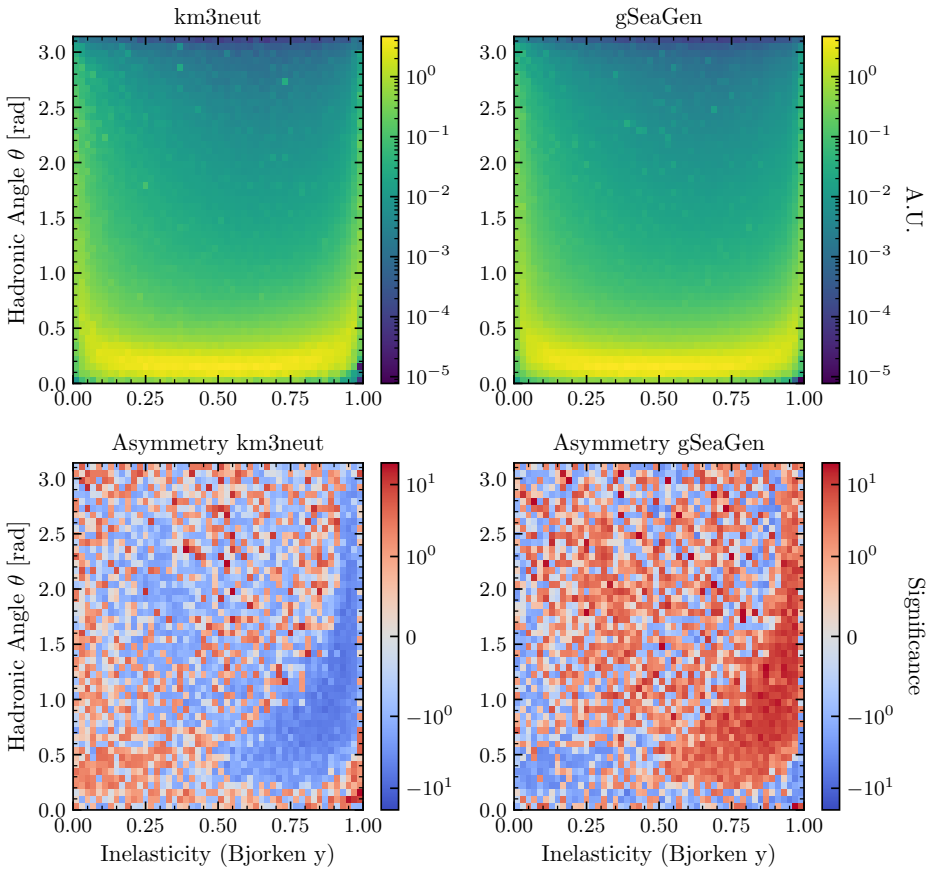

Figure 6.9.: Correlation between Bjorken-y and visible hadronic angle for ν_e CC interactions. Top row: event densities for `km3neut` and `gSeaGen`. Bottom row: asymmetries as defined in section 5.5. Upper left: event density for `km3neut`. Upper right: event density for `gSeaGen`. Lower left: asymmetry relative to `km3neut`. Lower right: asymmetry relative to `gSeaGen`.

changing excess indicates generator-dependent distortions of this mapping. The depletion of `km3neut` near the $y = 1$ boundary, together with its extension to larger φ at fixed $y < 0.5$, points to differences in the modeling of transverse momentum transfer. Conversely, the broader low-y coverage of `gSeaGen` at large φ implies a modified balance between longitudinal and transverse components of the hadronic current.

The (φ, θ) correlation (Figure 6.11) exhibits only weak structure, indicating approximate independence of lepton and hadronic angular observables for ν_e CC interactions. The localized `km3neut` excess near the identity line at small angles

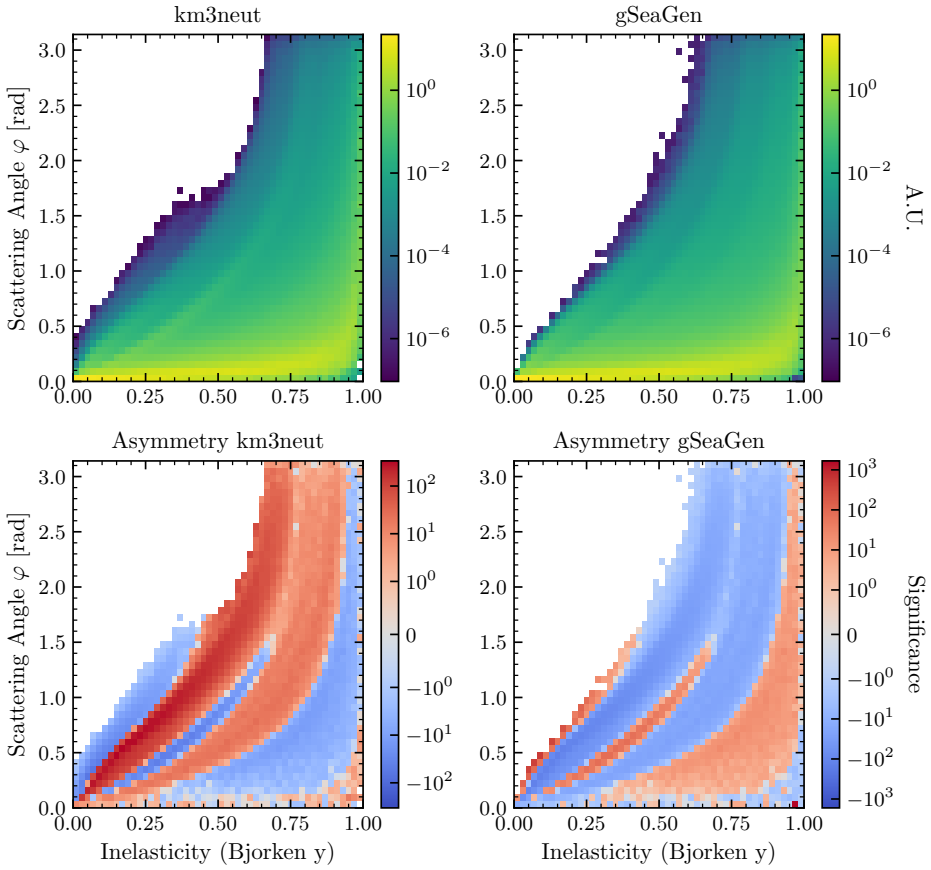

Figure 6.10.: Correlation between Bjorken-y and scattering angle for ν_e CC interactions. Upper left: event density for `km3neut`. Upper right: event density for `gSeaGen`. Lower left: asymmetry relative to `km3neut`. Lower right: asymmetry relative to `gSeaGen`.

suggests a tighter alignment of lepton and hadronic systems, potentially reflecting differences in final-state interaction modeling. Outside this region, the mild `gSeaGen` dominance does not reveal a strong dynamical correlation.

6.3.2. Muon Neutrino Charged-Current Interactions

For ν_μ CC interactions, the (y, θ) correlation (Figure 6.12) shows a systematic depletion of `km3neut` at $\theta \simeq 0$ over the full y range, indicating a reduced population of forward hadronic systems. Outside this region, `km3neut` exhibits an excess that is largely confined to sparsely populated areas of phase space and is therefore expected to have limited impact on integrated observables.

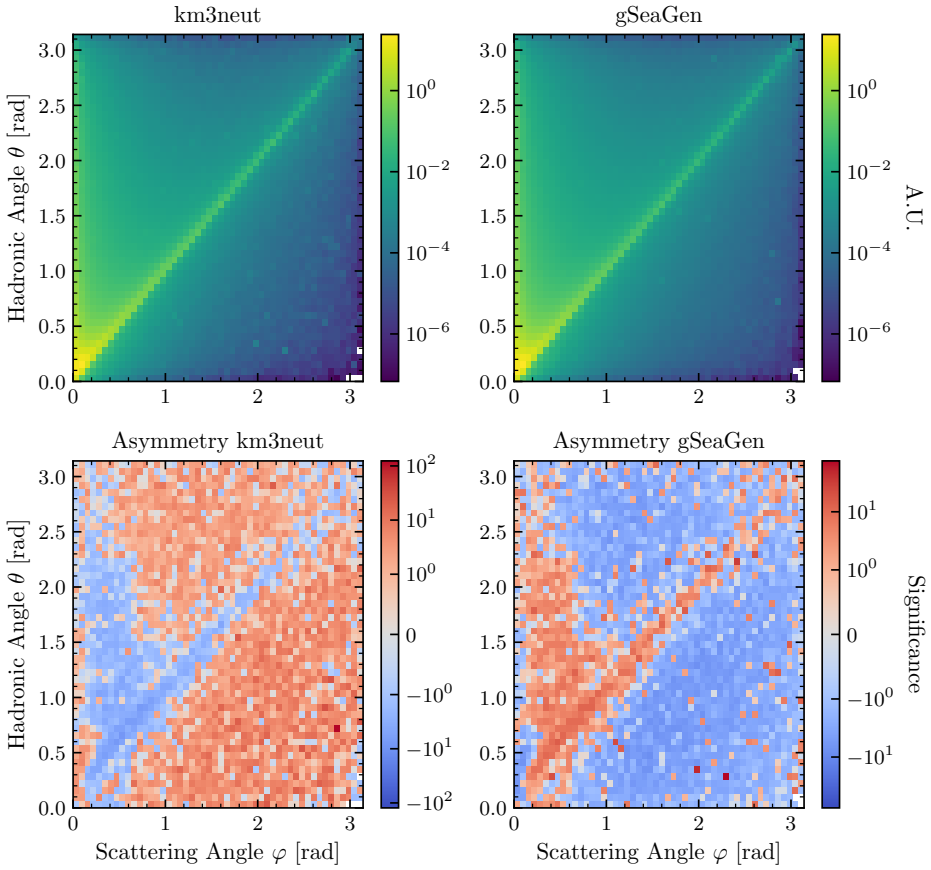

Figure 6.11.: Correlation between scattering and hadronic angles for ν_e CC interactions. Upper left: event density for `km3neut`. Upper right: event density for `gSeaGen`. Lower left: asymmetry relative to `km3neut`. Lower right: asymmetry relative to `gSeaGen`.

The (y, φ) distribution (Figure 6.13) follows the same kinematic diagonal as in the ν_e channel but with enhanced asymmetry. The extension of `km3neut` toward larger φ at fixed y points to differences in the modeling of transverse momentum transfer, which are more pronounced for muon kinematics.

In the (φ, θ) plane (Figure 6.14), `km3neut` is enhanced above the identity line ($\varphi < \theta$) and depleted below it, implying a systematic shift toward larger lepton–hadronic angles. The reduction of this excess at very large θ suggests convergence in the extreme angular regime.

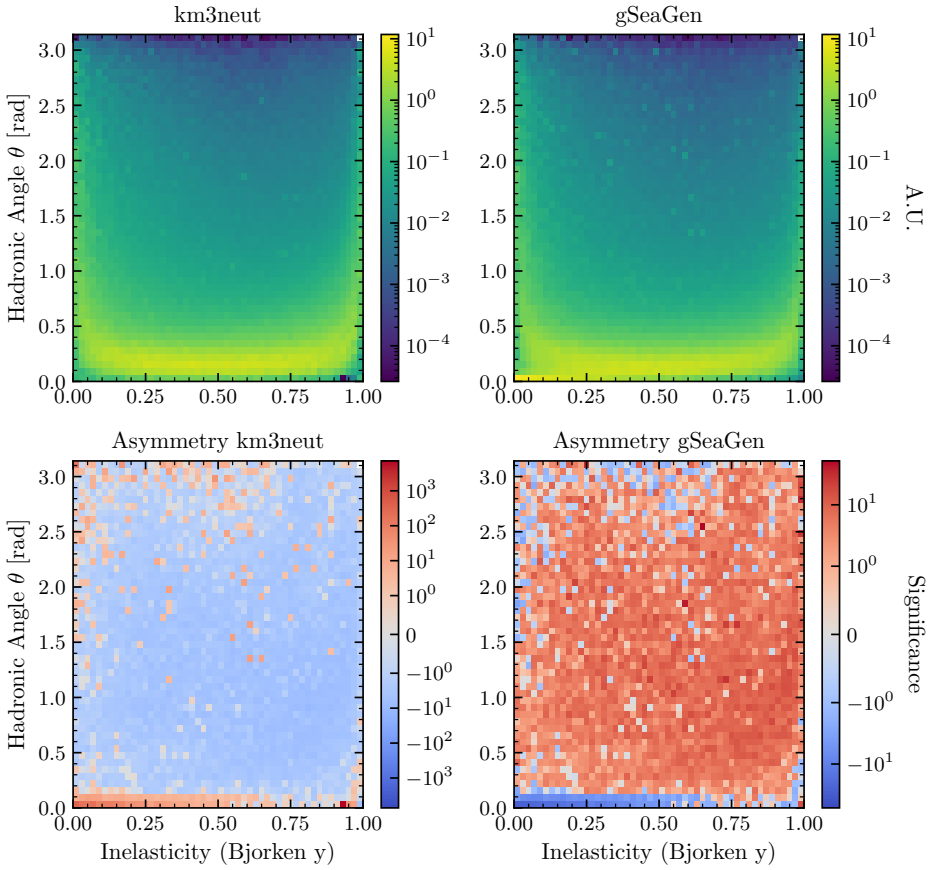

Figure 6.12.: Correlation between Bjorken-y and visible hadronic angle for ν_μ CC interactions. Upper left: event density for `km3neut`. Upper right: event density for `gSeaGen`. Lower left: asymmetry relative to `km3neut`. Lower right: asymmetry relative to `gSeaGen`.

6.3.3. Tau Neutrino Charged-Current Interactions

For ν_τ CC interactions, the (y, θ) correlation (Figure 6.15) is dominated by a pronounced `km3neut` depletion at $\theta \simeq 0$ and for $\theta > 0.7$ rad, largely independent of y. This indicates a generator-dependent suppression of both very forward and wide-angle hadronic systems, which drives the overall normalization difference rather than a modification of the y dependence.

In the (y, φ) plane (Figure 6.16), `km3neut` exhibits an excess at small φ for $y \gtrsim 0.26$, whereas `gSeaGen` dominates the lowest-y region. This pattern suggests differences in the modeling of the energy–angle correlation of the outgoing lepton, particularly in the intermediate inelasticity regime.

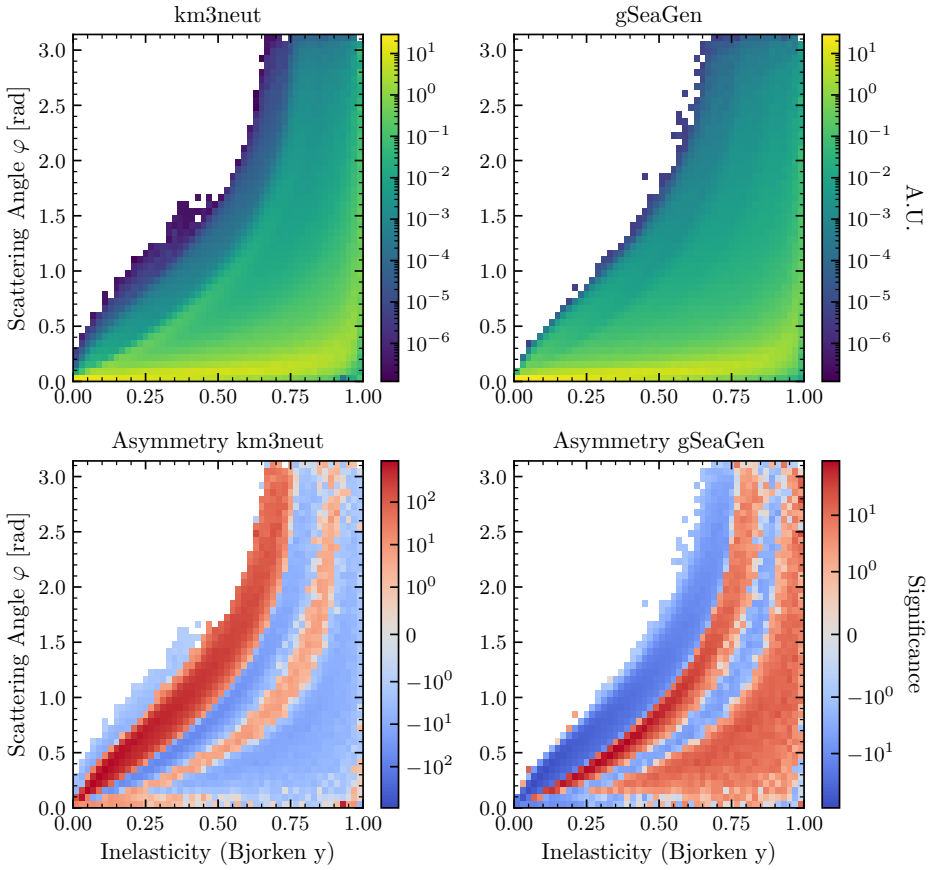

Figure 6.13.: Correlation between Bjorken-y and scattering angle for ν_μ CC interactions. Upper left: event density for `km3neut`. Upper right: event density for `gSeaGen`. Lower left: asymmetry relative to `km3neut`. Lower right: asymmetry relative to `gSeaGen`.

The (φ, θ) correlation (Figure 6.17) reflects these features: the asymmetry is approximately independent of φ, while a strong `km3neut` depletion persists for $\theta > 0.5$ rad and an excess is observed at smaller hadronic angles. The structure points to a systematic shift in the angular distribution of the hadronic system which was already seen in Figure 6.6.

6.3.4. Antineutrinos and Neutral-Current Interactions

The corresponding antineutrino channels exhibit qualitatively similar behavior. In particular, $\bar{\nu}_e$ and $\bar{\nu}_\mu$ reproduce the structures observed for ν_e and ν_μ, indicating that the underlying generator differences are not driven by the sign of the leptonic

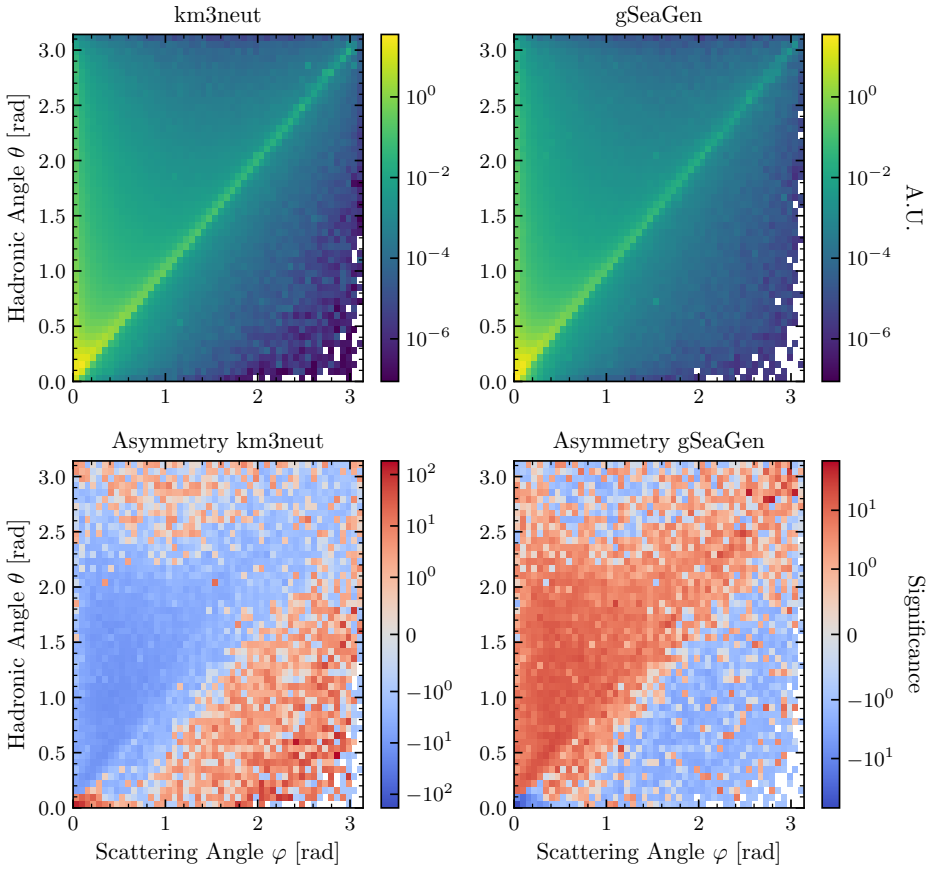

Figure 6.14.: Correlation between scattering and hadronic angles for ν_μ CC interactions. Upper left: event density for `km3neut`. Upper right: event density for `gSeaGen`. Lower left: asymmetry relative to `km3neut`. Lower right: asymmetry relative to `gSeaGen`.

current. The $\bar{\nu}_\tau$ channel mirrors the pronounced hadronic-angle depletion seen for ν_τ, confirming that this feature is intrinsic to the modeling of the hadronic system rather than specific to the lepton kinematics.

For NC interactions, `km3neut` shows a relative excess at large y, predominantly mapping into the region $\theta < 1$ rad, while `gSeaGen` dominates the complementary phase space. The (y, φ) and (φ, θ) correlations exhibit fewer pronounced stripe-like structures compared to CC channels, with alternating regions of generator dominance. This pattern suggests localized differences in hadronic modelling rather than a coherent shift of the global kinematic correlations.

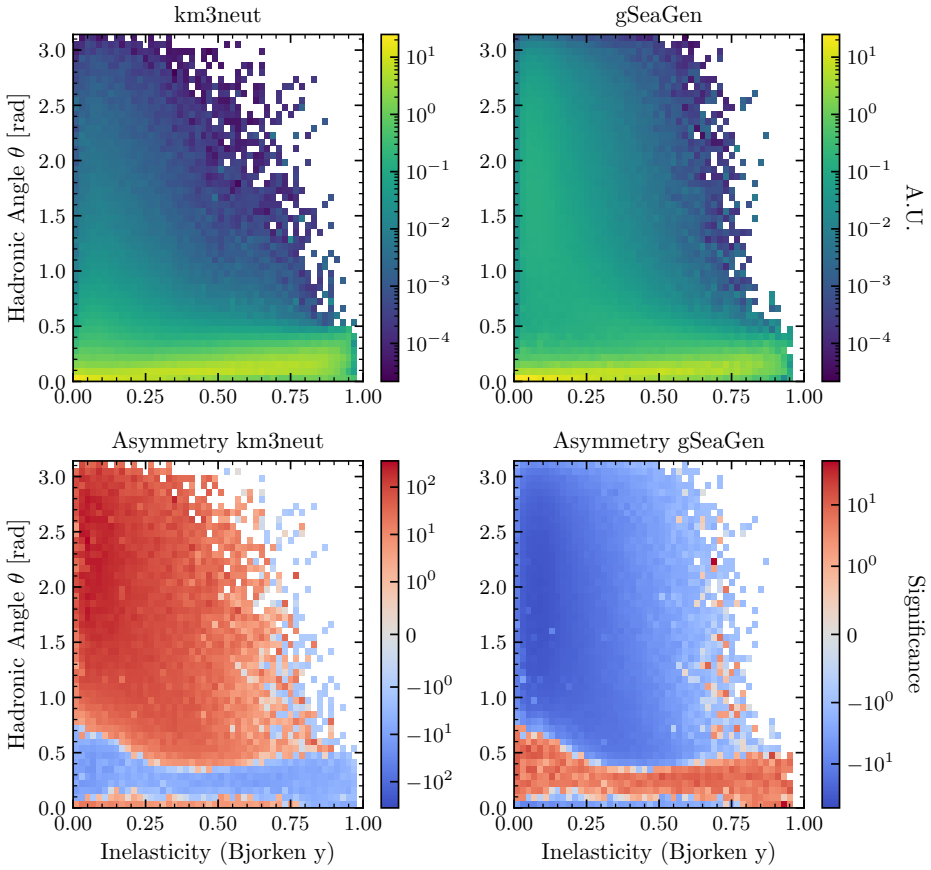

Figure 6.15.: Correlation between Bjorken-y and visible hadronic angle for ν_τ CC interactions. Upper left: event density for `km3neut`. Upper right: event density for `gSeaGen`. Lower left: asymmetry relative to `km3neut`. Lower right: asymmetry relative to `gSeaGen`.

6.4. Secondary Particle Multiplicities

The multiplicity of a given particle species is defined as the mean number of such particles produced per interaction within a fixed neutrino energy bin, according to section 5.6. In CC interactions, the charged lepton produced at the primary neutrino-nucleon vertex is excluded from this definition.

Across all interaction channels and neutrino flavours, the multiplicities exhibit a monotonic increase with neutrino energy, reflecting the growing hadronic invariant mass and the corresponding opening of additional fragmentation and resonance-production channels. While the absolute normalization differs between generators and flavours, the overall energy dependence is qualitatively consistent.

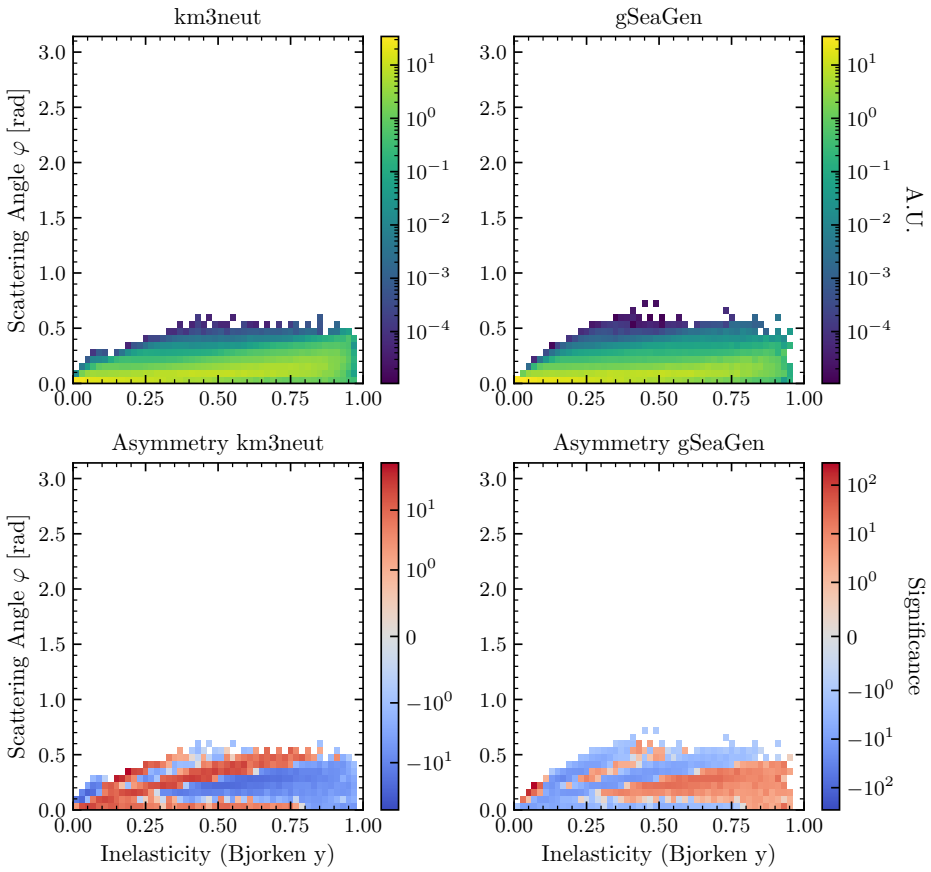

Figure 6.16.: Correlation between Bjorken-y and scattering angle for ν_τ CC interactions. Upper left: event density for `km3neut`. Upper right: event density for `gSeaGen`. Lower left: asymmetry relative to `km3neut`. Lower right: asymmetry relative to `gSeaGen`.

The multiplicities for charged-current interactions induced by electron neutrinos are shown in Figure 6.18, while the corresponding results for muon and tau neutrinos are presented in Figure 6.19 and Figure 6.20, respectively. Neutral-current interaction multiplicities are displayed in Figure 6.21.

Only neutrino-induced interactions are shown, as the antineutrino samples exhibit the same qualitative behaviour under charge conjugation. In particular, the energy dependence and relative differences between particle species and generators are preserved, with the roles of positively and negatively charged final-state particles interchanged.

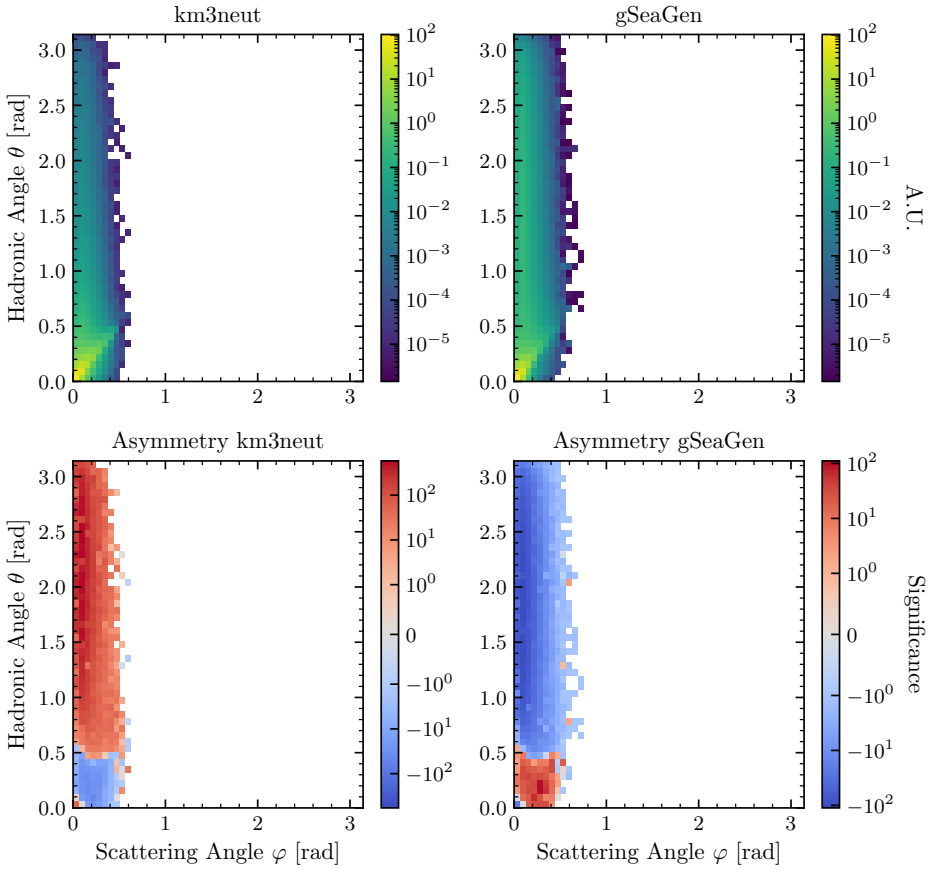

Figure 6.17.: Correlation between scattering and hadronic angles for ν_τ CC interactions. Upper left: event density for `km3neut`. Upper right: event density for `gSeaGen`. Lower left: asymmetry relative to `km3neut`. Lower right: asymmetry relative to `gSeaGen`.

6.4.1. Mesons

The pion-multiplicity distributions exhibit the expected charge hierarchy, with charged pions dominating over π^0, and an approximate $\pi^- \leftrightarrow \pi^+$ shape symmetry between neutrino and antineutrino samples, besides an overall lower normalization due to lower inelasticity.

For ν_e interactions, the charged-pion multiplicities predicted by `gSeaGen` and `km3neut` are consistent in shape, with a modest normalization excess in `km3neut`. In contrast, the systematically reduced π^0 yield in `km3neut` over the full energy range indicates generator-dependent differences in neutral-pion production, likely originating from resonance branching ratios and/or the treatment of FSI. Given

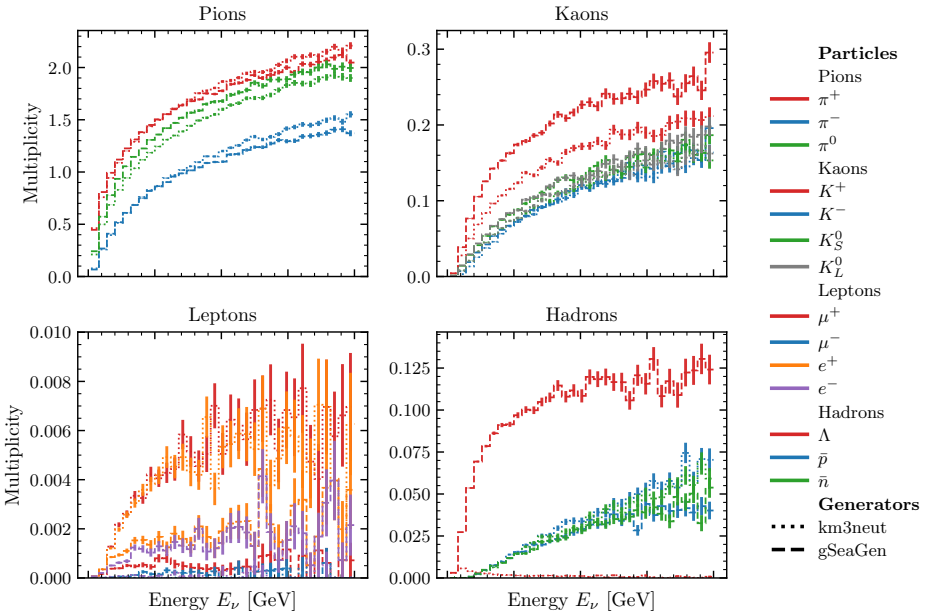

Figure 6.18.: Mean multiplicity of secondary particles produced in charged-current ν_e interactions as a function of the incoming neutrino energy E_{ν_e}. The horizontal axis shows the neutrino energy in GeV, while the vertical axes give the average multiplicity per interaction. Shown separately are pions (π^+, π^-, π^0), kaons (K^+, K^-, K_S^0, K_L^0), secondary leptons ($\mu^\pm$, $e^\pm$), and selected hadrons (Λ, $\bar{p}$, $\bar{n}$). Results from `gSeaGen` (dashed) and `km3neut` (dotted) are compared. The charged lepton produced at the primary interaction vertex is excluded.

the relevance of $\pi^0 \to \gamma\gamma$ for electromagnetic shower development, this discrepancy directly impacts visible energy reconstruction and flavour classification.

In the ν_μ channel, the agreement in π^0 production suggests comparable resonance modelling at intermediate energies. The divergence observed at $E_\nu \gtrsim 40\,\mathrm{GeV}$, together with the systematically enhanced π^+ yield in `km3neut`, points to differences in the DIS hadronization model. This affects the charged-hadron content of events and can modify track–shower separation and energy-scale systematics at high energies.

For ν_τ interactions, pion production receives a significant secondary contribution from τ decays, enhancing all pion species. The systematically larger multiplicities predicted by `km3neut` at high energies, reaching $\mathcal{O}(20\%)$, imply generator-dependent modelling of both primary hadronization and τ decay handling. Such differences

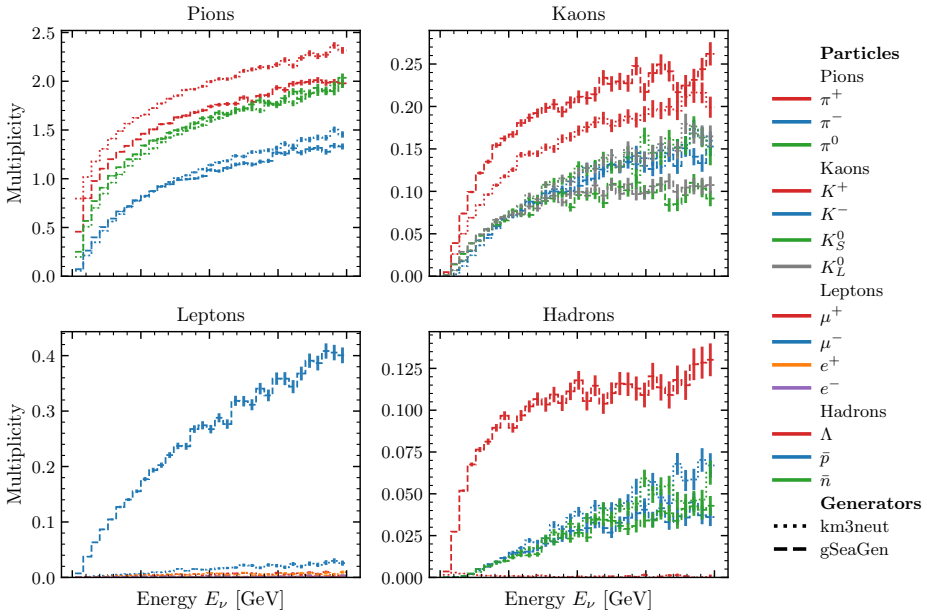

Figure 6.19.: Mean multiplicity of secondary particles in charged-current ν_μ interactions as a function of the neutrino energy E_{ν_μ}.

propagate to the hadronic energy fraction and thus to reconstructed inelasticity.

In NC interactions, the relative suppression of π^0 and π^- accompanied by a mild π^+ excess in `km3neut` indicates altered charge partitioning in the hadronic system. Since NC events are reconstructed solely via hadronic activity, these differences translate directly into visible-energy and flavour-dependent systematics.

Kaon multiplicities are substantially lower than pion multiplicities and increase with neutrino energy in all channels, consistent with the higher production threshold for strange hadrons. Relative generator differences are more pronounced than for pions, indicating enhanced sensitivity to the modelling of strangeness production.

Across all channels, `km3neut` predicts systematically reduced K^+ yields compared to `gSeaGen`, with deviations increasing towards higher energies. This behaviour points to differences in strange-quark production and fragmentation in the DIS regime. The suppression in `km3neut` implies a comparatively softer or less strangeness-rich hadronization model.

For ν_e, ν_μ, and ν_τ CC interactions, the remaining kaon species are consistent within statistical uncertainties. In contrast, for ν_{NC} interactions, all kaon multiplicities are

reduced in `km3neut`, indicating generator-dependent differences in purely hadronic final states that directly affect the visible hadronic energy component.

6.4.2. Leptons

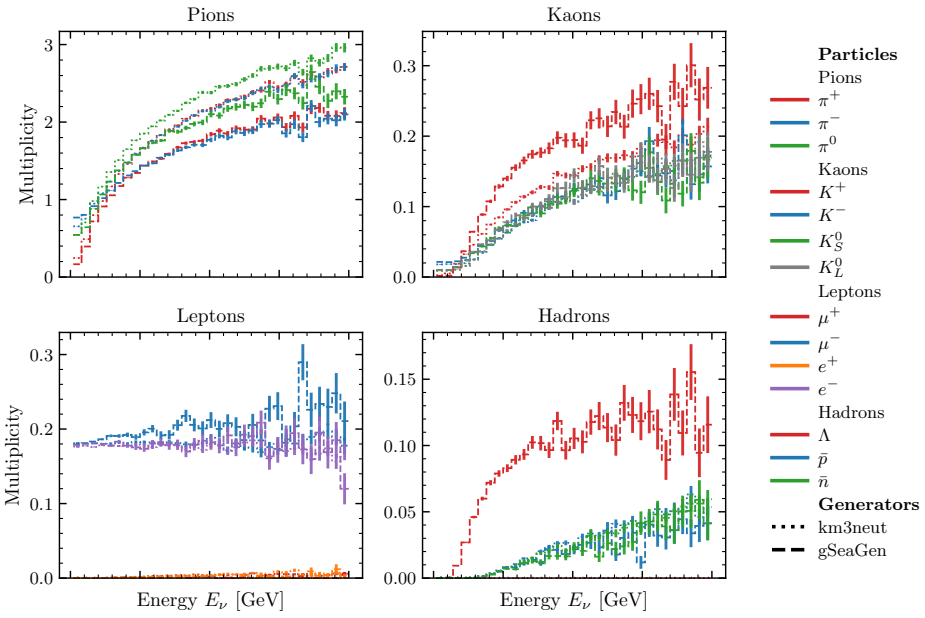

Figure 6.20.: Mean multiplicity of secondary particles in charged-current ν_τ interactions as a function of the neutrino energy E_{ν_τ}.

Secondary lepton production is strongly suppressed relative to hadron production and arises predominantly from decay chains rather than primary interaction vertices. For ν_e interactions, `km3neut` predicts an enhanced yield of secondary μ^+ and e^+, accompanied by a deficit in e^-. The corresponding antineutrino samples exhibit the expected charge-conjugated pattern. This charge asymmetry indicates generator-dependent differences in meson production and decay cascades, in particular in the balance of $\pi^\pm$ and $K^\pm$ contributions.

In the ν_μ channel (and analogously for $\bar{\nu}_\mu$), `km3neut` produces fewer secondary muons by up to an order of magnitude relative to `gSeaGen`. However, the absolute multiplicities remain at the percent level of total events, such that no significant modification of the global event shape or reconstruction performance is expected.

For ν_τ interactions, the secondary lepton yields agree within statistical uncertainties,

indicating comparable treatment of τ decay chains.

In NC interactions, `km3neut` predicts an increased production of secondary electrons and positrons relative to `gSeaGen`. Given that the absolute rates remain at the per-mille level, the phenomenological impact on reconstruction and classification is negligible.

6.4.3. Hadrons

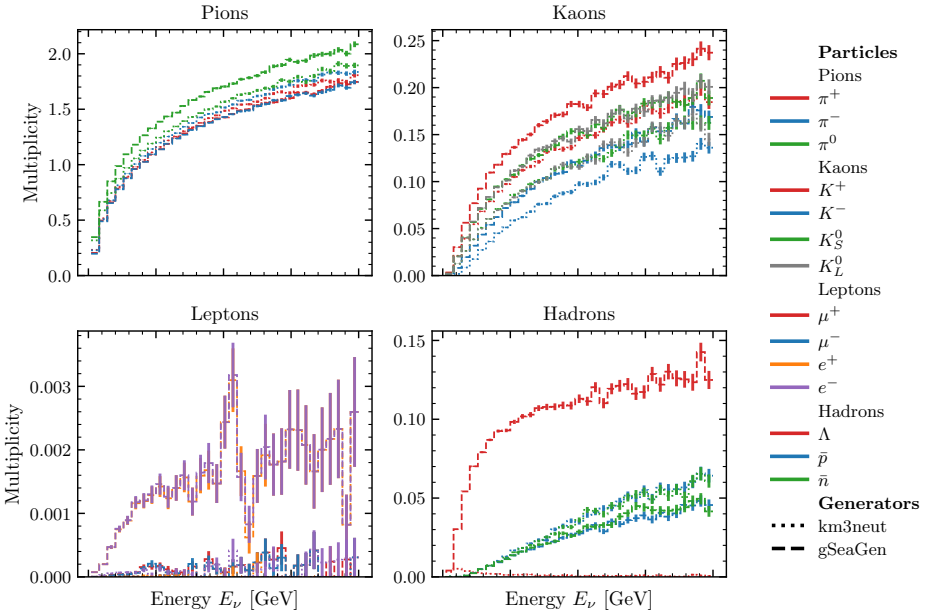

Figure 6.21.: Mean multiplicity of secondary particles in neutral-current neutrino interactions as a function of the neutrino energy E_ν^{NC}.

The largest generator discrepancy is observed in Λ production. Except for contributions from kaon-resonant channels, Λ hyperons are essentially absent in `km3neut` and arise only from RES-K processes. This results in an order-of-magnitude deficit relative to `gSeaGen` across all flavours and energies, indicating a missing or strongly suppressed strange-baryon production mechanism in `km3neut`.

This behaviour is consistent with the reduced kaon yields in `km3neut` and suggests an overall suppression of $s\bar{s}$ pair production during hadronization. The observed difference for kaon and Λ yields therefore reflects a generator-dependent treatment of strangeness partitioning between mesons and baryons.

Antiprotons and antineutrons probe hadronization independently of primary nucleon knockout, since at the interaction level ejected and newly produced nucleons cannot be distinguished. In contrast to the Λ deficit, the antinucleon production rates are comparable in `km3neut` and `gSeaGen`, indicating that baryon–antibaryon pair production is treated consistently and that the discrepancy is specific to strange-baryon channels.

6.5. Event-level consequences for ORCA

The event-level comparison between `gSeaGen` and `km3neut` demonstrates that their differences cannot be reduced to an overall normalization or a simple energy-dependent reweighting but instead arise from kinematics-dependent distortions across the phase space. These distortions affect Bjorken x and y, the mapping of momentum transfer into lepton and hadronic angles, the partition of visible energy between leptonic and hadronic systems, and the detailed hadronization and fragmentation content. For ORCA, whose reconstructed observables are driven primarily by event categorization, directionality, and energy-inelasticity rather than exclusive final-state reconstruction, such correlated differences propagate directly into oscillation sensitivities and into the structure of dominant systematic uncertainties. Bjorken y constitutes the most direct handle on ORCA reconstruction, and the observed generator differences therefore have immediate experimental consequences. `km3neut` exhibits a narrowed y spectrum for CC ν_e and ν_μ interactions, with suppression at both low and high y and enhancement at intermediate values, a strong suppression of low-y NC events, and pronounced flavour-dependent distortions for ν_τ, characterized by excesses at high y and deficits at low to intermediate y. Because inelasticity governs the energy sharing between the outgoing lepton and the hadronic system, these differences directly alter the balance between track-dominated and cascade-dominated events, the visible-energy response due to different leptonic and hadronic light yields and resolutions, and the effective angular resolution. In particular, the depletion of low-y CC ν_μ and excess of high y CC ν_μ interactions

in `km3neut` implies fewer events with energetic muon tracks carrying most of the neutrino energy, leading to a relative enhancement of hadronic contributions to the reconstructed energy scale, and modified migration between track and cascade classifications. For NC interactions, the suppression of low-y events reduces the population with very small visible energy, hardens the visible-energy spectrum near analysis thresholds, and changes the NC contamination of oscillation samples. Because NC events intrinsically involve missing energy, their generator-dependent y distributions constitute a first-order systematic in ORCA modelling.

The ν_τ channel displays particularly severe anomalies in `km3neut`, including an order-of-magnitude deficit in the hadronic-angle distribution at large angles and systematically higher inelasticity. These features are incompatible with statistical fluctuations and instead point to limitations in the modelling or implementation of ν_τ interactions, potentially composed by limited validation of unmodified `NEUT` configurations[1]. Since ORCAs ν_τ appearance sensitivity relies on predicting the rate, and kinematics of τ-induced cascades from atmospheric $\nu_\mu \to \nu_\tau$ oscillations, distorted angular and inelasticity distributions directly bias zenith-angle spectra and reconstructed-energy distributions.

Large and systematic discrepancies in the hadronic scattering angle, particularly for NC interactions and most strongly for ν_τ, further reveal differences in transverse-momentum balance and in the modelling of hadronization and FSI. While `gSeaGen` predicts enhanced populations at both very small and very large hadronic angles, `km3neut` produces a more forward-peaked hadronic system. In ORCA, where hadronic-direction reconstruction limits the performance for cascades and NC events, such differences translate into generator-dependent angular-resolution, altered spatial light distributions that affect reconstruction and quality selections, and selection-dependent biases that amplify underlying modelling discrepancies.

Visible-energy observables provide an additional manifestation of these effects. Although the absolute E_{vis} shapes for CC interactions are broadly similar, `NEUT`

[1] Addendum: Conversations AFTER the submission of this thesis confirmed that SK modifies/wraps NEUT to enable the simulation of ν_τ.

shows a deficit at low E_{vis}/E_ν for ν_e and ν_μ, reaching up to an order of magnitude in that region, while for NC interactions `gSeaGen` predicts enhanced high-E_{vis} tails. A deficit at low visible-energy fractions in CC interactions implies fewer events in which a large fraction of the neutrino energy is invisible to the detector response, whereas differences at high visible energy for NC interactions reflect altered high-y behaviour and hadronic energy deposition. Because ORCA oscillation analyses depend critically on the mapping between reconstructed and true neutrino energy, disagreements in the tails of E_{vis}/E_ν may shift reconstructed-energy spectra.

These effects are amplified by observed discrepancies that are correlated rather than purely one-dimensional. Generator-dependent structures in multidimensional distributions, such as correlations between y and scattering or hadronic angle, indicate coupled modelling differences.

Finally, substantial differences in hadronization, particularly in strangeness and baryon production, further affect the detector response. `NEUT` exhibits systematically lower kaon yields and a strong suppression of Λ production, indicating materially different treatments of strange and baryonic channels. In a Cherenkov detector, the hadronic particle content influences both the total light yield and its temporal and spatial development; long-lived neutral kaons transport energy further before interacting, while strange baryons and antibaryons modify cascade development and secondary particle production. Although these effects may be subdominant in inclusive spectra, they may be significantly amplified by reconstruction and selection procedures.

7. Light Propagation Comparisons

This chapter describes the light-stage comparison between `km3neut` and `gSeaGen`. All results refer to observables evaluated after light propagation, not including trigger efficiencies or PMT response effects. Due to insufficient statistical precision in the light-stage samples $\nu_\tau/\bar{\nu}_\tau$ are excluded.

The analysis focuses on detector-level observables that directly characterize the optical response: the total number of photons reaching the photocathode, timing observables derived from the photon time distribution (first-photon arrival time t_{first}, last-photon arrival time t_{last}, and event timespan $\Delta t = t_{\text{last}} - t_{\text{first}}$), the number of hit PMTs, and the decomposition of detected photons by the particle species responsible for their production. For a fixed deposited energy, an average number N of detected photons is attributed to the initiating particle. Photons produced by tertiary particles are assigned to their primary progenitor and are not treated as independent contributions, the calculation follows section 5.6.

7.1. Light-Stage Observables and Event Reweighting

To compare generators at fixed interaction phase space, events are reweighted with the interaction-probability scale p_S and an energy factor consistent with Equation 4.3. The interaction-probability scale is defined as the interaction probability p along the simulated neutrino trajectory within the detector volume, normalized to the maximum interaction probability $p_{\max}$. The final event weight is

$$w(E, p) = p_S(p) \cdot \mathrm{EG}(E) = \frac{p}{p_{\max}} \mathrm{EG}(E) \tag{7.1}$$

where w denotes the final event weight.

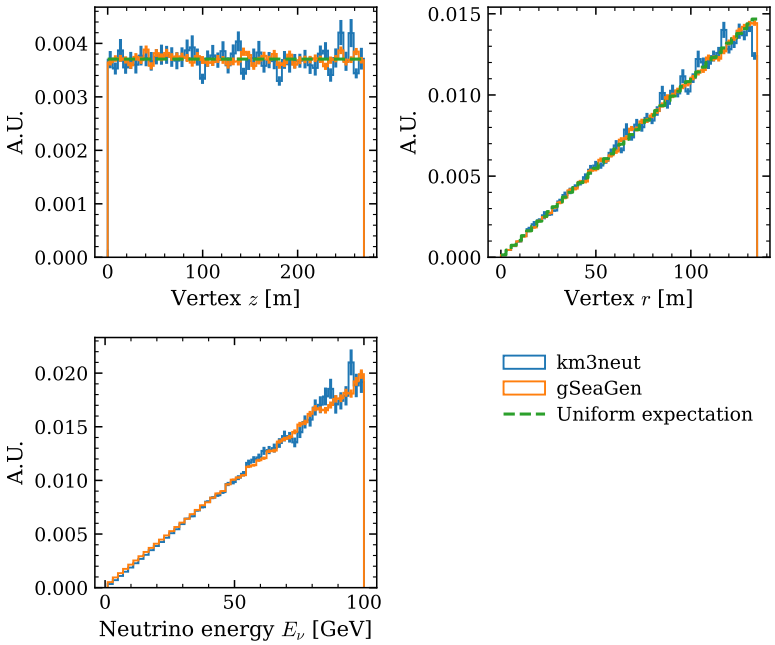

Figure 7.1.: Example of the normalization procedure applied in the light-stage analysis, shown for a combined sample of ν_e, $\bar{\nu}_e$, and NC interactions. Reweighted distributions of the interaction vertex position along the detector axis z, the transverse radius $r = \sqrt{x^2 + y^2}$, and the neutrino energy E_ν are compared between `km3neut` and `gSeaGen`. Dashed curves indicate the expectation for a uniform interaction density within a cylindrical detector volume. Vertex coordinates are centred by subtracting constant offsets $\Delta x = 477.0\,\mathrm{m}$ and $\Delta y = 552.3\,\mathrm{m}$.

This procedure enforces a matched neutrino-energy distribution between `km3neut` and `gSeaGen`, and an approximately uniform interaction-vertex distribution within the detector volume, enabling generator comparisons in optical observables. An example of the resulting reweighted vertex and energy distributions is shown in Figure 7.1.

This reweighting does not preserve a uniform neutrino-energy spectrum; the effective distribution scales as $\sigma(E)$, enhancing the relative contribution of high-energy interactions and shifting the normalization toward large E. The corresponding increase in statistical uncertainties at high energies implies that the overall statistical sensitivity remains dominated by low-energy interactions. The induced energy-dependent normalization biases the comparison toward high energies;,this effect is not corrected for and is neglected in the present interpretation.

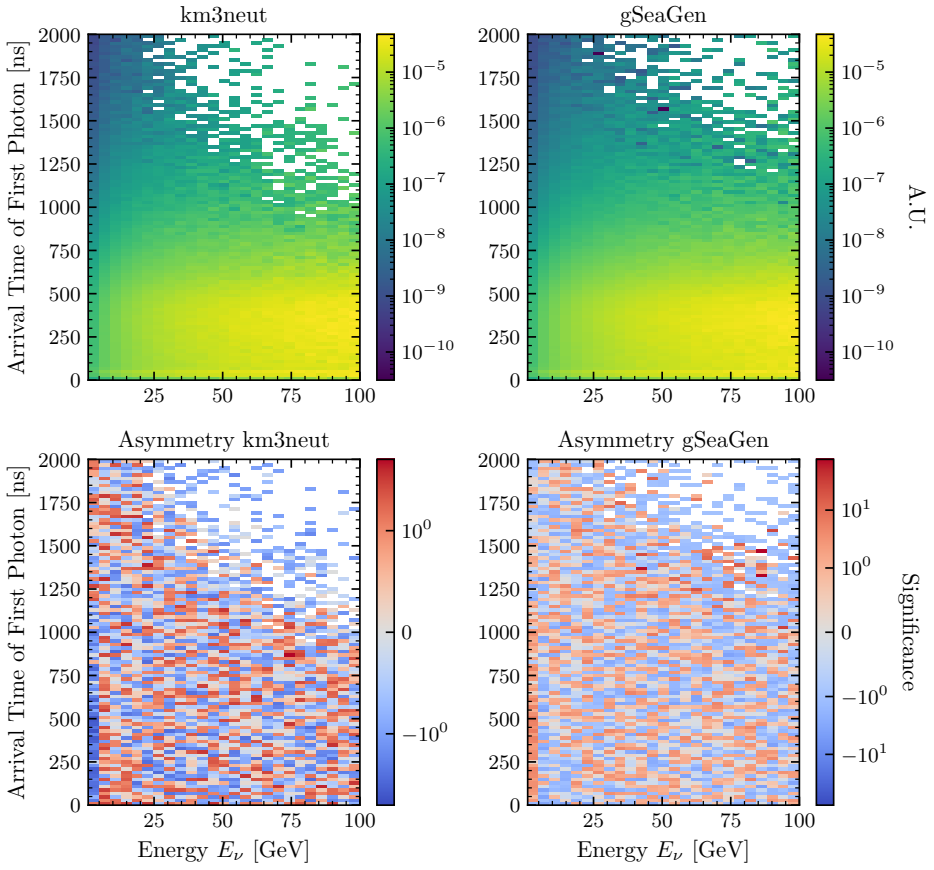

Figure 7.2.: Light-stage ν_e charged-current first-photon arrival time t_{first} versus E_ν, comparing `km3neut` and `gSeaGen` after reweighting. The definition of asymmetry follows section 5.5. Upper left: event density for `km3neut`. Upper right: event density for `gSeaGen`. Lower left: asymmetry relative to `km3neut`. Lower right: asymmetry relative to `gSeaGen`.

A consistent extension would be a bin-by-bin normalization in E_ν, thereby factorizing the spectral shape from the absolute rate within each neutrino-energy interval. This procedure would remove the energy-dependent normalization bias while retaining the differential shape information and remove potential differences in survival rates (section 8.4).

Additionally, this analysis is restricted to the main event population by imposing a cutoff at $t = 2000\,\text{ns}$, since the region beyond this threshold is statistically limited. Consequently, late photon arrivals are excluded from the definitions of t_{first} and t_{last}, and events with $\Delta t = t_{\text{last}} - t_{\text{first}} > 2000\,\text{ns}$ are discarded.

The phase space outside this interval does not affect the extracted normalization

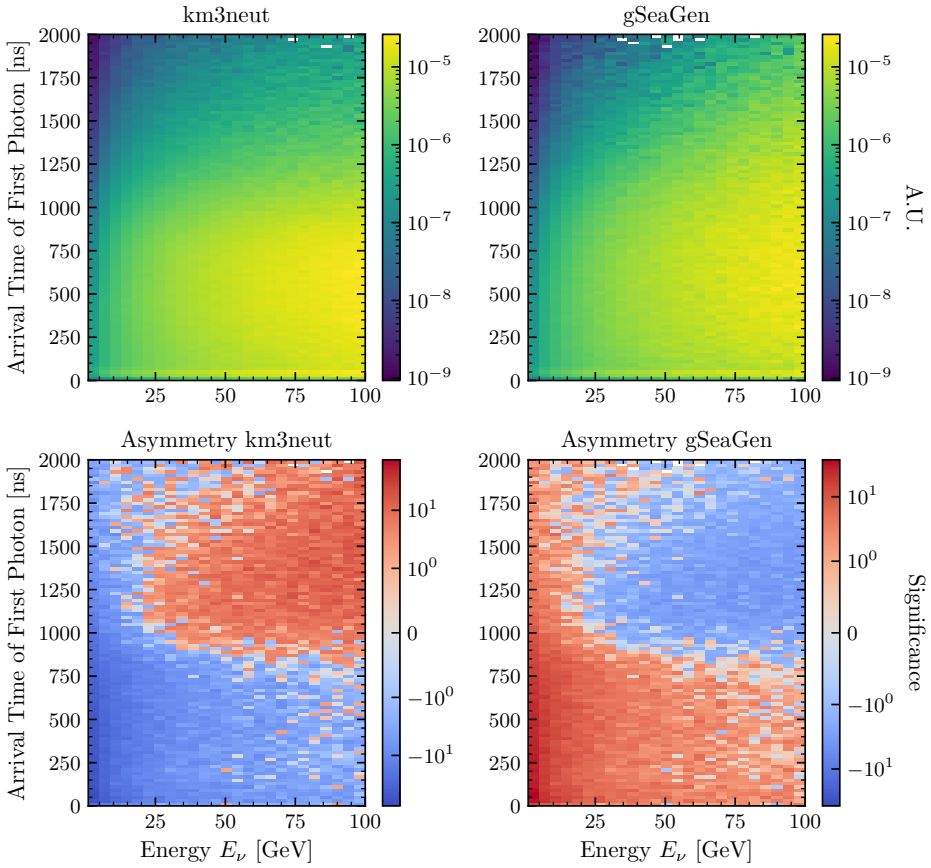

Figure 7.3.: Light-stage ν_μ charged-current first-photon arrival time t_{first} versus E_ν. The definition of asymmetry follows section 5.5. Upper left: event density for `km3neut`. Upper right: event density for `gSeaGen`. Lower left: asymmetry relative to `km3neut`. Lower right: asymmetry relative to `gSeaGen`.

within the considered window. Its inclusion requires increased statistics and should be addressed future work.

7.2. Timing Observables

The timing comparison is based on the joint distributions of each timing observable with neutrino energy, focusing on distinct regions. Early first photons t_{first}, early termination in t_{last}, and short timespans Δt at fixed E_ν.

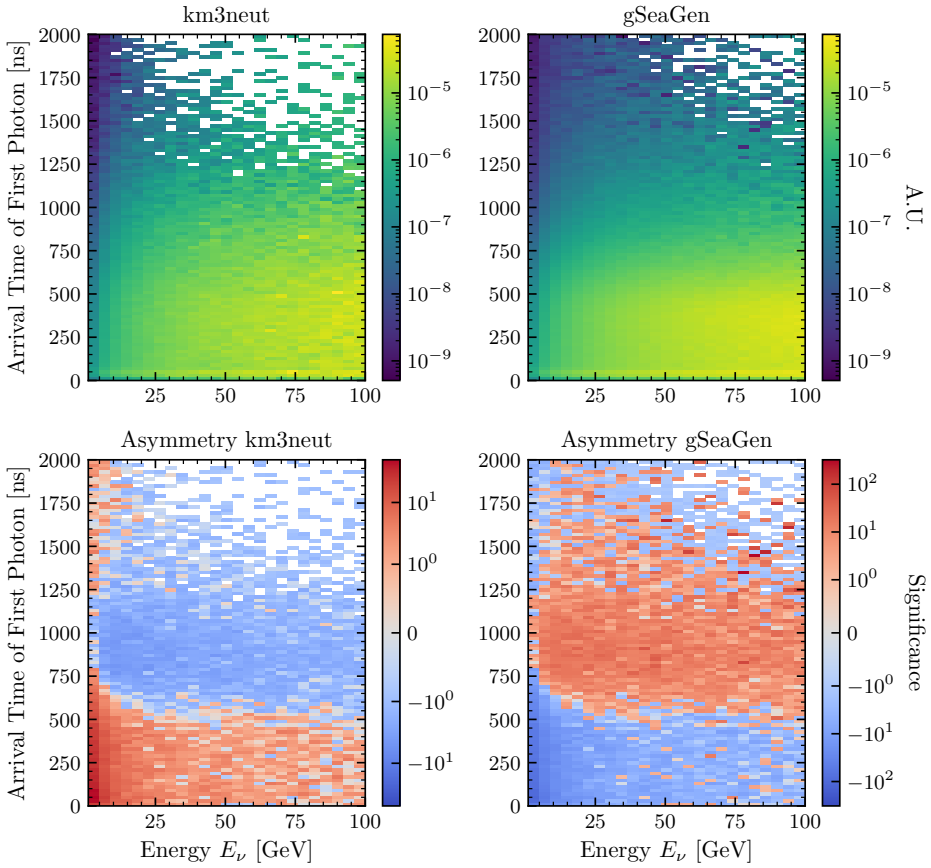

Figure 7.4.: Light-stage NC first-photon arrival time t_{first} versus E_ν. Upper left: event density for `km3neut`. Upper right: event density for `gSeaGen`. Lower left: asymmetry relative to `km3neut`. Lower right: asymmetry relative to `gSeaGen`.

7.2.1. First-photon arrival time

For ν_e and $\bar{\nu}_e$ charged-current interactions, the only structured deviation is confined to low neutrino energies and early photon arrival times and an earlier cutoff for higher energies of arrival times: `gSeaGen` predicts an excess of events with $t_{\text{first}} < 750\,\text{ns}$ and $E_\nu < 15\,\text{GeV}$ and `km3neut` predicts that for higher energies less late first photons arrive. The statistical significance in these regions is low and the impact is expected to be negligible.

Outside these phase-space regions, residual differences are consistent with statistical fluctuations, including the sparsely populated domain at high E_ν and large t_{first}, which remains statistically insignificant at the present sample size.

For ν_μ and $\bar{\nu}_\mu$ charged-current interactions, the first-photon distributions show a generator-dependent redistribution across $(E_\nu, t_{\text{first}})$: `gSeaGen` under populates low-energy events with early first photons, while `km3neut` under populates high-energy events with late first photons. The similarity of low-energy late-first-photon behaviour and high-energy early-first-photon behaviour between generators disfavours a global timing offset and instead points to differences in the secondary-particle content and/or kinematics. A plausible driver is different muon energies induced by different inelasticity (y) distributions and hadronic-state modelling. In the corresponding generator-stage comparisons, `km3neut` exhibits a modest shift toward fewer low-y events and more high-y events, together with increased charged-pion and kaon production but a relative deficit in additional muons; such changes can decrease the fraction of energetic muons and thereby reduce the population of events with late first photons. For NC interactions, `gSeaGen` overpopulates early first photons at low energy, whereas `km3neut` shows a deficit of mid-range first-photon times across energies. In the associated generator-stage trends, `km3neut` has fewer very low-$y \approx 0$ events by approximately a factor two, while simultaneously exhibiting reduced π^0 production but increased charged-pion production and substantially more $e^\pm$. These features are not mutually exclusive because timing is sensitive to secondary-particle energies and light-production topology, not only raw multiplicities. The observed pattern indicates that multiplicity-only diagnostics are insufficient for timing-level interpretation. For NC interactions, the same qualitative behaviour is present but the `km3neut` excess is reduced.

7.2.2. Last-photon arrival time

For $\bar{\nu}_e$ and ν_e charged-current interactions, the last-photon distributions mirror the corresponding first-photon observations: deviations are confined to low energies, where `km3neut` shows an excess in ν_e and `gSeaGen` shows a relative excess of early last photons for $E_\nu < 15\,\text{GeV}$ in $\bar{\nu}_e$ with higher significance compared to t_{first} but still expected to have a negligible impact. Beyond these localized regions, the

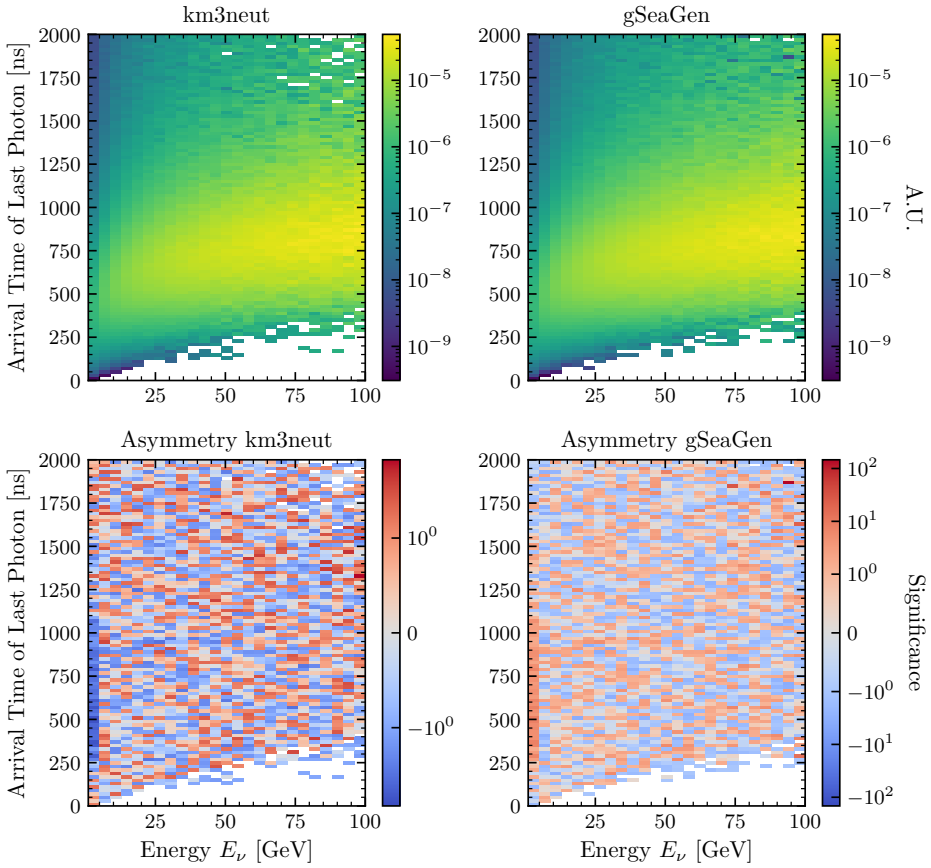

Figure 7.5.: Light-stage ν_e charged-current last-photon arrival time t_{last} versus E_ν. Upper left: event density for `km3neut`. Upper right: event density for `gSeaGen`. Lower left: asymmetry relative to `km3neut`. Lower right: asymmetry relative to `gSeaGen`.

differences are consistent with statistical noise.

For ν_μ and $\bar{\nu}_\mu$ CC interactions, the t_{last} distributions follow the same qualitative pattern as the first-photon observables, with a more pronounced effect at low energies. The `gSeaGen` deficit at low visible energy extends to larger t_{last}, while the phase space region in which `gSeaGen` exceeds `km3neut` is reduced relative to the first-photon case.

At high energies, `km3neut` exhibits an earlier cutoff in t_{last}, i.e. last photons arrive earlier, indicating suppressed late-light production compared to `gSeaGen`. Equivalently, with increasing energy, the region depleted in early t_{last} shrinks more strongly in `gSeaGen` than in `km3neut`, consistent with a more extended late-light component

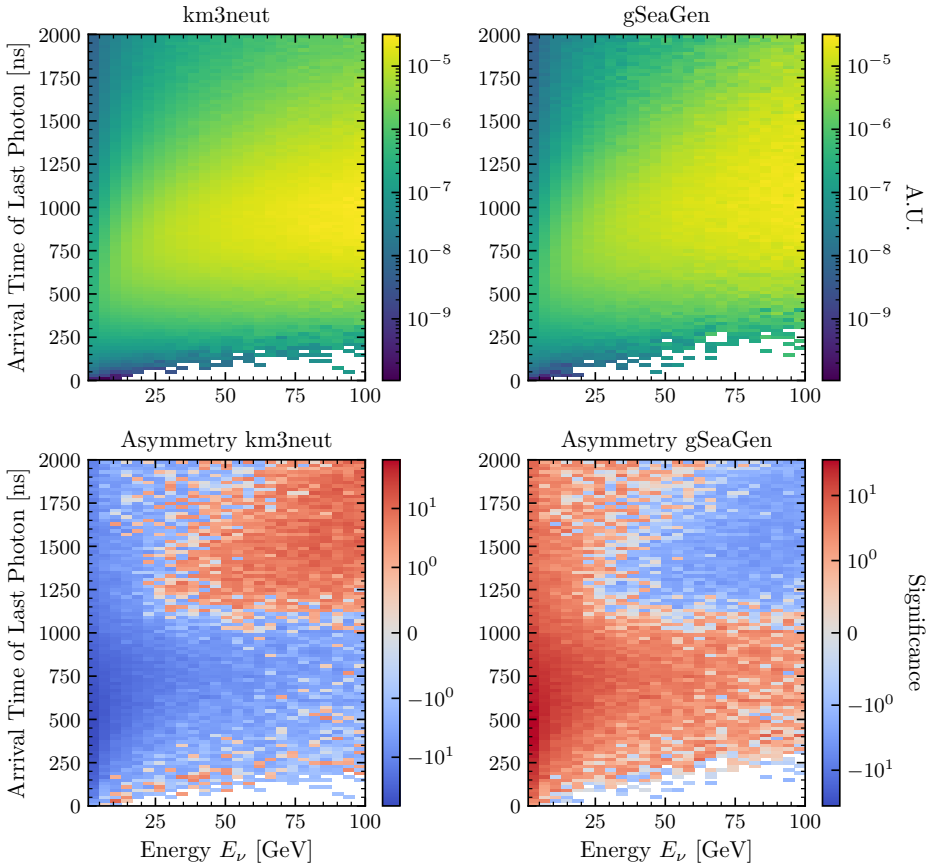

Figure 7.6.: Light-stage ν_μ charged-current last-photon arrival time t_{last} versus E_ν. Upper left: event density for `km3neut`. Upper right: event density for `gSeaGen`. Lower left: asymmetry relative to `km3neut`. Lower right: asymmetry relative to `gSeaGen`.

in `gSeaGen`. This behavior is compatible with lower average inelasticity in ν_μ and $\bar{\nu}_\mu$ interactions, yielding fewer high-energy $\mu^\pm$ that propagate over long distances and generate additional delayed light through stochastic energy losses.

For NC channels, the generator ordering is similar to the first-photon case, but the phase-space regions where `km3neut` dominates are reduced and often compatible with statistical fluctuations.

7.2.3. Event timespan

For ν_e and $\bar{\nu}_e$, the timespan shows no prominent structure; a mild `gSeaGen` excess appears at low energy and short events, but it is small. The timespan follows

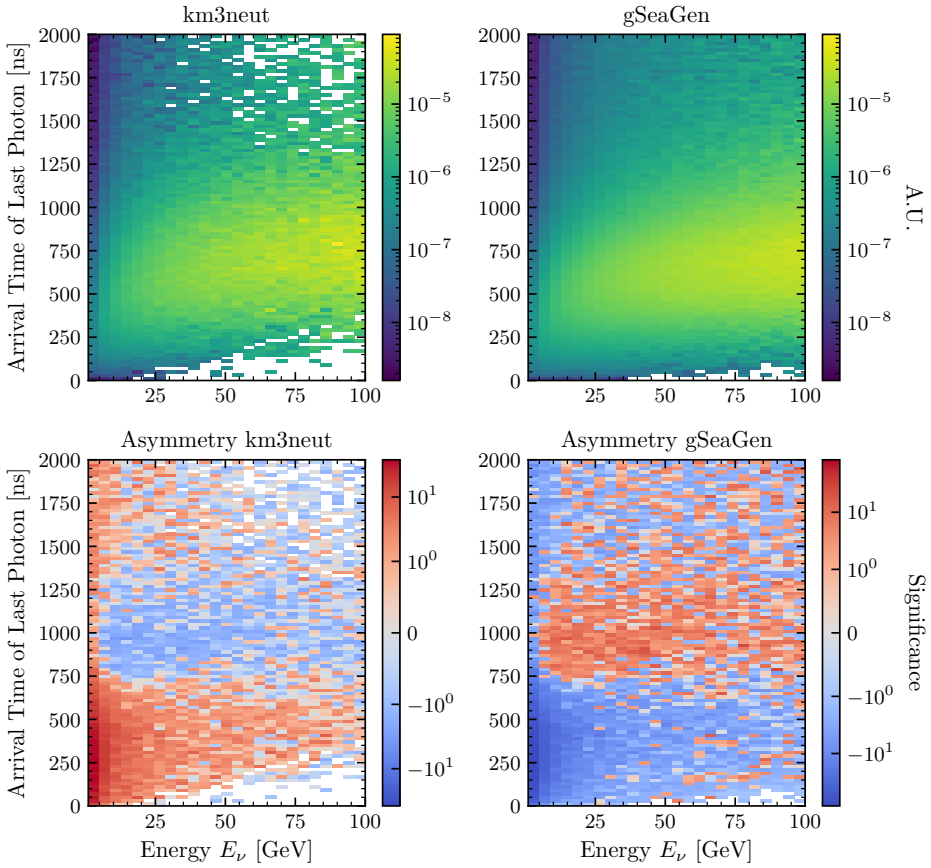

Figure 7.7.: Light-stage NC last-photon arrival time t_{last} versus E_ν. Upper left: event density for `km3neut`. Upper right: event density for `gSeaGen`. Lower left: asymmetry relative to `km3neut`. Lower right: asymmetry relative to `gSeaGen`.

the same qualitative behaviour as the first- and last-photon observables, with a low-energy `km3neut` excess and no stable high-statistics discrepancies.

For ν_μ charged-current interactions, `km3neut` dominates short-duration, low-energy events and shows a relative deficit of short-duration events at high energy, consistent with reduced secondary-muon production and reduced muon energies in parts of phase space. A direct test would be a two-dimensional comparison including the energy of the leading lepton in the light-stage sample.

For NC interactions, `km3neut` under populates short, low-energy events, consistent with the low-energy deficits observed in the timing endpoints.

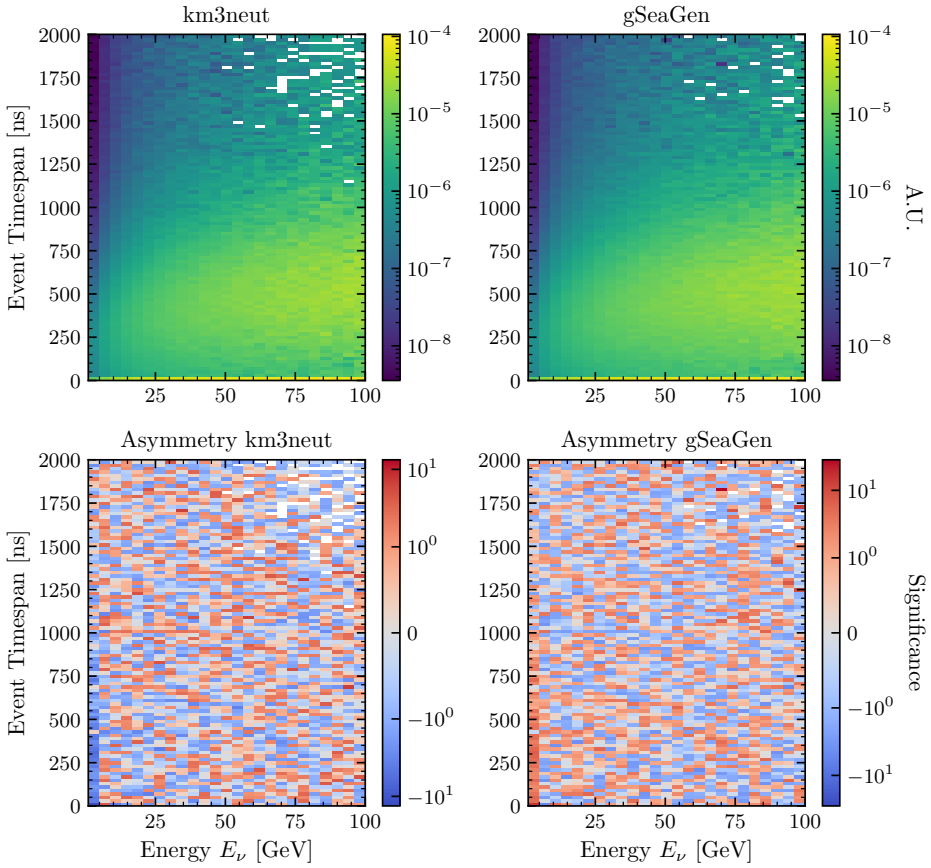

Figure 7.8.: Light-stage ν_e charged-current event timespan $\Delta t = t_{\text{last}} - t_{\text{first}}$ as a function of neutrino energy E_ν. Upper left: event density for `km3neut`. Upper right: event density for `gSeaGen`. Lower left: asymmetry relative to `km3neut`. Lower right: asymmetry relative to `gSeaGen`.

7.3. Optical Yield

The event amplitude N_γ is defined as the total number of photon arrivals at the photocathode surfaces, counting each photon individually, including multiple arrivals on the same PMT at distinct times. It is computed from the true photon arrival times and does not incorporate effects of PMT quantum efficiency, collection efficiency, or trigger response. The mean amplitude $\langle N_\gamma \rangle$ is defined as the mean total number of photon arrivals at the photocathode and follows weighted profiles defined in section 5.6

The mean number of hit PMTs is defined as the mean number of PMTs registering at least one photon arrival. This quantity is likewise evaluated at the photocathode

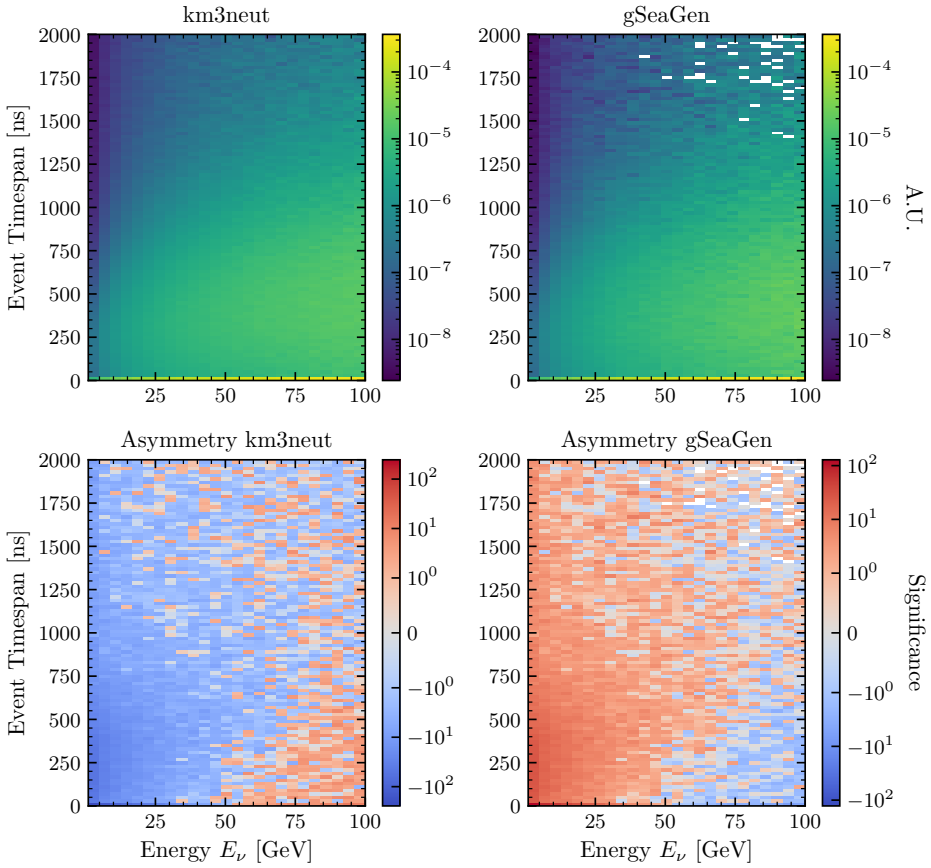

Figure 7.9.: Light-stage ν_μ charged-current event timespan Δt versus E_ν. Upper left: event density for `km3neut`. Upper right: event density for `gSeaGen`. Lower left: asymmetry relative to `km3neut`. Lower right: asymmetry relative to `gSeaGen`.

level without applying quantum-efficiency, collection-efficiency, or trigger corrections, and follows the weighted profile definition introduced in section 5.6.

The mean number of hit PMTs (Figure 7.11) for combined neutrino and antineutrino samples is systematically larger in `km3neut` than in `gSeaGen` for ν_μ CC interactions. For ν_μ, the excess increases with E_ν and becomes pronounced for $E_\nu \gtrsim 40\,\mathrm{GeV}$, consistent with the timing-level observation of more compact light emission at low energies and a modified high-energy tail in `km3neut`. NC interactions, ν_τ and ν_e are compatible within statistical uncertainty. The same trend is observed for the mean amplitude $\langle N_\gamma \rangle$ which is therefore not shown.

The amplitude N_γ dependent on energy is compatible with statistical fluctuations

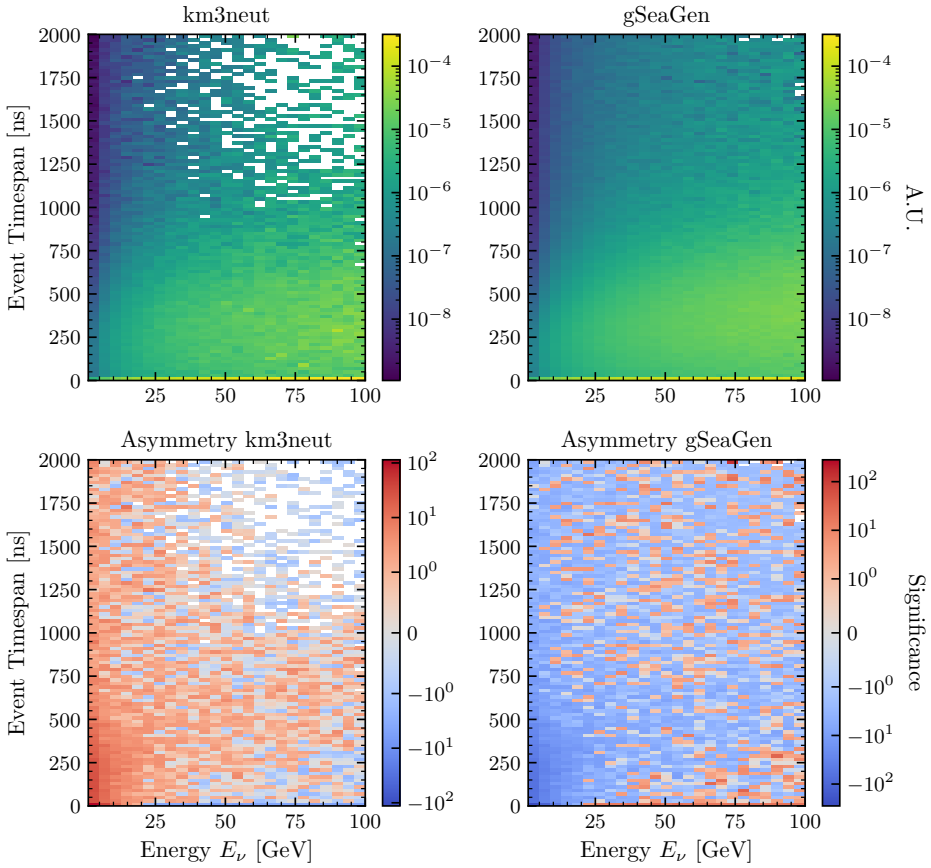

Figure 7.10.: Light-stage NC event timespan Δt versus E_ν. Upper left: event density for `km3neut`. Upper right: event density for `gSeaGen`. Lower left: asymmetry relative to `km3neut`. Lower right: asymmetry relative to `gSeaGen`.

for $\nu_e + \bar{\nu}_e$ and for NC interactions. In contrast, for $\nu_\mu + \bar{\nu}_\mu$ shown in Figure 7.12, a significant excess at low amplitudes is observed in `km3neut` over the full energy range.

For $\nu_\mu + \bar{\nu}_\mu$, the amplitude asymmetries are in tension with $\langle N_\gamma \rangle$ and $\langle N_{\text{hit}} \rangle$. A bin-wise normalization in E_ν is therefore required to remove global normalization effects at high energies and to enable a differential comparison.

The enhanced $\langle N_{\text{hit}} \rangle$ and $\langle N_\gamma \rangle$ in `km3neut` indicate more spatially extended light distributions for $\nu_\mu + \bar{\nu}_\mu$. This is consistent with reduced inelasticity, transferring a larger fraction of E_ν to the hadronic system and increasing local energy deposition and light yield. The outgoing muons carry correspondingly less energy, with ranges

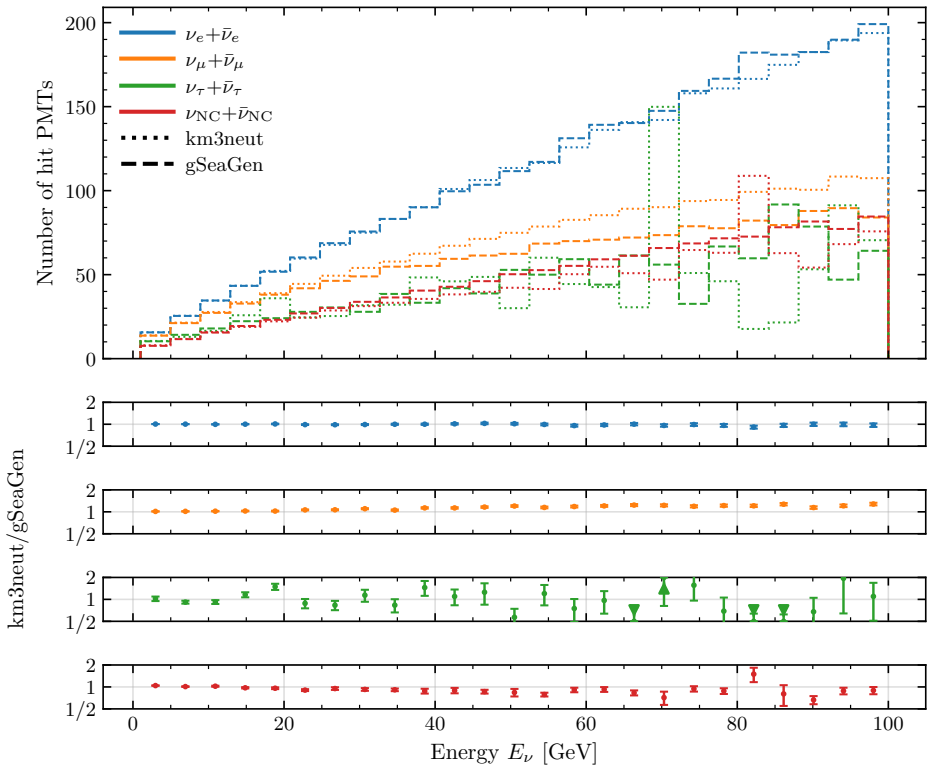

Figure 7.11.: Number of hit PMTs as a function of neutrino energy. Upper left: event density for `km3neut`. Upper right: event density for `gSeaGen`. Lower left: asymmetry relative to `km3neut`. Lower right: asymmetry relative to `gSeaGen`.

of $\mathcal{O}(\mathrm{m/GeV})$, depositing energy over shorter path lengths and partially via decay electrons within the instrumented volume.

At the differential level (photon yield vs. E_ν), ν_e remains dominated by fluctuations, while $\bar{\nu}_e$ shows a localized `km3neut` deficit in the phase space of low E_ν and low photon counts. For ν_μ and $\bar{\nu}_\mu$, `km3neut` dominates the region of low energy and low photon multiplicity; the corresponding region is larger and more significant for antineutrinos. For NC interactions, the ordering reverses in that specific corner of phase space: `gSeaGen` dominates low energy and low photon multiplicity, but the effect does not extrapolate to a large difference in mean yield.

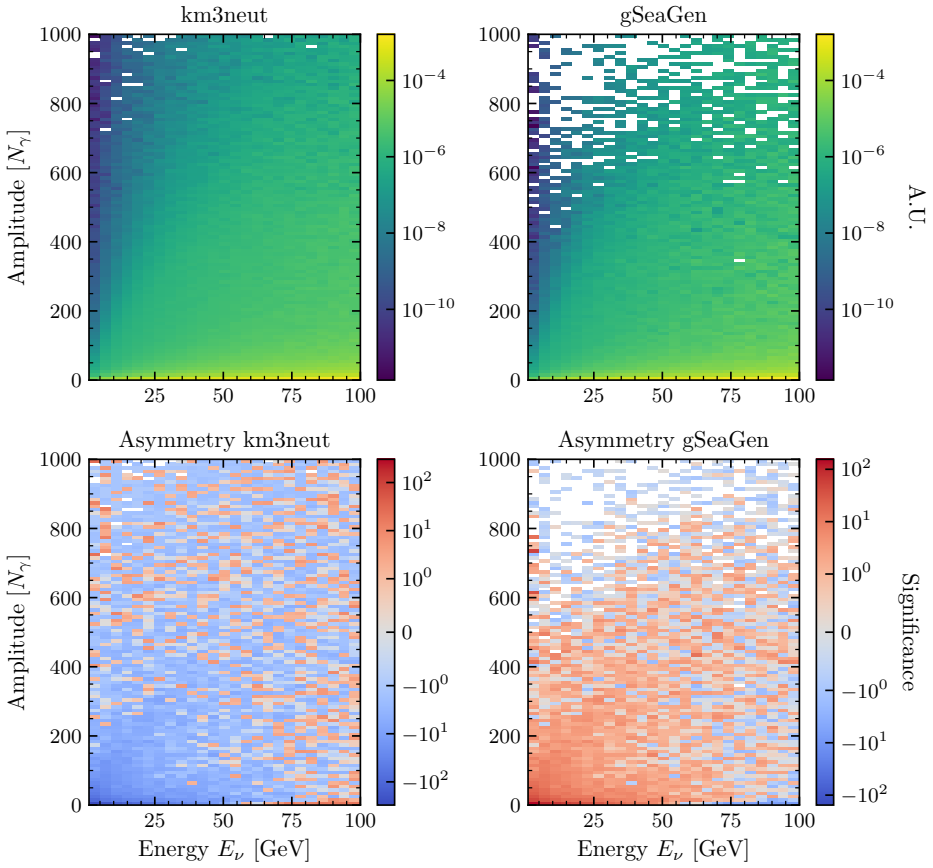

Figure 7.12.: Light-stage ν_μ charged-current optical yield: photon multiplicity versus E_ν. Upper left: event density for `km3neut`. Upper right: event density for `gSeaGen`. Lower left: asymmetry relative to `km3neut`. Lower right: asymmetry relative to `gSeaGen`.

7.4. Photon-Origin Decomposition

To relate detector-level light yield to the simulated final state, the detected photons are decomposed by the particle species that produced them and follows the definition in section 5.6.

For ν_e CC interactions (Figure 7.13), the photon yield attributed to $\pi^\pm$ is consistently less for `km3neut` compared to `gSeaGen`, in contrast to the generator-level agreement. In contrast, the π^0-tagged photon contribution is larger in `km3neut` despite lower yield at generator-level π^0 multiplicity. This points to generator-dependent differences in secondary energy/angle spectra (and hence $\pi^0 \to \gamma\gamma$ kinematics and subsequent electromagnetic shower development) and should be quantified explicitly

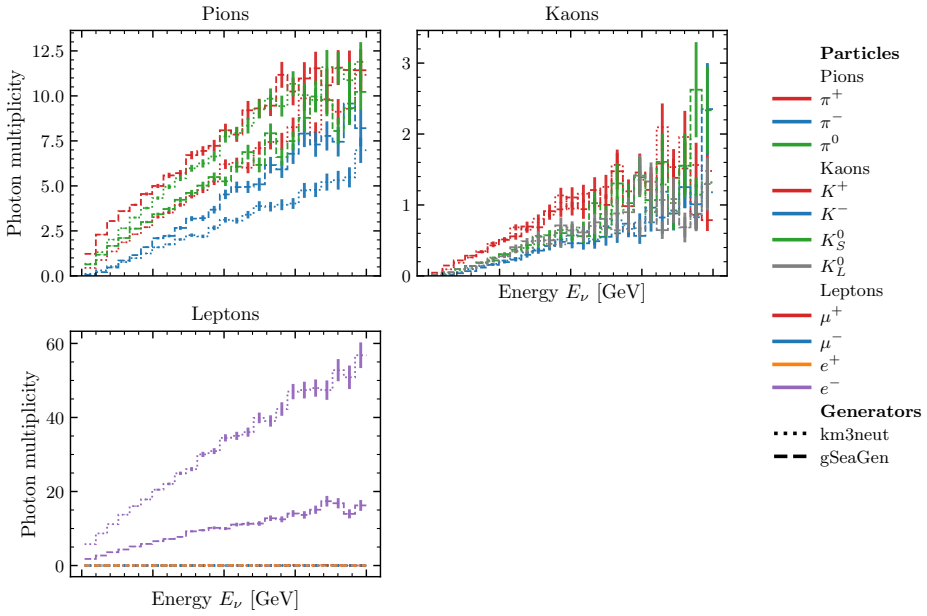

Figure 7.13.: Light-level secondary-particle multiplicities for ν_e charged-current interactions as a function of neutrino energy.

in future work. For π^+, `gSeaGen` predicts a moderately photon yield up to a factor of 1.3. Kaon-induced photons are statistics-limited; fluctuations are consistent despite slightly larger K^+-tagged contribution in `gSeaGen` at generator level, indicating a harder K^+ spectrum resulting in a higher photon yield. Electron-induced photons are significantly larger in `km3neut` (up to $\sim 3\times$), despite only moderate differences in the Bjorken-y distribution and an the absolute electron multiplicity at the per-mille level.

For $\bar{\nu}_e$, as shown in Figure 7.14, `gSeaGen` shows higher π-induced photon contributions. Kaon-induced contributions are again noise-dominated. Electron-induced photon contributions remain larger in `km3neut` by a factor ~ 3.

For ν_μ, as shown in Figure 7.15, charged-current interactions, detector-level photon contributions from π^0 are larger in `km3neut` at high energy up to a factor ~ 2 for $E_\nu \gtrsim 50\,\mathrm{GeV}$. For π^+, `gSeaGen` dominates up to $\sim 50\,\mathrm{GeV}$, after which `km3neut` becomes slightly larger within compatibility; notably, the `gSeaGen` pion-induced hit contributions decrease in the high-energy region where `km3neut` increases. For π^-, `gSeaGen` exceeds `km3neut` mildly but within uncertainness. Muon-induced photon

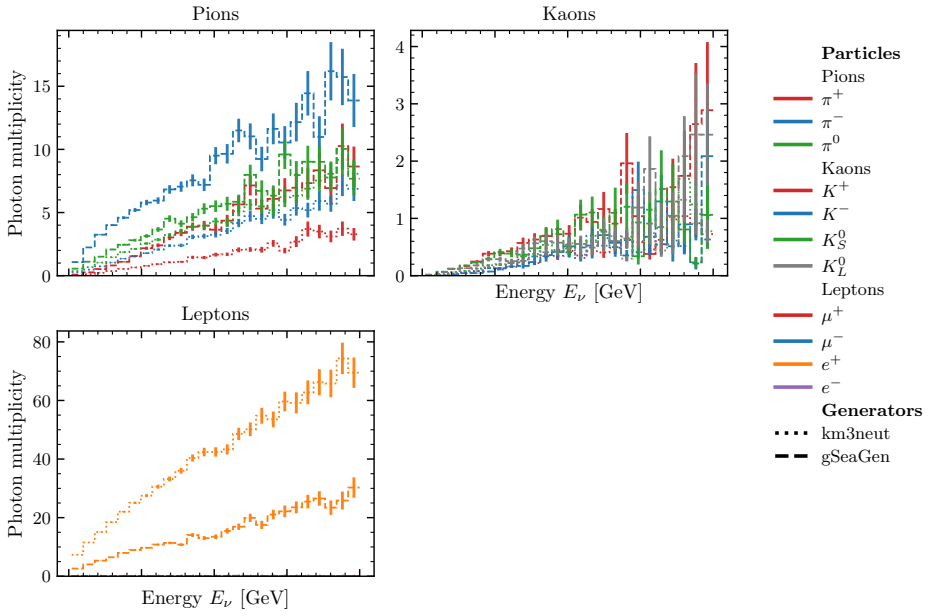

Figure 7.14.: Light-level secondary-particle multiplicities for $\bar{\nu}_e$ charged-current interactions as a function of neutrino energy.

contributions are substantially larger in `km3neut` up to a factor ~ 3, and muons dominate the total, implying that differences in muon production and/or muon energy-loss patterns are a primary driver of the light-yield discrepancy. This is consistent with the observation that generator-level π^0 multiplicities can be similar while detector-level pion-induced photon arrivals differ, again pointing to secondary kinematics as a controlling variable.

For $\bar{\nu}_\mu$, as shown in Figure 7.16, charged-current interactions, `gSeaGen` dominates π-induced contributions but shows reduced pion-induced photon arrivals from the other charge states at higher energies, despite producing more pions at event level in parts of phase space. Kaon-induced contributions remain unresolved. Muon-induced photon contributions are larger in `km3neut` by factors $\sim 3-4$ and dominate the total. For NC interactions (Figure 7.17 for ν_{NC} and Figure 7.18 for $\bar{\nu}_{\mathrm{NC}}$), lepton-induced contributions are negligible and remain noise-dominated due to low lepton multiplicity. `km3neut` shows substantially higher pion-induced photon contributions (typical factors $\sim$ 2–3) and similarly higher kaon-induced contributions within large uncertainties. However, the kaon-induced hit counts remain small $\mathcal{O}(1)$–$\mathcal{O}(3)$

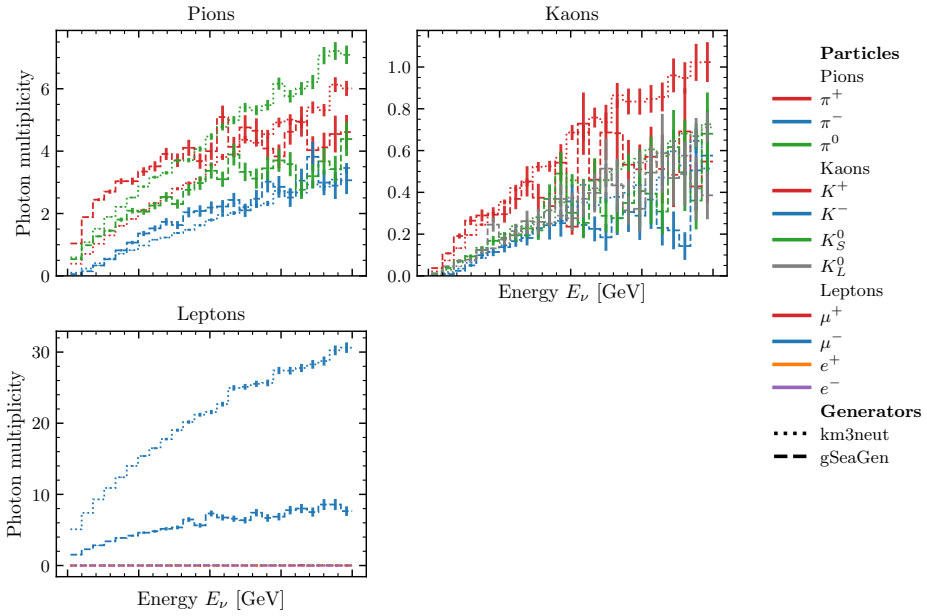

Figure 7.15.: Light-level secondary-particle multiplicities for ν_μ charged-current interactions as a function of neutrino energy.

photon arrivals on average, implying negligible impact on total light. A notable inconsistency arises when comparing generator-level multiplicities to detector-level photon origins: `gSeaGen` can produce slightly more π^0 and π^- at generator level while `km3neut` produces more photon photon arrivals attributed to these species. This demonstrates that raw multiplicities do not predict optical yield without incorporating the energy spectra of the secondaries and their spatial development.

7.5. Synthesis and Implications

The light-stage comparison identifies the most pronounced and phase-space coherent generator discrepancies in $\nu_\mu/\bar{\nu}_\mu$ CC interactions. Over a broad neutrino-energy range, `km3neut` systematically predicts higher detected-photon yields than `gSeaGen`, accompanied by shorter event timespans and an earlier saturation of the last detected photon time t_{last} at high E_ν. The correlated modification of yield and timing excludes a trivial global timing offset and instead points to differences in light-production topology. Decomposition by photon origin demonstrates that the

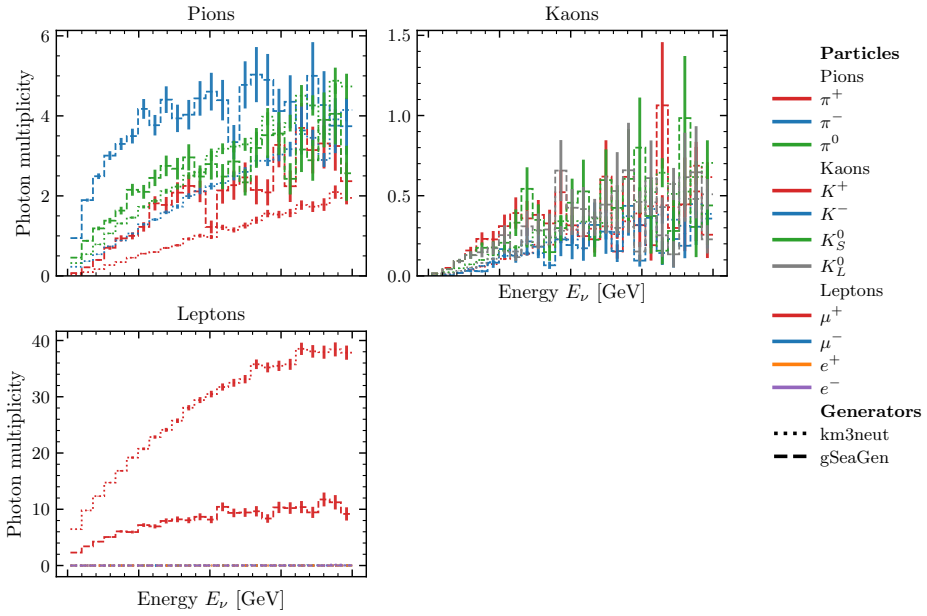

Figure 7.16.: Light-level secondary-particle multiplicities for $\bar{\nu}_\mu$ charged-current interactions as a function of neutrino energy.

excess light in `km3neut` is dominated by muon-induced emission, with subleading and energy-dependent contributions from pion-induced photons. These effects therefore primarily trace back to generator-dependent treatments of muon kinematics, presumably driven by differences in inelasticity distributions and hadronic final-state composition that alter the relative energy carried by the muon and the structure of the accompanying hadronic system.

For $\nu_e/\bar{\nu}_e$ CC interactions, generator differences are more localized in phase space. Deviations in timing observables and differential photon yield are confined to the low-energy region and do not form extended structures in (E_ν, t) space, while at higher energies the timing distributions are statistically compatible between generators. Despite this, the mean detected-photon yield shows a persistent excess in `km3neut` for ν_e interactions across the full energy range, indicating that the integrated optical response remains sensitive to generator-dependent electromagnetic and hadronic energy deposition even when timing metrics agree. The photon-origin supports this interpretation by revealing enhanced electron-induced contributions at detector level in `km3neut`, consistent with differences in secondary energy spectra and shower

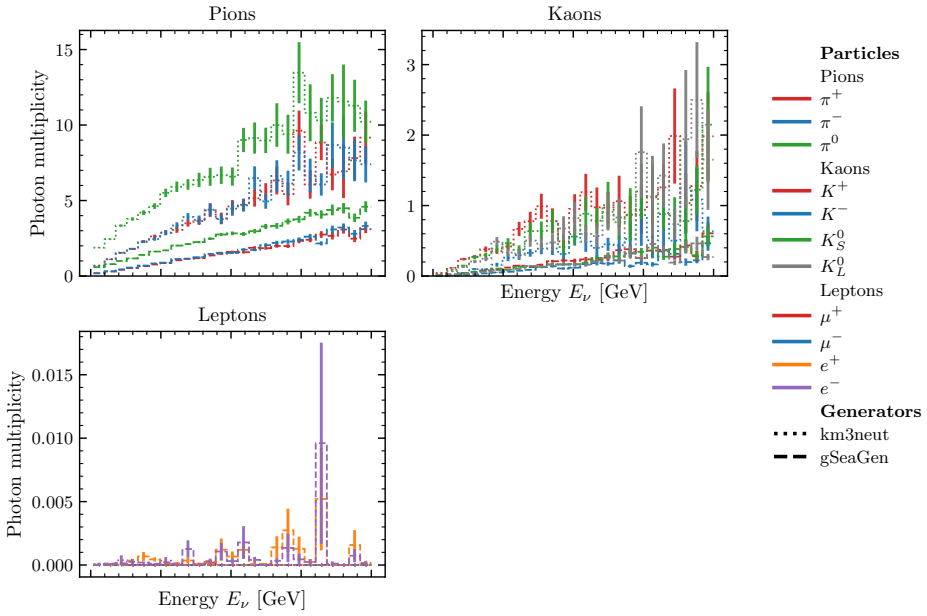

Figure 7.17.: Light-level secondary-particle multiplicities for NC interactions induced by neutrinos as a function of neutrino energy.

development rather than purely in timing structure.

Neutral-current interactions exhibit a qualitatively different pattern. Although `km3neut` produces substantially larger pion-induced photon contributions-often exceeding those of `gSeaGen` by factors of two, the mean detected-photon yield is broadly consistent between generators. Instead, the low-energy, low-photon-multiplicity region is preferentially populated by `gSeaGen`. This behaviour indicates that generator-level secondary multiplicities are not reliable predictors of the detector-level optical response. Instead, the detected light is governed primarily by the energy spectra, spatial development, and light-production efficiency of the secondary particles, rather than by their raw multiplicities.

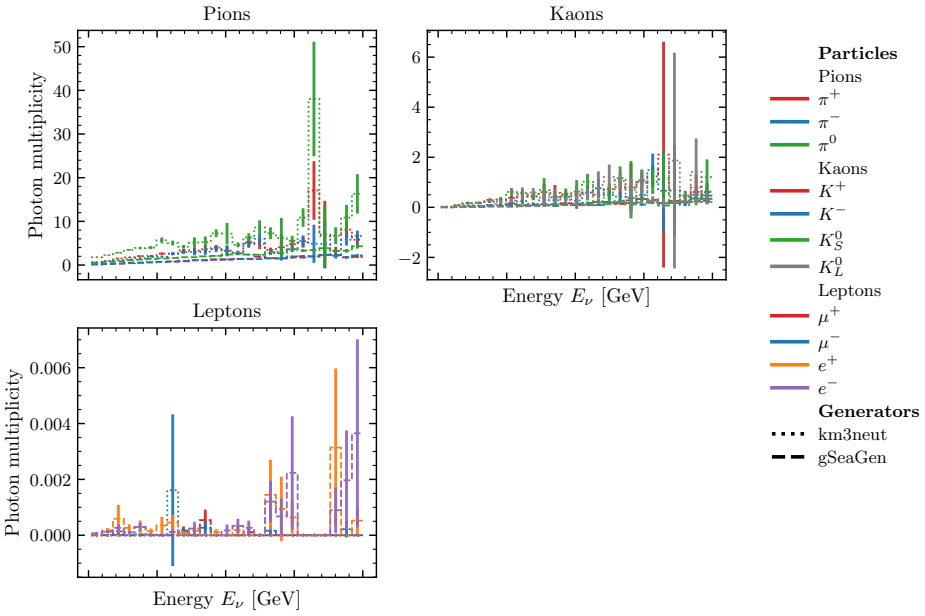

Figure 7.18.: Light-level secondary-particle multiplicities for NC interactions induced by antineutrinos as a function of neutrino energy.

8. Reconstruction-Level Comparisons

This chapter compares the reconstruction performance obtained with `km3neut` and `gSeaGen` under ORCA's detector conditions.

All events are weighted according to Equation 4.3. The angular error is defined as the opening angle between the true and reconstructed neutrino directions. Perfect flavour identification is assumed throughout: ν_μ CC interactions are reconstructed using an algorithm optimized for the reconstruction of track-like events, and ν_e CC interactions as well as NC interactions using an algorithm optimized for the reconstruction of shower-like events.

The reconstructed samples exhibit substantial channel-dependent differences in event counts between the generators. The dominant contribution arises from the unequal number of processed runs, with additional effects from stage-dependent selection efficiencies discussed in section 8.4. The number of processed runs and surviving events at each stage are summarized in Table 8.1. Owing to limited statistics, the $\nu_\tau + \bar{\nu}_\tau$ and NC samples are excluded from quantitative generator-to-generator comparisons in most of the following analyses. The results presented in this chapter

	km3neut			gSeaGen		
Channel	Generator	Light	Reco	Generator	Light	Reco
ν_e	32 887 678	6 268 320	172 280	29 262 286	8 707 625	189 810
$\bar{\nu}_e$	8 982 415	1 887 529	71 006	9 174 711	2 940 343	76 553
ν_μ	101 175 145	7 468 310	294 330	29 503 703	1 193 171	45 070
$\bar{\nu}_\mu$	32 976 026	2 726 315	132 100	13 390 036	587 758	24 079
ν_τ	57 176	6 118	294	1 232 862	50 464	1 455
$\bar{\nu}_\tau$	32 980	3 361	155	980 264	39 911	1 093
ν_{NC}	3 249 995	296 221	7 853	31 215 293	4 245 232	72 728
$\bar{\nu}_{\mathrm{NC}}$	856 383	66 991	1 654	13 546 524	1 451 298	20 673
Runs	1 503	740	672	1 392	1 381	1 150

Table 8.1.: Event counts by interaction channel, generator, light and reconstruction stage as well as the number of processed runs is shown

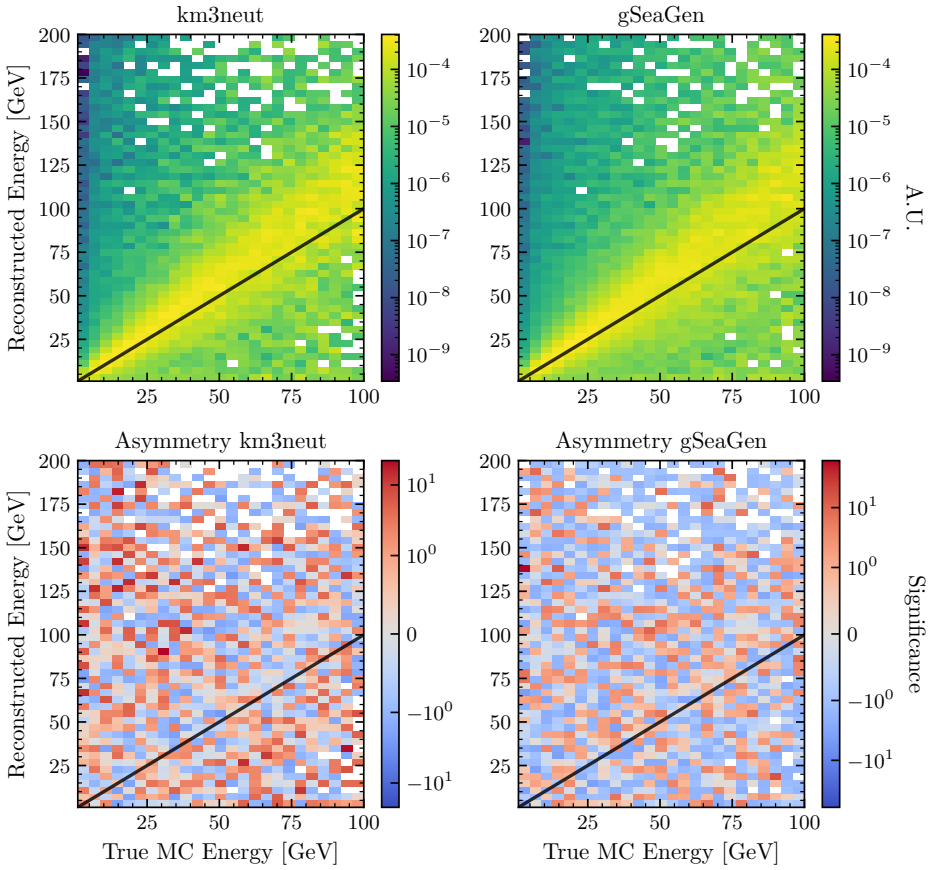

Figure 8.1.: True versus reconstructed energy for $\nu_e + \bar{\nu}_e$. The diagonal indicates perfect reconstruction. The definition of asymmetry follows section 5.5. Upper left: event density for `km3neut`. Upper right: event density for `gSeaGen`. Lower left: asymmetry relative to `km3neut`. Lower right: asymmetry relative to `gSeaGen`.

should therefore be regarded as indicative rather then definitive.

8.1. Energy Reconstruction

Figures Figure 8.1 and Figure 8.2 show the true neutrino energy as a function of reconstructed energy for the combined $\nu_e + \bar{\nu}_e$ and $\nu_\mu + \bar{\nu}_\mu$ samples, respectively. The diagonal corresponds to perfect energy reconstruction.

For $\nu_e + \bar{\nu}_e$, both generators show a clear concentration of events along the identity line, indicating good overall energy reconstruction. Differences are nonetheless visible: `km3neut` exhibits a mild tendency to overestimate the reconstructed energy,

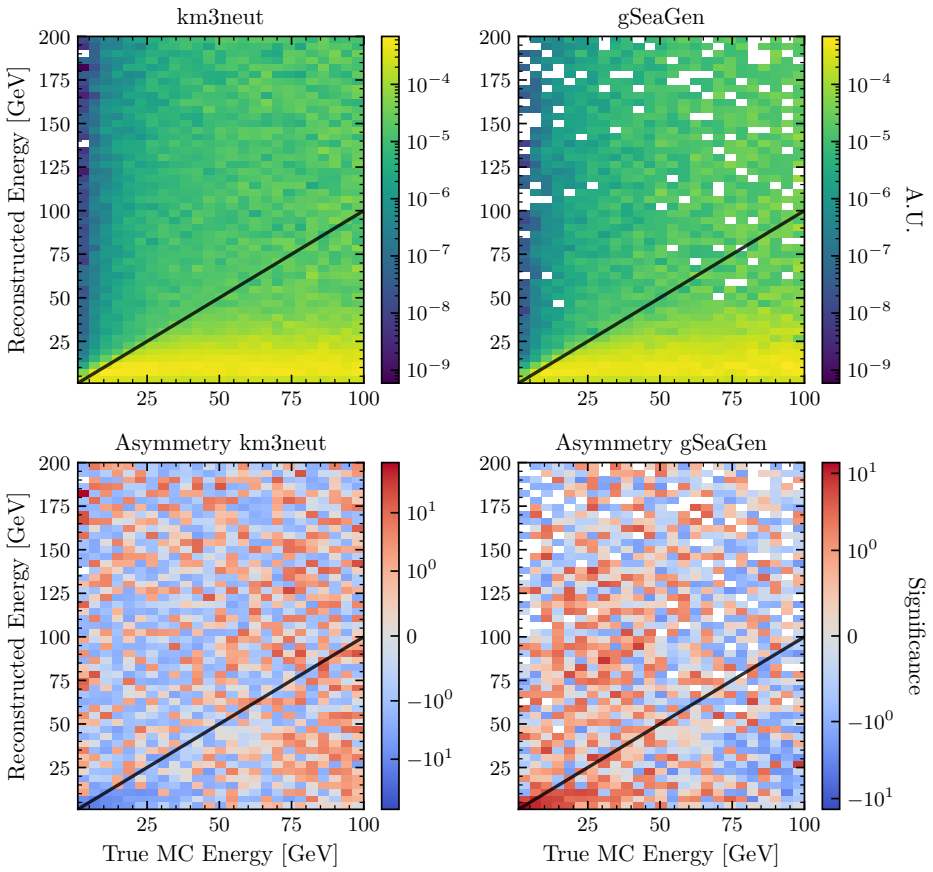

Figure 8.2.: True versus reconstructed energy for $\nu_\mu + \bar{\nu}_\mu$. The diagonal indicates perfect reconstruction. Upper left: event density for `km3neut`. Upper right: event density for `gSeaGen`. Lower left: asymmetry relative to `km3neut`. Lower right: asymmetry relative to `gSeaGen`.

while `gSeaGen` shows a small underestimation. However, the observed differences are compatible with statistical fluctuations.

The discrepancy is more pronounced for $\nu_\mu + \bar{\nu}_\mu$. For a given true energy, `km3neut` systematically yields lower reconstructed energies than `gSeaGen`, corresponding to a downward shift relative to the diagonal. This effect directly modifies the reconstructed distribution used in atmospheric oscillation analyses.

A systematic bias in E_{reco} modifies the reconstructed L/E and displaces the positions of oscillation extrema. For $\nu_e + \bar{\nu}_e$, the impact is negligible. For $\nu_\mu + \bar{\nu}_\mu$, the stronger energy underestimation in `km3neut` increases the effective L/E, shifting the disappearance minimum to lower reconstructed energies and distorting the inferred

oscillation frequency. Such migration effects also alter the reconstructed event distributions near the disappearance minimum and propagate to the ν_e appearance channel, where they modify the energy-dependent matter-enhanced pattern and consequently affect the sensitivity to the mass ordering.

These observations indicate that generator choice induces a correlated, energy-dependent shape systematic in reconstructed energy. This effect cannot be absorbed by simple normalization or flux scaling and must be treated as a response-function uncertainty to avoid biasing oscillation parameters. In combined ν_e-ν_μ fits, inconsistent generator-induced biases can lead to internal tensions that degrade sensitivity.

8.2. Angular Reconstruction

Figure 8.3 shows the overall angular error for $\nu_e + \bar{\nu}_e, \nu_\mu + \bar{\nu}_\mu$ and $\nu_{\mathrm{NC}} + \bar{\nu}_{\mathrm{NC}}$ and Figure 8.4 and Figure 8.5 show the angular reconstruction error as a function of true neutrino energy for the combined sample and for $\nu_e + \bar{\nu}_e$ and $\nu_\mu + \bar{\nu}_\mu$ separately .

For the combined sample, both generators show a concentration of events at small angular errors with a gradual improvement toward higher energies. The overall distributions and asymmetry maps are broadly consistent, indicating comparable angular performance.

In the $\nu_e + \bar{\nu}_e$ channel, no statistically significant generator-dependent differences are observed. Both generators exhibit similar angular resolutions and energy dependence, with most events reconstructed within $\mathcal{O}(0.5)$ rad and deviation compatible within statistical uncertainties. For $\nu_\mu + \bar{\nu}_\mu$, the angular resolution improves with increasing energy for both generators, consistent with the longer muon track length at higher energies. At low energies, however, `km3neut` exhibits a systematically larger angular uncertainty. Restricting the true Bjorken inelasticity to $y \in (0, 0.2)$, thereby selecting events in which the muon carries the dominant fraction of the neutrino energy, shown in Figure 8.6, removes this discrepancy. This demonstrates that differences in the y-distribution are potentially the primary driver of the observed angular-resolution differences.

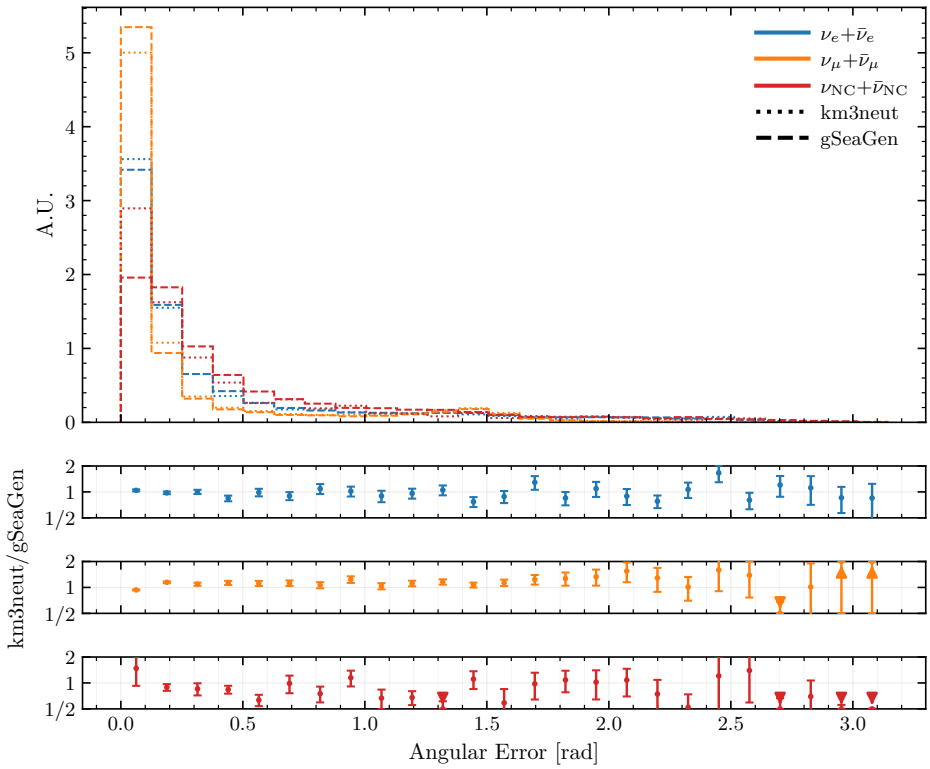

Figure 8.3.: Angular reconstruction error for the combined sample for $\nu_e+\bar{\nu}_e$, $\nu_\mu+\bar{\nu}_\mu$ and $\nu_{\mathrm{NC}}+\bar{\nu}_{\mathrm{NC}}$.

8.3. Bjorken-y of Reconstructed Events

This section examines how reconstruction reshapes the inelasticity (y) distributions discussed at generator level in chapter 6. Figure Figure 8.7 shows the Bjorken-y distribution of successfully reconstructed events compared to the original generator distribution.

Relative to the generator-level distributions, reconstruction induces a suppression of high-y events. While the true distributions extend up to $y \simeq 1$, the reconstructed samples are increasingly depleted for $y \gtrsim 0.5$. This reflects the loss of events in which a large fraction of the neutrino energy is transferred to the hadronic system, leaving insufficient energy in the outgoing lepton for reliable reconstruction. At low y ($y \lesssim 0.2$), the reconstructed distributions closely follow the generator-level shapes, indicating a high and approximately uniform reconstruction efficiency.

The `km3neut/gSeaGen` ratios display a stronger y dependence after reconstruction

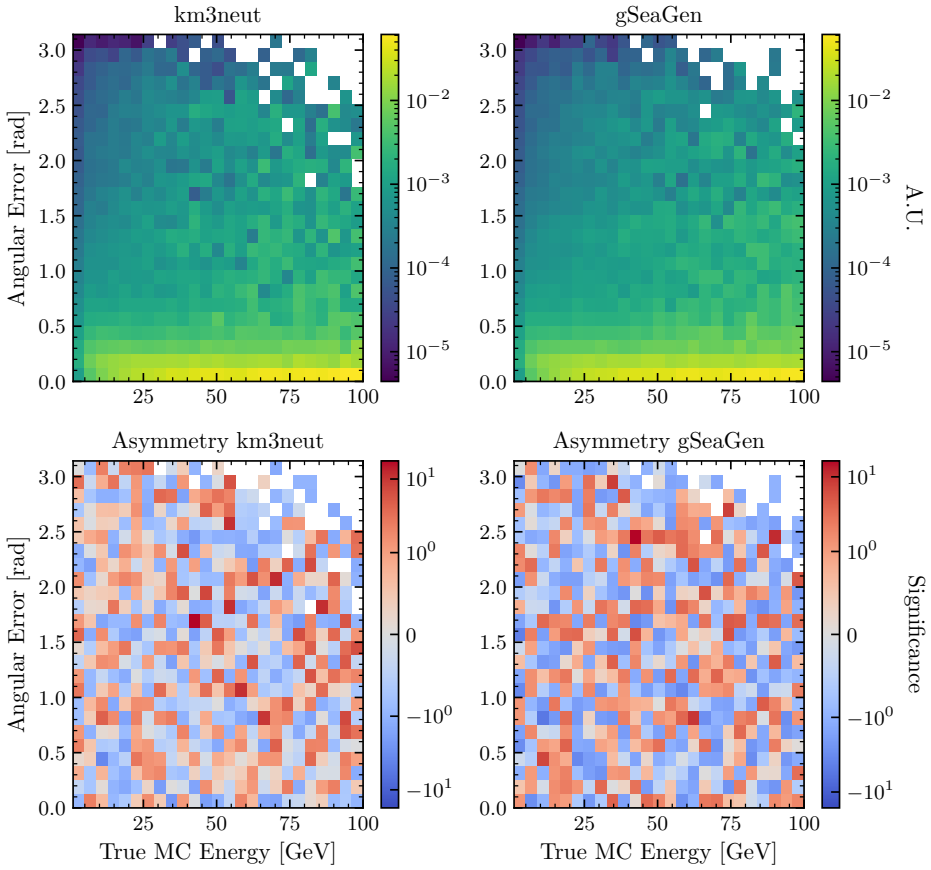

Figure 8.4.: Angular reconstruction error versus true energy for $\nu_e + \bar{\nu}_e$. Upper left: event density for `km3neut`. Upper right: event density for `gSeaGen`. Lower left: asymmetry relative to `km3neut`. Lower right: asymmetry relative to `gSeaGen`.

than at truth level. For low y, the ratios are consistent with those at generation, except for lowest y values in ν_μ and $\bar{\nu}_\mu$ which are overrepresented at reconstruction stage in `km3neut`. At intermediate and high y, small generator-level differences are amplified by the steeply decreasing reconstruction efficiency. Relative to `gSeaGen`, `km3neut` exhibits a stronger suppression at large y, resulting in a tilted ratio indicative of generator-dependent reconstruction efficiencies rather than intrinsic differences in the true-y distributions. However, the observed deviations remain statistically compatible with fluctuations and require increased statistics for confirmation.

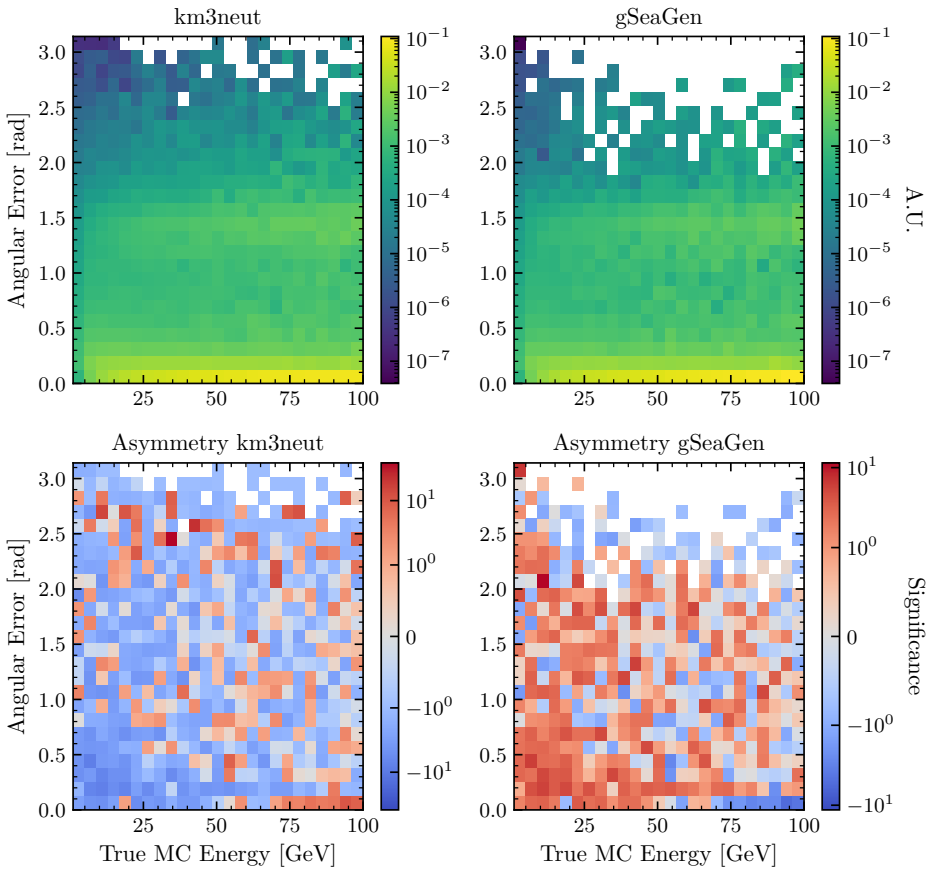

Figure 8.5.: Angular reconstruction error versus true energy for $\nu_\mu + \bar{\nu}_\mu$. Upper left: event density for `km3neut`. Upper right: event density for `gSeaGen`. Lower left: asymmetry relative to `km3neut`. Lower right: asymmetry relative to `gSeaGen`.

8.4. Survival Curves and Event Filtering

At generator level, the number of processed runs is comparable, as reflected by the similar yields of ν_e and $\bar{\nu}_e$ events. In contrast, for ν_μ and $\bar{\nu}_\mu$ approximately a factor of three more events are recorded in `km3neut` than in `gSeaGen`. This difference may arise from the vertex placement strategy, since events are retained only if the interaction vertex lies inside the instrumented volume or if the outgoing lepton intersects the detector can.

This mechanism, however, cannot explain the substantially lower statistics of ν_τ, $\bar{\nu}_\tau$, ν_{NC}, and $\bar{\nu}_{\mathrm{NC}}$ in `km3neut`, where the deficit ranges from one to more than an order of magnitude relative to `gSeaGen`, depending on flavour and channel. For ν_τ and

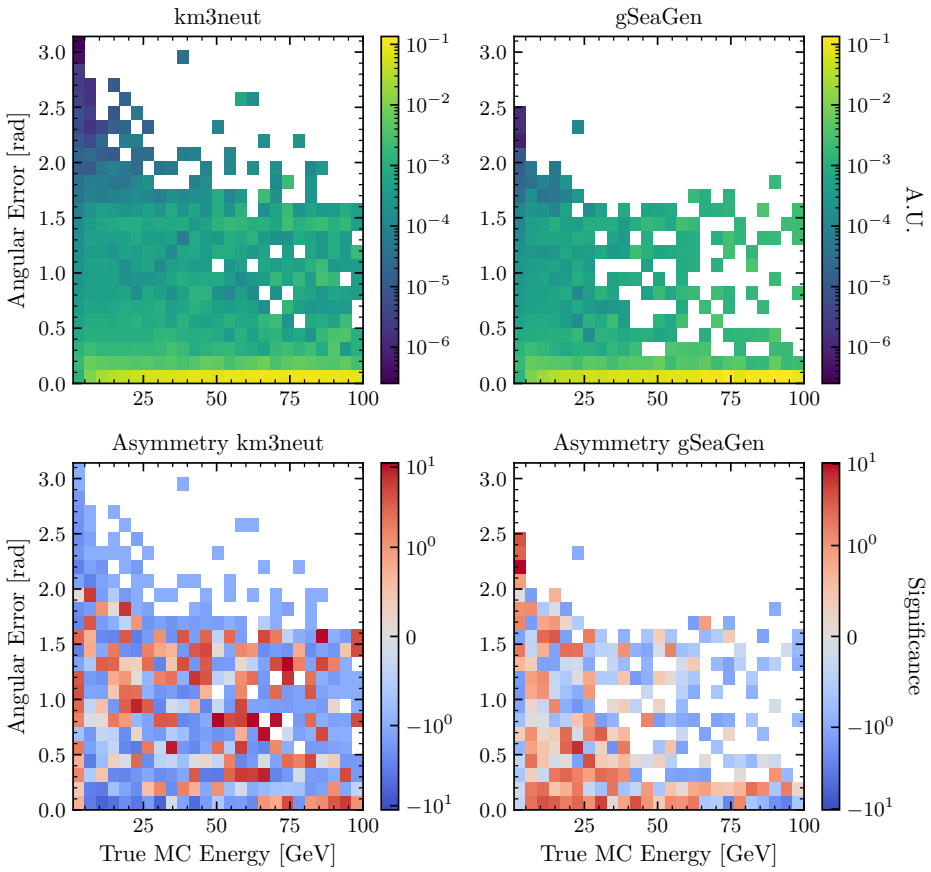

Figure 8.6.: Angular reconstruction error versus true energy for $\nu_\mu + \bar{\nu}_\mu$ with Bjorken inelasticity $y < 0.2$. Upper left: event density for `km3neut`. Upper right: event density for `gSeaGen`. Lower left: asymmetry relative to `km3neut`. Lower right: asymmetry relative to `gSeaGen`.

$\bar{\nu}_\tau$, a contributing factor may be the larger inelasticity in `km3neut`, which produces a softer $\tau^\pm$ spectrum and consequently reduces the probability that secondary $\mu^\pm$ reach the detector volume before decay. The origin of the remaining discrepancies is presently unresolved and requires further investigation of both `km3neut` and the external event interface of `gSeaGen`.

To quantify event losses along the simulation chain, survival curves are constructed as a function of true neutrino energy. The stages considered are generation, light simulation, and reconstruction. Figures Figure 8.8 and Figure 8.9 show the corresponding survival fractions for `gSeaGen` and `km3neut`.

The light→reconstruction survival probability agrees within uncertainties for both

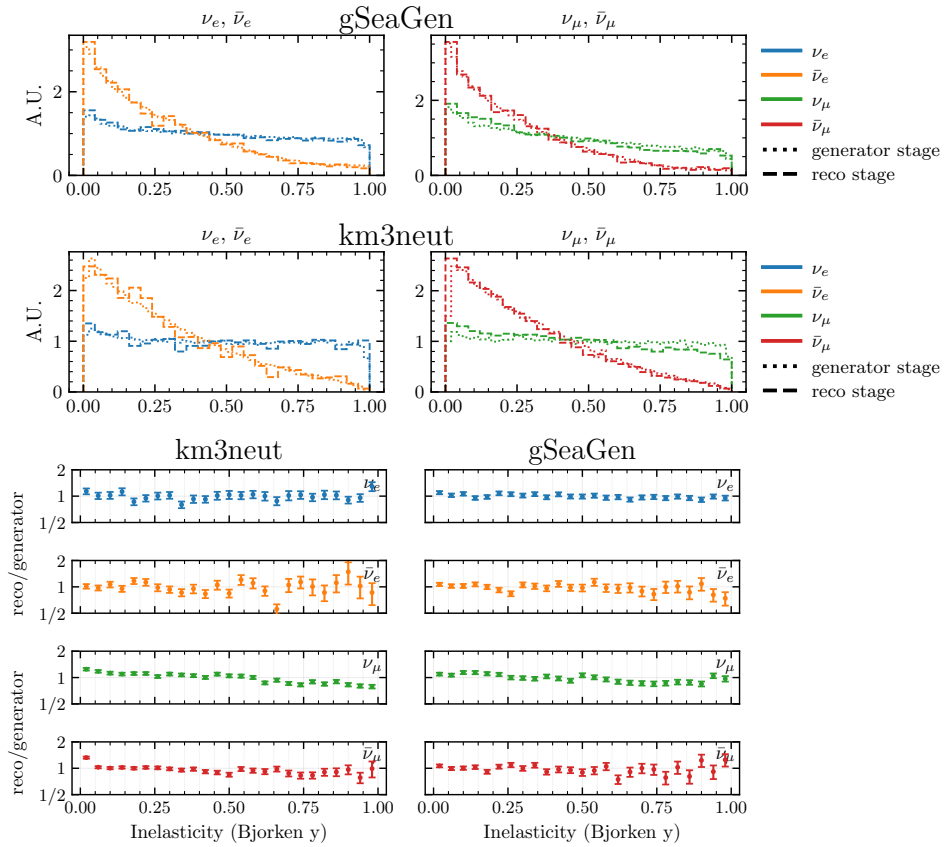

Figure 8.7.: Comparison of Bjorken-y distributions at generator and reconstruction level for `gSeaGen` (top) and `km3neut` (middle). Ratio of reconstructed to generator-level Bjorken-y distributions(bottom).

generators, indicating equivalent trigger and reconstruction performance once detectable light is produced. Consequently, all observed differences arise from the generator→light stage or from mismatches between the requested neutrino sample and the neutrinos recorded in the generator output due to event filtering done by `gSeaGen`.

For `gSeaGen`, the generator→light survival is systematically lower, particularly for ν_μ CC, ν_τ CC, and NC interactions, and exhibits a weaker energy dependence. In contrast, `km3neut` shows significantly higher generator→light efficiencies across all channels, resulting in generator→reconstruction survival fractions larger by factors of $\mathcal{O}(2\text{–}4)$ in the 10–100 GeV range. Variations in hadronic final-state modelling and vertex activity propagate through light production and reconstruction, biasing

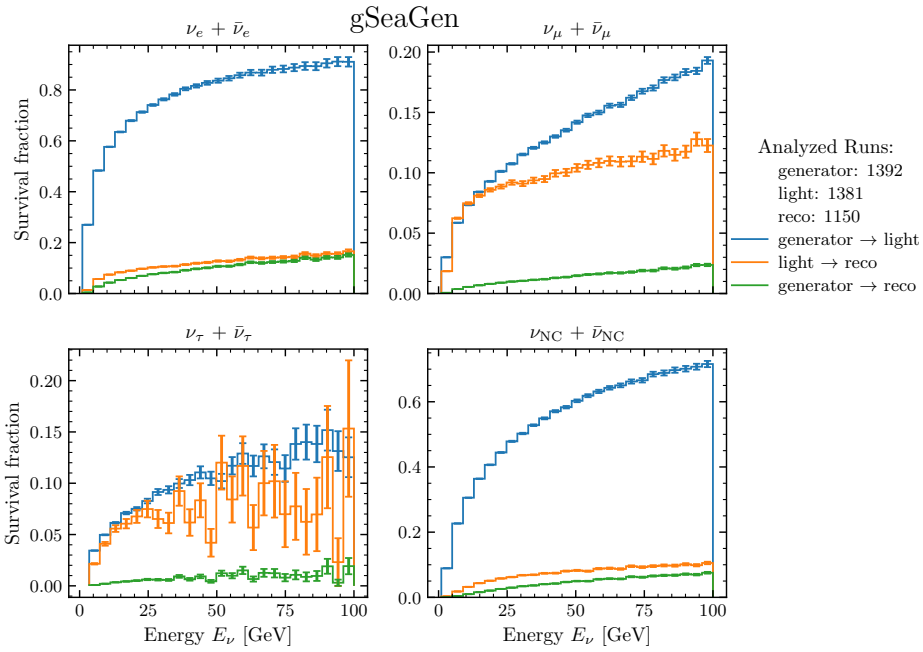

Figure 8.8.: Energy-dependent survival fractions for `gSeaGen`.

effective areas and flavour-dependent responses.

For the integration of `km3neut` into the ORCA simulation framework, the stage-dependent survival probabilities and the substantially different generator-level event yields must be explicitly accounted for.

The reconstruction stage therefore acts as a energy- and inelasticity-dependent filter. Generator-level differences in final-state modelling are amplified by this filtering, particularly at large y, and must be accounted for consistently in oscillation analyses.

8.5. Implications for ORCA

The observed generator-dependent differences propagate non-trivially into oscillation measurements. The most significant effect is the systematic shift in reconstructed energy for $\nu_\mu + \bar{\nu}_\mu$, where `km3neut` yields lower reconstructed energies than `gSeaGen` at fixed true energy. This modifies the reconstructed L/E distribution, displaces the position of the disappearance minimum, and distorts the inferred oscillation frequency. If unaccounted for, such energy-dependent migration effects can bias

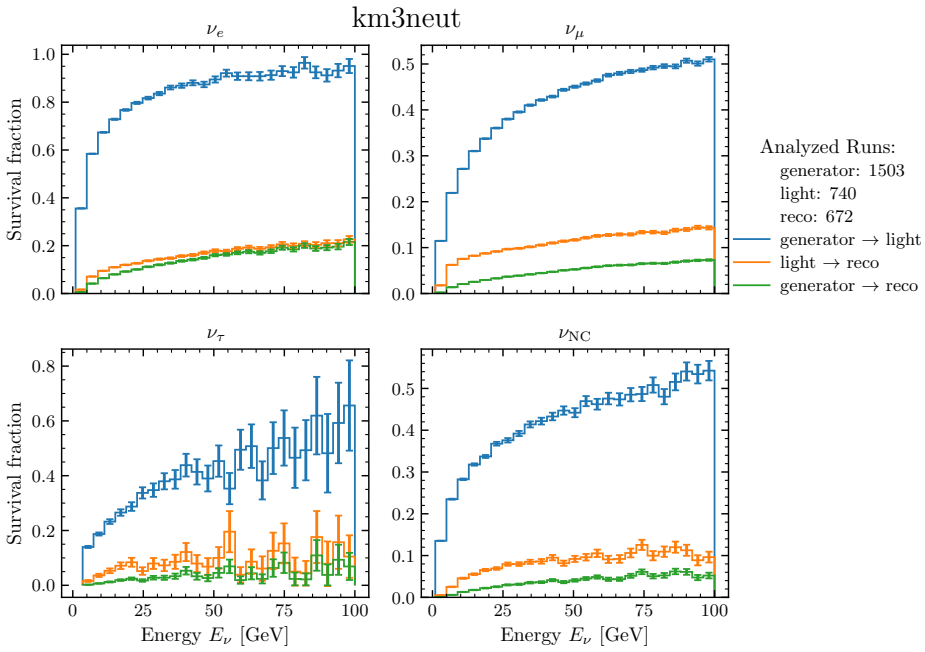

Figure 8.9.: Energy-dependent survival fractions for `km3neut`.

the extraction of oscillation parameters. Since the distortion is shape dependent, it cannot be absorbed by a simple normalization or flux tilt and must be treated as a response-function uncertainty.

Although energy reconstruction differences are small in the $\nu_e + \bar{\nu}_e$ channel, migration effects in the ν_μ disappearance sample propagate into the ν_e appearance channel through the oscillation fit. This modifies the predicted energy-dependent matter-enhanced structure and can affect the sensitivity to the neutrino mass ordering. In combined flavour analysis, inconsistent generator-induced distortions introduce correlated systematics that may reduce the overall sensitivity.

Angular reconstruction differences are driven primarily by generator-dependent Bjorken-y distributions. The larger low-energy angular uncertainty observed for $\nu_\mu + \bar{\nu}_\mu$ in `km3neut` disappears when restricting to low inelasticity ($y < 0.2$), demonstrating that the effect originates from final-state modelling rather than intrinsic reconstruction performance. Since zenith angle determines the baseline in atmospheric oscillation analyses, generator-induced differences in inelasticity translate into baseline-smearing systematics.

Reconstruction acts as an energy- and inelasticity-dependent filter that suppresses high-y events. Small generator-level differences in hadronic modelling are therefore amplified after reconstruction, leading to generator-dependent effective areas and flavour compositions. The survival probabilities show that discrepancies originate almost entirely from the generator→light stage, while light→reconstruction efficiencies are consistent. Consequently, differences in vertex placement, hadronic activity, and event filtering propagate through the full simulation chain and alter the detector response.

9. Summary, Outlook and Conclusion

This thesis has presented a comparison of the neutrino interaction generators NEUT (`km3neut`) and Generates Events for Neutrino Interaction Experiments (GENIE) (`gSeaGen`) within the Oscillation Research with Cosmics in the Abyss (ORCA) simulation and reconstruction chain, with the aim of identifying where and how generator-dependent differences arise and how they propagate to reconstructed observables relevant for oscillation analyses.

9.1. Summary

In the first part of this thesis, the theoretical and experimental framework is established. The physics of neutrino oscillations in matter, the experimental objectives of Kilometer^3 Neutrino Telescope (KM3NeT)/ORCA, and the motivation for a dedicated generator comparison are introduced in chapter 1. An overview of the structure and modelling strategies of modern neutrino event generators is provided in chapter 2. The underlying interaction physics is summarized in chapter 3, where Charged Current (CC) and Neutral Current (NC) processes, the Charged Current Quasi Elastic (CCQE), Resonant (RES), Shallow Inelastic Scattering (SIS), and Deep Inelastic Scattering (DIS) regimes, and the relevant kinematic variables are defined consistently with the observables used throughout the analysis. The Monte Carlo chain implemented in ORCA, from generator output through particle propagation, Cherenkov-light production, optical detection, and event reconstruction, is described in chapter 4. The binning strategies, normalization conventions, and comparison metrics employed in the subsequent chapters are defined in chapter 5, ensuring that generator-level and reconstruction-level differences are evaluated within a consistent statistical framework.

In chapter 6 an event-level comparison of `km3neut` and `gSeaGen` was performed for Bjorken-x, inelasticity, hadronic energy, scattering angle, visible energy, and secondary-particle multiplicities. At the cross-section level, the generators differ structurally on both hydrogen and oxygen. On free protons, `gSeaGen` activates DIS at lower energies and predicts a substantially larger diffractive component, while `km3neut` features delayed and strongly suppressed diffraction, enhanced low-energy CCQE scattering, and a larger high-energy DIS normalization. On oxygen, nuclear modelling further differentiates the predictions: `km3neut` yields a larger CCQE contribution, whereas `gSeaGen` introduces an explicit Meson Exchange Current (MEC) component with a sharp onset and termination, producing step-like features and enhancing intermediate-energy rates. These differences are most consequential in the RES–DIS transition region and around the τ production threshold, where they propagate directly to rate predictions and to the expected inelasticity spectra. Generator-level kinematics demonstrate that these discrepancies are not limited to global normalizations but correspond to phase-space dependent distortions. In Bjorken-x, `gSeaGen` populates the low-x region more strongly across channels, while `km3neut` suppresses high-x events for ν_e, ν_μ, and $\bar{\nu}_{\mathrm{NC}}$, consistent with different treatments of large-Q^2 scattering and the SIS–DIS transition. The y distributions exhibit channel-dependent distortions: `km3neut` predicts a narrower y spectrum for several antineutrino channels, a shift toward higher inelasticities for ν_μ, and systematically larger inelasticities for ν_τ, implying altered energy partitioning between the charged lepton and hadronic system. Angular observables show further generator dependence. While ν_e CC scattering-angle distributions agree well, large discrepancies appear for $\bar{\nu}_e$ and $\bar{\nu}_\mu$ at wide lepton angles and for ν_μ with the opposite trend, indicating differences in momentum-transfer modelling. Hadronic-angle distributions exhibit the strongest disagreement in NC channels, where `gSeaGen` predicts substantially broader hadronic systems; for ν_τ the differences reach orders of magnitude at large angles, consistent with incomplete or non-standard model coverage in the default `km3neut` configuration for ν_τ DIS.

Visible-energy distributions are broadly compatible in shape for several channels but show persistent differences in the tails and in the visible-energy fraction. In particular, `km3neut` exhibits a deficit at low E_{vis}/E_{ν} for ν_e and ν_μ, while ν_μ CC events show an enhanced high-E_{vis} population. Two-dimensional correlations reinforce that these effects are coupled: correlations between y and lepton or hadronic angles reveal generator-dependent distortions of the energy–angle mapping, implying differences in transverse-momentum balance and hadronic recoil. Secondary-particle multiplicities indicate non-trivial differences in hadronization, particularly for strangeness. While pion yields are broadly similar up to normalization shifts, kaon yields are systematically lower in `km3neut`, and Λ production is suppressed by about an order of magnitude relative to `gSeaGen`, pointing to a reduced strange-baryon component. In chapter 7 this comparison is extended to the light-simulation stage. After reweighting to a common neutrino-energy and vertex distribution, the strongest discrepancies appear in $\nu_\mu/\bar{\nu}_\mu$ CC interactions, where `km3neut` systematically predicts higher detected-photon yields, shorter event timespans, and an earlier saturation of the last-photon time at high energy. This pattern is not consistent with a global timing offset but instead reflects differences in secondary-particle kinematics, dominated by muon-induced light and influenced by generator-dependent inelasticity and hadronic modelling. For $\nu_e/\bar{\nu}_e$ CC channels, timing differences are confined to low energies, yet `km3neut` still shows a persistent excess in mean photon yield, consistent with modified electron- and π^0-induced contributions. Neutral Current (NC) interactions display increased pion-attributed photon contributions in `km3neut` yet broadly compatible mean total yields, with `gSeaGen` preferentially populating the low-energy, low-light region.

Within the ORCA framework, the reconstruction-level comparison demonstrates that the choice of generator induces channel-dependent differences already in the surviving event counts. These differences originate predominantly in the generator→light stage. Survival-curve studies show that light→reconstruction efficiencies agree within uncertainties for both generators, whereas `gSeaGen` exhibits systematically

lower generator→light survival, especially for ν_μ CC, ν_τ CC and NC interactions. Consequently, generator→reconstruction survivals are larger for `km3neut` by factors of $\mathcal{O}(2\text{–}4)$ in the 10–100 GeV range, consistent with generator-dependent final-state activity propagating through light production.

In reconstructed energy, $\nu_e + \bar{\nu}_e$ events cluster close to the identity line for both generators, with a small opposite bias, `km3neut` slightly overestimating and `gSeaGen` slightly underestimating E_{reco}. For $\nu_\mu + \bar{\nu}_\mu$, a clearer systematic shift is observed: for fixed true energy, `km3neut` reconstructs lower energies than `gSeaGen`, implying a correlated, energy-dependent response-function systematic. Angular reconstruction is broadly consistent inclusively between generators, with generator-dependent structure mainly confined to low energies for $\nu_\mu + \bar{\nu}_\mu$, driven by differences in the inelasticity distributions. Reconstruction distorts the inelasticity distribution by suppressing high-y events relative to generator truth. This selection enhances generator-level discrepancies and implies generator-dependent reconstruction efficiencies at large y. Owing to limited statistics, this effect cannot be quantified conclusively. Owing to limited statistics, especially in the $\nu_\tau + \bar{\nu}_\tau$ and NC samples, these trends cannot yet be quantified with high significance but provide a clear direction for further work.

9.2. Conclusion

The combined results show that the `km3neut-gSeaGen` differences correspond to correlated, kinematics-dependent distortions across phase space rather than to a global normalization shift. For ORCA, this implies that generator uncertainties cannot be represented by a simple cross-section scaling. Instead, correlated variations affecting $\sigma(E_\nu)$, the inelasticity distribution, angular observables, and the composition of hadronic final states must be considered simultaneously. In particular, the energy-dependent shifts observed in reconstructed E_{reco} for $\nu_\mu + \bar{\nu}_\mu$ would translate into distortions of reconstructed L/E, potentially shifting oscillation features if untreated.

This conclusion is even more critical for the ν_τ appearance channel. The production threshold, the strong dependence of the cross section on energy in the threshold region, and the complex decay of the τ lepton render ν_τ interactions intrinsically sensitive to the detailed modelling of inelasticity, hadronic recoil, and secondary-particle spectra. The generator-level differences observed in cross sections near the τ threshold and in the RES–DIS transition region therefore directly affect both the predicted rate and the visible-energy response of ν_τ events. Since ν_τ appearance in ORCA is identified statistically through its impact on event-class composition and reconstructed energyangle distributions rather than through explicit τ tagging, generator-dependent distortions of the y distribution and of hadronic final states can modify the efficiency, migration patterns, and flavour classification of ν_τ events in a correlated manner.

Consequently, uncertainties in ν_τ modelling are not confined to an overall normalization of the appearance signal but propagate into the reconstructed L/E spectrum and into the relative population of track- and cascade-like events. This is particularly relevant in the context of precision measurements of oscillation parameters and tests of unitarity in the ν_τ sector, where a mis-modelling of the appearance channel could mimic or obscure genuine oscillation effects. The pronounced deviations observed in the NC sector and in the ν_τ appearance channel therefore indicate that these channels require dedicated treatment in any systematic uncertainty model.

A translation between generators based solely on inclusive cross-section reweighting is therefore insufficient. Generator-dependent differences in the underlying multi-dimensional kinematic distributions must be incorporated, requiring reweighting schemes that preserve correlations among the relevant observables, especially in the threshold-dominated and high-inelasticity regions that govern ν_τ appearance.

9.3. Outlook

Further investigation is required to quantify these effects with statistical significance. The impact on reconstructed observables is presently statistics-limited, and a

substantially larger event sample is necessary, particularly for ν_τ, $\bar{\nu}_\tau$, ν_{NC}, and $\bar{\nu}_{\mathrm{NC}}$ interactions. The deficit of these samples must be understood or consistently corrected for before firm conclusions can be drawn regarding their propagation through the light-simulation and reconstruction stages.

To disentangle whether the observed deviations arise from isolated modelling components or from a limited set of underlying differences, targeted reweighting studies can be performed. For example, reweighting a single observable such as the inelasticity to enforce agreement at the level of its marginal distribution between generators removes differences attributable solely to that marginal. If discrepancies persist in other observables after this controlled adjustment, they necessarily originate from differences in conditional distributions or correlations beyond the reweighted variable. Conversely, if most deviations disappear, the reweighted observable can be identified as a dominant driver of the variation.

Additionally, the applied reweighting in chapter 7 does not preserve a uniform neutrino-energy spectrum; instead, the effective distribution scales as $\sigma(E_\nu)$, enhancing the relative contribution of high-energy interactions and shifting the normalization toward large E_ν. As a consequence, statistical uncertainties increase at high energies, while the overall statistical sensitivity remains dominated by low-energy interactions. This induces an energy-dependent normalization bias toward high energies which is not corrected for in the present interpretation. A consistent extension would therefore be a bin-by-bin normalization in E_ν, factorizing the spectral shape from the absolute rate within each neutrino-energy interval. Such a procedure would remove the energy-dependent normalization bias while retaining differential shape information and would simultaneously eliminate potential differences in generator→light survival rates, thereby isolating genuine kinematic effects from rate-driven distortions.

The role of hadronic energy spectra and particle composition at the light stage should also be studied in more detail. Particle multiplicities alone are insufficient to characterize generator-induced differences in Cherenkov light production. Differential

energy spectra of secondary pions, kaons, and baryons, as well as their angular distributions, should be propagated through the light simulation to determine which components dominate photon-yield and timing differences. In particular, the strongly suppressed strange-baryon production in `km3neut` relative to `gSeaGen` motivates a dedicated study of strangeness-induced light contributions and their possible impact on cascade development.

Finally, the quantitative impact of the observed generator-dependent differences on oscillation parameter extraction and searches for physics Beyond Standard Model (BSM) remains unaddressed. The magnitude and direction of potential biases in extracted parameters or limits are therefore presently unknown and require dedicated studies within the ORCA oscillation-analysis framework.

Acronyms

2p2h two particles-two holes.

3p3h three particles-three holes.

ANTARES Astronomy with a Neutrino Telescope and Abyss environmental RE-Search project.

ARCA Astroparticle Research with Cosmics in the Abyss.

B.T. Below Threshold.

BSM Beyond Standard Model.

CC Charged Current.

CCQE Charged Current Quasi Elastic.

COH Coherent.

DIF Diffractive.

DIS Deep Inelastic Scattering.

DOM Digital Optical Modules.

DST summary file.

DU Detection Unit.

DUNE Deep Underground Neutrino Experiment.

FSI Final State Interaction.

GENIE Generates Events for Neutrino Interaction Experiments.

GiBUU Giessen Boltzmann-Uehling-Uhlenbeck.

KM3NeT Kilometer^3 Neutrino Telescope.

MEC Meson Exchange Current.

MINERνA Main Injector Neutrino ExpeRiment to study ν-A interactions.

N.A. Not Available.

NC Neutral Current.

NCEL Neutral Current Elastic.

NOνA NuMI Off-axis ν_e Appearance.

ORCA Oscillation Research with Cosmics in the Abyss.

PCAC Partially Conserved Axial Vector Current.

PMT Photomultiplier Tube.

RES Resonant.

SIS Shallow Inelastic Scattering.

SK Super Kamiokande.

T2K Tokai to Kamioka.

Bibliography

[1] Wolfgang Pauli. *Offener Brief an die Gruppe der Radioaktiven bei der Gauvereins-Tagung zu Tübingen*. Online as of 01.03.2026. 1930. URL: https://sis.web.cern.ch/archives/history_CERN/historical_images/month-88-years-ago.

[2] James Chadwick. "The existence of a neutron". In: *Proceedings of the Royal Society of London. Series A, Containing Papers of a Mathematical and Physical Character* 136.830 (June 1932), pp. 692–708. DOI: 10.1098/rspa.1932.0112.

[3] Enrico Fermi. "Tentativo di una Teoria Dei Raggi β". In: *Il Nuovo Cimento (1924-1942)* (1934). DOI: 10.1007/BF02959820.

[4] Enrico Fermi. "Versuch einer Theorie der β-Strahlen. I." In: *Zeitschrift für Physik* (1934). DOI: 10.1007/BF01351864.

[5] Joanna Rose. *The chameleons of space. Popular schience background, The Nobel Prize in Physics 2015*. Ed. by Gunnar Ingelman Lars Bergström Olga Botner and the Nobel Committee for Physics Anne LHuillier. Online as of 01.03.2026. URL: https://www.nobelprize.org/uploads/2018/06/popular-physicsprize2015.pdf.

[6] C. L. Cowan, F. Reines, F. B. Harrison, H. W. Kruse, and A. D. McGuire. "Detection of the Free Neutrino: a Confirmation". In: *Science* 124.3212 (1956), pp. 103–104. DOI: 10.1126/science.124.3212.103.

[7] The Nobel Foundation. *The Nobel Prize 1995*. Online as of 01.03.2026. URL: https://www.nobelprize.org/prizes/physics/1995/summary/.

[8] G. Danby, J-M. Gaillard, K. Goulianos, et al. “Observation of High-Energy Neutrino Reactions and the Existence of Two Kinds of Neutrinos”. In: *Phys. Rev. Lett.* 9 (1 July 1962), pp. 36–44. DOI: 10.1103/PhysRevLett.9.36.

[9] The Nobel Foundation. *The Nobel Prize 1988*. Online as of 01.03.2026. URL: https://www.nobelprize.org/prizes/physics/1988/summary/.

[10] K. Kodama, N. Ushida, C. Andreopoulos, et al. “Observation of tau neutrino interactions”. In: *Physics Letters B* 504.3 (Apr. 2001), pp. 218–224. ISSN: 0370-2693. DOI: 10.1016/s0370-2693(01)00307-0.

[11] Salvatore Mele. “The Measurement of the Number of Light Neutrino Species at LEP”. In: *Adv. Ser. Direct. High Energy Phys.* 23 (2015), pp. 89–106. DOI: 10.1142/9789814644150_0004.

[12] Bruce T. Cleveland, Timothy Daily, Raymond Davis Jr., et al. “Measurement of the Solar Electron Neutrino Flux with the Homestake Chlorine Detector”. In: *The Astrophysical Journal* 496.1 (Mar. 1998), p. 505. DOI: 10.1086/305343.

[13] A. Bellerive, J.R. Klein, A.B. McDonald, A.J. Noble, and A.W.P. Poon. “The Sudbury Neutrino Observatory”. In: *Nuclear Physics B* 908 (July 2016), pp. 30–51. ISSN: 0550-3213. DOI: 10.1016/j.nuclphysb.2016.04.035.

[14] The Nobel Foundation. *The Nobel Prize 2015*. Online as of 01.03.2026. URL: https://www.nobelprize.org/prizes/physics/2015/summary/.

[15] C. A. Argüelles, G. Barenboim, M. Bustamante, et al. “Snowmass white paper: beyond the standard model effects on neutrino flavor”. In: *The European Physical Journal C* 83.1 (Jan. 2023), p. 15. ISSN: 1434-6052. DOI: 10.1140/epjc/s10052-022-11049-7.

[16] KM3NeT Collaboration. “KM3NeT constraint on Lorentz-violating superluminal neutrino velocity”. In: *Communications Physics* 8.1 (Nov. 2025), p. 457. ISSN: 2399-3650. DOI: 10.1038/s42005-025-02347-z.

[17] Alba Domi, Thomas Eberl, Max Joseph Fahn, et al. “Understanding gravitationally induced decoherence parameters in neutrino oscillations using a microscopic quantum mechanical model”. In: *Journal of Cosmology and Astroparticle Physics* 2024.11 (Nov. 2024), p. 006. ISSN: 1475-7516. DOI: 10.1088/1475-7516/2024/11/006.

[18] Nick E. Mavromatos, Anselmo Meregaglia, André Rubbia, Alexander S. Sakharov, and Sarben Sarkar. “Quantum-gravity decoherence effects in neutrino oscillations: Expected constraints from CNGS and J-PARC”. In: *Phys. Rev. D* 77 (5 Mar. 2008), p. 053014. DOI: 10.1103/PhysRevD.77.053014.

[19] Michelle J. Dolinski, Alan W.P. Poon, and Werner Rodejohann. “Neutrinoless Double-Beta Decay: Status and Prospects”. In: *Annual Review of Nuclear and Particle Science* 69.1 (Oct. 2019), pp. 219–251. ISSN: 1545-4134. DOI: 10.1146/annurev-nucl-101918-023407.

[20] Carlo Giunti and Thierry Lasserre. “eV-Scale Sterile Neutrinos”. In: *Annual Review of Nuclear and Particle Science* 69.1 (Oct. 2019), pp. 163–190. ISSN: 1545-4134. DOI: 10.1146/annurev-nucl-101918-023755.

[21] The KM3NeT Collaboration. “Letter of intent for KM3NeT 2.0”. In: *Journal of Physics G: Nuclear and Particle Physics* 43.8 (June 2016), p. 084001. ISSN: 1361-6471. DOI: 10.1088/0954-3899/43/8/084001.

[22] The ANTARES Collaboration. “The ANTARES detector: two decades of neutrino searches in the Mediterranean Sea”. In: *Physics Reports* 1121-1124 (2025), pp. 1–46. ISSN: 0370-1573. DOI: https://doi.org/10.1016/j.physrep.2025.04.001.

[23] IceCube Collaboration. “First year performance of the IceCube neutrino telescope”. In: *Astroparticle Physics* 26.3 (Oct. 2006), pp. 155–173. ISSN: 0927-6505. DOI: 10.1016/j.astropartphys.2006.06.007.

[24] E.M. Lifschitz; Paul Ziesche (Hrsg.) L.D. Landau. *Lehrbuch der Theoretischen Physik - Band VIII - Elektrodynamik der Kontinua VIII*. 5th ed. Lehrbuch der Theoretischen Physik - VIII. Akademie-Verlag, 1985.

[25] The KM3NeT Collaboration. "Observation of an ultra-high-energy cosmic neutrino with KM3NeT". In: *Nature* (2025). DOI: 10.1038/s41586-024-08543-1.

[26] Andrey Romanov and Valentin Pestel. "Measurement of optical water properties using stopping muons in KM3NeT/ORCA". In: *PoS* ICRC2025 (2025), p. 1158. DOI: 10.22323/1.501.1158.

[27] P. Coloma, P. Huber, C.-M. Jen, and C. Mariani. "Neutrino-nucleus interaction models and their impact on oscillation analyses". In: *Physical Review D* 89.7 (Apr. 2014). ISSN: 1550-2368. DOI: 10.1103/physrevd.89.073015.

[28] Nina M. Coyle, Shirley Weishi Li, and Pedro A.N. Machado. "The impact of neutrino-nucleus interaction modeling on new physics searches". In: *JHEP* 12 (Dec. 2022). DOI: 10.1007/JHEP12(2022)166.

[29] Ulrich Mosel. "Neutrino event generators: foundation, status and future". In: *Journal of Physics G: Nuclear and Particle Physics* 46.11 (Sept. 2019), p. 113001. ISSN: 1361-6471. DOI: 10.1088/1361-6471/ab3830.

[30] J. M. Campbell, M. Diefenthaler, T. J. Hobbs, et al. *Event Generators for High-Energy Physics Experiments*. 2025. arXiv: 2203.11110 [hep-ph]. URL: https://arxiv.org/abs/2203.11110.

[31] C. Andreopoulos et al. "The GENIE Neutrino Monte Carlo Generator". In: *Nucl. Instrum. Meth. A* 614 (2010), pp. 87–104. DOI: 10.1016/j.nima.2009.12.009. arXiv: 0905.2517 [hep-ph].

[32] Costas Andreopoulos, Christopher Barry, Steve Dytman, et al. "The GENIE Neutrino Monte Carlo Generator: Physics and User Manual". In: *arxiv* (Oct. 2015). arXiv: 1510.05494 [hep-ph].

[33] O. Buss, T. Gaitanos, K. Gallmeister, et al. “Transport-theoretical description of nuclear reactions”. In: *Physics Reports* 512.1-2 (Mar. 2012), pp. 1–124. ISSN: 0370-1573. DOI: 10.1016/j.physrep.2011.12.001.

[34] T. Golan, J.T. Sobczyk, and J. Zmuda. “NuWro: the Wroclaw Monte Carlo Generator of Neutrino Interactions”. In: *Nuclear Physics B - Proceedings Supplements* 229-232 (2012). Neutrino 2010, p. 499. ISSN: 0920-5632. DOI: https://doi.org/10.1016/j.nuclphysbps.2012.09.136.

[35] Cezary Juszczak, Jaroslaw A. Nowak, and Jan T. Sobczyk. “Simulations from a new neutrino event generator”. In: *Nuclear Physics B - Proceedings Supplements* 159 (2006). Proceedings of the 4th International Workshop on Neutrino-Nucleus Interactions in the Few-GeV Region, pp. 211–216. ISSN: 0920-5632. DOI: 10.1016/j.nuclphysbps.2006.08.069.

[36] Yoshinari Hayato. “A neutrino interaction simulation program library NEUT”. In: *Acta Phys. Polon. B* 40 (2009). Ed. by Arthur Ankowski and Jan Sobczyk, pp. 2477–2489. DOI: 10.1140/epjs/s11734-021-00287-7.

[37] Yoshinari Hayato and Luke Pickering. “The NEUT neutrino interaction simulation program library”. In: *The European Physical Journal Special Topics* 230.24 (Oct. 2021), pp. 4469–4481. ISSN: 1951-6401. DOI: 10.1140/epjs/s11734-021-00287-7.

[38] Yoshinari Hayato, Luke Pickering, Seisho Abea, and Clarence Wret. Official (private) repository for the NEUT, the neutrino event generator. In this work NEUT commit 24c2a8ac7848eb2cb70e56847d60cf858c730767 is used with some custom modifications. URL: https://github.com/neut-devel/neut.

[39] Joshua Isaacson, William I. Jay, Alessandro Lovato, Pedro A. N. Machado, and Noemi Rocco. “Introducing a novel event generator for electron-nucleus and neutrino-nucleus scattering”. In: *Physical Review D* 107.3 (Feb. 2023). ISSN:

2470-0029. DOI: 10.1103/physrevd.107.033007. URL: https://github.com/AchillesGen/Achilles.

[40] Joshua Isaacson, Stefan Höche, Diego Lopez Gutierrez, and Noemi Rocco. "Novel event generator for the automated simulation of neutrino scattering". In: *Phys. Rev. D* 105.9 (2022), p. 096006. DOI: 10.1103/PhysRevD.105.096006. arXiv: 2110.15319 [hep-ph].

[41] Torbjorn Sjostrand. *PYTHIA 5.7 and JETSET 7.4 Physics and Manual*. 1995. arXiv: hep-ph/9508391 [hep-ph]. URL: https://arxiv.org/abs/hep-ph/9508391.

[42] Torbjörn Sjöstrand, Stephen Mrenna, and Peter Skands. "PYTHIA 6.4 physics and manual". In: *Journal of High Energy Physics* 2006.05 (May 2006), pp. 026–026. ISSN: 1029-8479. DOI: 10.1088/1126-6708/2006/05/026.

[43] Christian Bierlich, Smita Chakraborty, Nishita Desai, et al. *A comprehensive guide to the physics and usage of PYTHIA 8.3*. 2022. arXiv: 2203.11601 [hep-ph]. URL: https://arxiv.org/abs/2203.11601.

[44] R. Gran, J. Nieves, F. Sanchez, and M. J. Vicente Vacas. "Neutrino-nucleus quasi-elastic and 2p2h interactions up to 10 GeV". In: *Phys. Rev. D* 88 (11 Dec. 2013), p. 113007. DOI: 10.1103/PhysRevD.88.113007.

[45] Ch. Berger and L. M. Sehgal. "Partially conserved axial vector current and coherent pion production by low energy neutrinos". In: *Phys. Rev. D* 79 (5 Mar. 2009), p. 053003. DOI: 10.1103/PhysRevD.79.053003.

[46] Mark Andrew Thomson. *Modern Particle Physics*. Cambridge University, 2013. ISBN: 978-1-107-03426-6. DOI: 10.1017/CBO9781139525367.

[47] Bogdan Povh, Klaus Rith, Christoph Scholz, Frank Zetsche, and Werner Rodejohann. *Teilchen und Kerne*. Springer, 2013. ISBN: 978-3-642-37821-8. DOI: 10.1007/978-3-642-37822-5.

[48] Peter Schuck Peter Ring. *The Nuclear Many-Body Problem*. Springer, 2004. ISBN: 978-3-540-21206-5.

[49] J. Edelmann, G. Piller, and W. Weise. "Deuteron spin structure functions at small Bjorken x". In: *Physical Review C* 57.6 (June 1998), pp. 3392–3405. ISSN: 1089-490X. DOI: 10.1103/physrevc.57.3392.

[50] I Ruiz Simo, J E Amaro, M B Barbaro, et al. "Relativistic model of 2p-2h meson exchange currents in (anti)neutrino scattering". In: *Journal of Physics G: Nuclear and Particle Physics* 44.6 (Apr. 2017), p. 065105. ISSN: 1361-6471. DOI: 10.1088/1361-6471/aa6a06.

[51] J. G. H. de Groot, T. Hansl, M. Holder, et al. "Inclusive interactions of high-energy neutrinos and antineutrinos in iron". In: *Zeitschrift für Physik C Particles and Fields* 1.2 (June 1979), pp. 143–162. ISSN: 1431-5858. DOI: 10.1007/BF01445406.

[52] Mona Dentler. "Investigation of the One-Particle Approximation in the ANTARES simulation package KM3". Bachelors thesis. Friedrich-Alexander-Universität Erlangen-Nürnberg, Oct. 2012. URL: https://ecap.nat.fau.de/wp-content/uploads/2017/05/2012_Dentler_Bachelor.pdf.

[53] KM3NeT collaboration. *run-based-data-processing git repository*. Collaboration internal, comit tag: b93e6b7705ff30461ef0477cb9b7b56a8efc0a46. URL: https://git.km3net.de/workflow-management/run-based-data-processing.

[54] Johannes Köster and Sven Rahmann. "Snakemakea scalable bioinformatics workflow engine". In: *Bioinformatics* 28.19 (Aug. 2012), pp. 2520–2522. ISSN: 1367-4803. DOI: 10.1093/bioinformatics/bts480. eprint: https://academic.oup.com/bioinformatics/article-pdf/28/19/2520/48879301/bioinformatics_28_19_2520.pdf. URL: https://doi.org/10.1093/bioinformatics/bts480.

[55] KM3NeT Collaboration. "gSeaGen: The KM3NeT GENIE-based code for neutrino telescopes". In: *Computer Physics Communications* 256 (2020), p. 107477. DOI: https://doi.org/10.1016/j.cpc.2020.107477.

[56] Frederik Andersen. The tag used in this work is v1.5, Collaboration and institute internal; https://git.ecap.work/AndersenFred/km3neut.git; https://git.km3net.de/-fandersen/km3neut.

[57] The KM3NeT collaboration. Not publicly available. URL: https://git.km3net.de/common/km3net-dataformat.git.

[58] A.G. Tsirigotis, A. Leisos, and S.E. Tzamarias. "HOU Reconstruction & Simulation (HOURS): A complete simulation and reconstruction package for very large volume underwater neutrino telescopes". In: *Nuclear Instruments and Methods in Physics Research Section A: Accelerators, Spectrometers, Detectors and Associated Equipment* 626-627 (2011), S185–S187. ISSN: 0168-9002. DOI: https://doi.org/10.1016/j.nima.2010.06.258. URL: https://www.sciencedirect.com/science/article/pii/S0168900210014488.

[59] M. de Jong and E. van Campenhout. *The probability density function of the arrival time of Cherenkov light*. 2023. arXiv: 2305.19626 [astro-ph.IM]. URL: https://arxiv.org/abs/2305.19626.

[60] Frederik Andersen. Collaboration / Institute internal; https://git.km3net.de/fandersen/generator-comparison; https://git.ecap.work/AndersenFred/neut_vs_genie.

[61] Frederik Andersen. Collaboration / Institute internal; https://git.ecap.work/AndersenFred/crosssection; https://git.km3net.de/fandersen/crosssections.

List of Figures

A. Customizations in NEUT

The following modifications were required to ensure stable event generation. All changes refer to the commit tag used in this thesis [38].

A.1. Hydrogen Support

In the default NEUT implementation, the number of bound neutrons is computed as

```
numbndn = numatom - numbndp;
```

with numbndp, numatom, and numfrep defined in neut/src/config/readcard.cc. Because NEUT assigns Fermi motion to all bound nucleons while allowing free protons to be associated with a nuclear target, hydrogen ($A = 1$, $Z = 1$) requires special treatment. Without this correction, neutrino–hydrogen interactions inherit unphysical nuclear effects.

The expression was therefore replaced by

```
neuttarget.numbndn = (neuttarget.numatom == 1 && neuttarget.
   numfrep == 1) ? 0 : neuttarget.numatom - neuttarget.numbndp
   ;
```

ensuring that no bound neutrons are assigned to hydrogen targets.

A.2. Deep Inelastic Scattering on Tau Neutrinos

During DIS event generation, Pythia attempts to decay the produced τ lepton internally resulting in `(LUROBO:) boost vector too large` and other warnings like `*** WARNING *** TOO MANY ERR AT NEVENT`. Presumably due to inconsistent

τ-mass definitions across the codebase[1], Lorentz boosts into and out of the τ rest frame can exceed unity, leading to an infinite loop during event generation.

The decay is intended to be disabled when `neutcard%ITAUFLGCORE = 1`; however, this variable is never initialized, and the condition is therefore never satisfied.

In `neut/src/models/MPiDIS/nejet.F`, the conditional block

```
IF(neutcard%ITAUFLGCORE.eq.1) THEN
   MDCY(LUCOMP(15),1) = 0
ENDIF
```

was replaced by an unconditional statement,

```
MDCY(LUCOMP(15),1) = 0
```

ensuring that `Pythia` never decays the τ lepton. The lepton is instead decayed by `Tauola` at a later stage.

A.3. Final-State Interaction Stability

Several Fortran arrays used to track Final State Interaction (FSI) histories can exceed their effective bounds for rare but pathological event topologies, leading to index-out-of-bounds memory access.

A.3.1. Final State Interaction History Guards

In `nrnuc.F`, writes to `nfiekin(NFNStep)` are now protected:

[1] (e.g. `core/ParticleMasses.cc`: 1776.99 MeV, `models/contrib/rmf/Constants.h`: 1777.09 MeV, `models/contrib/n1p1h/src/N1p1h.C` and `models/contrib/n1p1h/src/qe.F`: 1776.82 MeV, `tauola/pkorb.F`: 1.777 GeV, `tauola/taupol.f`: 1.78 GeV, `models/diffractive/ddifcrs.F`: 1784.1 MeV)

```
if (nucleonfsihist%NFNStep .le. 10000) then
   nucleonfsihist%nfiekin(nucleonfsihist%NFNStep) = ekin
else
   write(*,*) "WARNING (nrnuc): NFNStep > 10000, skipping
   nfiekin store"
endif
```

Analogous protections were added in `nrprton.F` for `NFecms2`, `NFnstep`, `NFptot` and `NFnstep`. Additionally, the cascade is terminated once a maximum nucleon step count is reached:

```
if (nucleonfsihist%NFnstep .lt. maxnucleonstep) then
   nucleonfsihist%NFnstep = nucleonfsihist%NFnstep + 1
else
   write(*,*) "WARNING (nrprton): reached maxnucleonstep"
   goto 99
endif
```

A.3.2. Pion FSI Numerical Protection

The above changes exposed a secondary instability in pion FSI propagation. In `efabpathtun.F`, the pion channel index is now clamped to the physically valid range:

```
25    CONTINUE
      if (J .lt. 2) J = 2
      if (J .gt. 8) J = 8
```

In `eftrace.F`, a NaN-safety guard was introduced. If any component of the pion momentum or position becomes NaN, the pion is forced to escape the nucleus and its state is reset:

```
if (P(1).ne.P(1) .or. P(2).ne.P(2) .or. P(3).ne.P(3) .or.
&    X(1).ne.X(1) .or. X(2).ne.X(2) .or. X(3).ne.X(3)) then
   write(*,*) "EFTRACE: NaN detected, forcing escape"
   do I = 1, 3
      P(I)   = PIN(I)
      X(I)   = XIN(I)
      PFI(I) = PIN(I)
   end do
   NABS  = 0
   NEL   = 0
   NINEL = 0
   KFI   = KIN
   return
endif
```

A.3.3. Common Block Interface and File Safety

To allow controlled access to the generator card, needed for a rewritten main enabling composed media, the `CommonBlockIFace` singleton was modified to return a non-const reference and to expose a setter for the generator card path:

```
static CommonBlockIFace &Get();
void SetGenCard(std::string const &GenCardLocation);
```

Finally, in `nerdseed.F`, an explicit `CLOSE` statement was inserted prior to returning from the routine, ensuring that `NEUT` reopens and rereads the seed file on each invocation. This modification is required because a new seed file is created for every target.

```
CLOSE(99)
RETURN
```

A.4. Coherent Neutrino Scattering and 3p3h

No coherent neutrino scattering events are present in the produced output files. The origin of this behavior could not be conclusively identified. However, all attempted simulations of coherent interactions consistently resulted in kinematical warnings from `NEUT`. In particular, the generator repeatedly issued the warning `*** WARNING *** KINEMATICAL ERROR AT NECOHVCT (MODE,E)`. As no physically valid events were produced this interaction mode was disabled in order to reduce unnecessary computational overhead.

In addition, the 3p3h interaction channel was disabled, as its inclusion significantly increased the frequency of `NEUT` crashes.

A.5. Final Comments on `NEUT`

The modifications described above resolve several stability issues and enable reliable simulations of hydrogen targets, ν_τ deep-inelastic scattering, and high-multiplicity FSI chains. Although a small fraction of events is removed at subsequent stages-of order 1 per $\mathcal{O}(10^7)$ by estimate-`NEUT` still exhibits residual instabilities, with crashes occurring at a rate of approximately one per $\mathcal{O}(10^7)$ generated events, averaged over neutrino flavors. No further investigation was performed to identify the specific interaction channel or flavor responsible for these failures.

These findings also highlight structural deficiencies in the current `NEUT` code base, including missing or incomplete initialization, inconsistent physical constants, hard-coded and insufficiently guarded array bounds, and a lack of internal validation checks.

A transition toward transparent, community-maintained open-source development is desirable, for long-term maintainability and scientific reliability. Equally important is the establishment of continuous integration and testing infrastructure to prevent regressions and to ensure that new developments do not compromise existing functionality.

A significant limitation is the continued use of Pythia 5.7, a legacy release from the early 1990s that predates double-precision numerics, modern parton-shower refinements, contemporary PDF sets, and LHC-era model tuning [42, 43]. Although some limitations are fixed, migrating `NEUT` to a modern, actively maintained `Pythia` version would likely remove legacy constraints, prevent inconsistencies such as the τ-mass mismatch discussed earlier, and substantially simplify debugging and validation.

In addition, sustained effort toward maintaining, restoring, and rigorously validating the existing code base is a prerequisite for the reliable implementation of new and increasingly complex physics models.

Despite the safeguards and corrections introduced in this work, occasional segmentation faults persist for reasons that are not yet fully understood. This further underscores the need for systematic code modernization, improved diagnostics, and comprehensive, automated testing[2].

[2] Addendum: As Super Kamiokande (SK) uses a modified or wrapped version of `NEUT`, these changes should also be migrated. Consequently, some of the limitations discussed in this chapter may already have been resolved. However, since these modifications have not been integrated into the main program, they could not be considered in this thesis. Furthermore, the changes discussed in section A.1 and subsection A.3.1 are under discussion regarding their permanent inclusion.

B. Tables

Process name	NEUT-Mode
CCQE/NCEL	$1, 51, 52,$ $-1, -51, -52$
2p2h/3p3h/MEC	$2, -2$
RES	$11, 12, 13, 17, 22, 23,$ $31, 32, 33, 34, 38, 39, 42, 43, 44, 45$ $-11, -12, -13, -17, -22, -23$ $-31, -32, -33, -34, -38, -39, -42, -44, -45$
DIF	$15, 35, -15, -35$
COH	$16, 36, -16, -36$
DIS	$21, 26, 41, 46, -21, -26, -41, -46$

Table B.1.: Mapping of NEUT-Modes onto gSeaGen(GENIE) modes. The definition of the different modes can be seen in [37]. Modes with $|\text{mode}| < 30$ are CC and NC otherwise.

Channel	km3neut	gSeaGen
ν_e	17 199 760	13 202 397
$\bar{\nu}_e$	14 975 398	13 203 638
ν_μ	3 363 503	1 424 581
$\bar{\nu}_\mu$	2 315 505	1 475 435
ν_τ	1 222 211	1 324 418
$\bar{\nu}_\tau$	1 095 396	1 350 770
ν_{NC}	13 647 500	13 199 675
$\bar{\nu}_{\text{NC}}$	11 209 613	13 203 794

Table B.2.: Total number of generated events entering the analysis at generator level.

Channel	Number of events per run	`km3neut` γ	`gSeaGen`γ
ν_e	22140	3.335836	2.335836
$\bar{\nu}_e$	6946	3.239740	2.239740
ν_μ	697901	2.903403	1.903403
$\bar{\nu}_\mu$	259012	2.903403	1.903403
ν_τ	542	3.764765	2.764765
$\bar{\nu}_\tau$	352	3.948949	2.948949
ν_{NC}	23697	3.087588	2.087588
$\bar{\nu}_{\mathrm{NC}}$	10248	3.087588	2.087588

Table B.3.: Generated number of neutrino events per run generated with `km3neut`, and `gSeaGen` together with the corresponding spectral indices γ used in the generator stage of the pipeline for $1 < E_\nu < 100$.

Table B.4.: Cross sections for different neutrino and antineutrino interaction modes at 0.6 GeV and 10 GeV on Oxygen in pb per Nucleon. Antineutrino cross sections are shown in parentheses . Taken from [37]

Mode	Reaction	σ 0.6 GeV	σ 10 GeV
± 1	CCQE (1p1h)	0.76 (0.20)	0.95 (0.85)
± 2	2p2h	0.03 (0.01)	0.08 (0.08)
11	CCRes $1\pi^+$	0.15 (Not Available (N.A.))	0.77 (N.A.)
-11	CCRes $1\pi^-$	N.A. (0.02)	N.A. (0.63)
± 12	CCRes $1\pi^0$	0.04 (0.01)	0.39 (0.31)
13	CCRes $1\pi^+$	0.03 (N.A.)	0.52 (N.A.)
-13	CCRes $1\pi^-$	N.A. (0.005)	N.A. (0.41)
15	CCDif $1\pi^+$	Below Threshold (B.T.) (N.A.)	0.03 (N.A.)
-15	CCDif $1\pi^-$	B.T. (N.A.)	0.03 (N.A.)
16	CCCoh $1\pi^+$	0.001 (N.A.)	0.04 (N.A.)
-16	CCCoh $1\pi^-$	N.A. (0.001)	N.A. (0.04)
± 17	CCRes 1γ	0.0002 (3×10^{-5})	0.002 (0.001)
± 21	CCNπ	B.T. (B.T.)	0.85 (0.62)
± 22	CCRes $1\eta^0$	B.T. (B.T.)	0.19 (0.14)
23	CCRes $1K^0$	B.T. (N.A.)	0.06 (N.A.)
-23	CCRes $1K^+$	N.A. (B.T.)	N.A. (0.03)
± 26	CCDIS	B.T. (B.T.)	4.53 (1.30)
± 31	NCRes $1\pi^0$	0.03 (0.009)	0.15 (0.13)
± 32	NCRes $1\pi^0$	0.03 (0.009)	0.15 (0.12)
± 33	NCRes $1\pi^-$	0.02 (0.005)	0.13 (0.11)
± 34	NCRes $1\pi^+$	0.02 (0.005)	0.12 (0.10)
± 35	NCDif $1\pi^0$	B.T. (B.T.)	0.01 (0.01)
± 36	NCCoh $1\pi^+$	0.001 (0.001)	0.02 (0.02)
± 38	NCRes 1γ	0.0002 (6×10^{-5})	0.001 (0.0008)
± 39	NCRes 1γ	0.0002 (6×10^{-5})	0.0009 (0.0008)
± 41	NCNπ	0.0002 (3×10^{-5})	0.25 (0.23)
± 42	NCRes $1\eta^0$	B.T. (B.T.)	0.04 (0.03)
± 43	NCRes $1\eta^0$	B.T. (B.T.)	0.03 (0.02)
± 44	NCRes $1K^0$	B.T. (B.T.)	0.01 (0.007)
± 45	NCRes $1K^+$	B.T. (B.T.)	0.009 (0.007)
± 46	NCDIS	B.T. (B.T.)	1.37 (0.49)
± 51	NCEL (1p1h)	0.13 (0.05)	0.16 (0.16)
± 52	NCEL (1p1h)	0.16 (0.06)	0.21 (0.19)

Table B.5.: Cross sections predictions by NEUT 6 for different neutrino and antineutrino interaction modes at 0.6 GeV and 10 GeV on Oxygen in pb per Nucleon. Antineutrino cross sections are shown in parentheses.

Mode	Reaction	σ 0.6 GeV	σ 10 GeV
±1	CCQE (1p1h)	0.379225 (0.086825)	0.477722 (0.406622)
±2	2p2h	0.0500635 (0.0149485)	0.109777 (0.101192)
11	CCRes $1\pi^+$	0.0721025 (N.A.)	0.382639 (N.A.)
-11	CCRes $1\pi^-$	N.A. (0.0085202)	N.A. (0.316227)
±12	CCRes $1\pi^0$	0.0204746 (0.00262283)	0.195819 (0.158159)
13	CCRes $1\pi^+$	0.0167951 (N.A.)	0.258648 (N.A.)
-13	CCRes $1\pi^-$	N.A. (0.00235294)	N.A. (0.204252)
15	CCDif $1\pi^+$	N.A. (N.A.)	N.A. (N.A.)
-15	CCDif $1\pi^-$	N.A. (N.A.)	N.A. (N.A.)
16	CCCoh $1\pi^+$	0.00146261 (N.A.)	0.0455568 (N.A.)
-16	CCCoh $1\pi^-$	N.A. (0.00146261)	N.A. (0.0455568)
±17	CCRes 1γ	9.60735e−05 (1.72531e−05)	0.00082882 (0.000657545)
±21	CCNπ	B.T. (B.T.)	0.89223 (0.60147)
±22	CCRes $1\eta^0$	B.T. (B.T.)	0.0953185 (0.0676535)
23	CCRes $1K^0$	B.T. (N.A.)	0.0285137 (N.A.)
-23	CCRes $1K^+$	N.A. (B.T.)	N.A. (0.0153343)
±26	CCDIS	B.T. (B.T.)	4.74256 (1.28229)
±31	NCRes $1\pi^0$	0.0153151 (0.004284)	0.0748825 (0.0631795)
±32	NCRes $1\pi^0$	0.0153118 (0.00428419)	0.073311 (0.06223)
±33	NCRes $1\pi^-$	0.00913375 (0.00242992)	0.0630675 (0.05263)
±34	NCRes $1\pi^+$	0.0091262 (0.00243099)	0.0607895 (0.0511975)
±35	NCDif $1\pi^0$	N.A. (N.A.)	N.A. (N.A.)
±36	NCCoh $1\pi^+$	0.00132283 (0.00132283)	0.0247466 (0.0247466)
±38	NCRes 1γ	8.36209e−05 (2.97011e−05)	0.000483723 (0.00041069)
±39	NCRes 1γ	8.36073e−05 (2.96956e−05)	0.000473998 (0.00041244)
±41	NCNπ	0.00025 (5e−05)	0.30599 (0.21263)
±42	NCRes $1\eta^0$	B.T. (B.T.)	0.0183686 (0.0133565)
±43	NCRes $1\eta^0$	B.T. (B.T.)	0.0149589 (0.0122244)
±44	NCRes $1K^0$	B.T. (B.T.)	0.00573805 (0.00333558)
±45	NCRes $1K^+$	B.T. (B.T.)	0.00468741 (0.00339886)
±46	NCDIS	B.T. (B.T.)	1.54509 (0.53726)
±51	NCEL (1p1h)	0.07885 (0.0293)	0.10235 (0.09075)
±52	NCEL (1p1h)	0.059875 (0.024075)	0.07755 (0.06925)

C. Cross Sections

C.1. Comparison NEUT 5.5 and NEUT 6

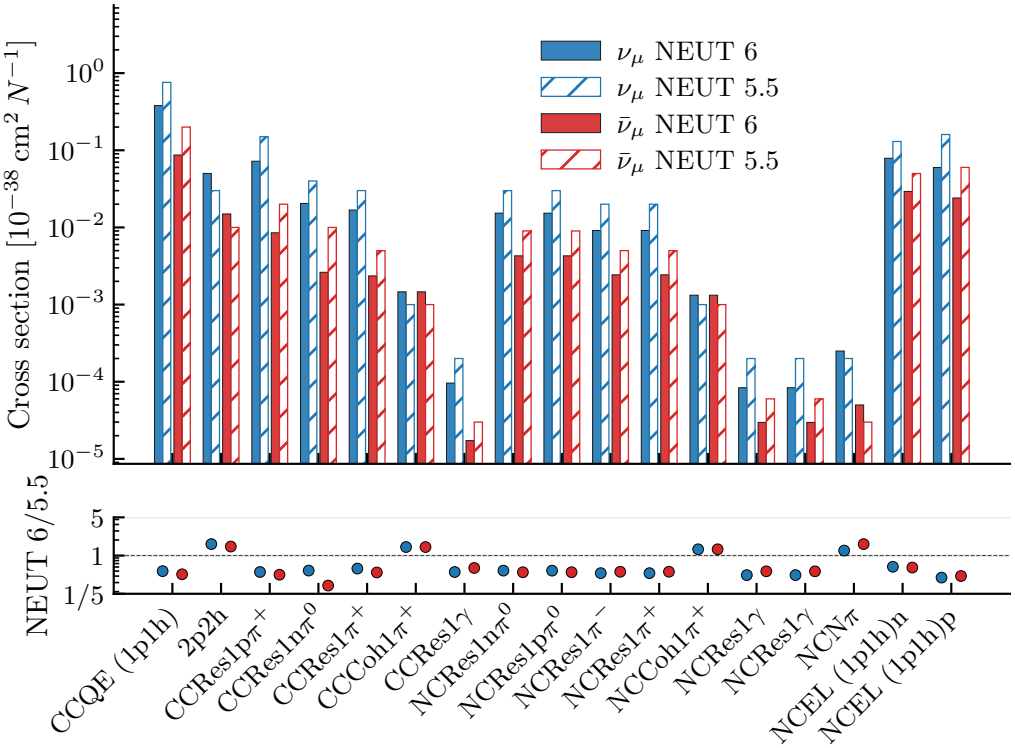

Figure C.1.: Comparison of NEUT 5.5 and NEUT 6 cross sections for ν_μ and $\bar{\nu}_\mu$ interactions on oxygen at $E_\nu = 0.6\,\text{GeV}$. The NEUT 5.5 cross sections are taken from [37].

The cross sections predicted by NEUT 5.5 and NEUT 6 show systematic and channel-dependent differences that become apparent when the reference values from [37] (Tables 1 and 2) are compared with the recalculated results obtained using NEUT 6. For interactions on ^{16}O at 0.6 GeV and 10 GeV for both ν_μ and $\bar{\nu}_\mu$, the resulting cross sections can be contrasted directly with the published NEUT 5.5 values. The graphical comparison is given in Figure C.1 for 0.6 GeV and Figure C.2 for 10 GeV, while the

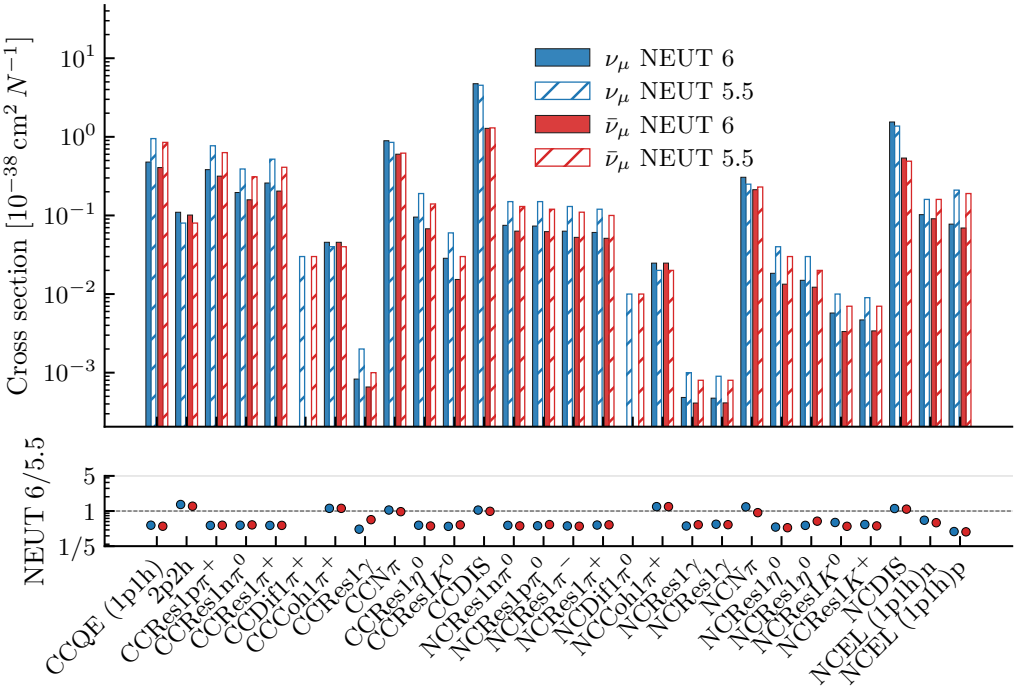

Figure C.2.: Comparison of NEUT 5.5 and NEUT 6 cross sections for ν_μ and $\bar{\nu}_\mu$ interactions on oxygen at $E_\nu = 10\,\text{GeV}$. The NEUT 5.5 cross sections are taken from [37].

numerical reference data and the updated NEUT 6 predictions are summarized in Table B.4 and Table B.5, respectively.

At 0.6 GeV the transition from NEUT 5.5 to NEUT 6 generally lowers the predicted interaction rates, most notably for CCQE, RES, CC and NC single-pion production, and Neutral Current Elastic (NCEL). A few modes, however, increase: the two particles-two holes (2p2h) component becomes larger, Coherent (COH) production in both CC and NC is slightly enhanced, and the CCSIS channels (the $CCN\pi$ sector) rise relative to the older release. The growth of 2p2h is consistent with the updated treatment in NEUT in which multi-nucleon strength beyond the two-body topology, including effective three particles-three holes (3p3h) contributions, is incorporated into the 2p2h model. At 10 GeV the global pattern remains similar but includes additional structural revisions. The elimination of the Diffractive (DIF) channels in NEUT 6 removes contributions that were still present in NEUT 5.5. The RES channels again decrease, while 2p2h, COH, and CCSIS terms exhibit moderate

increases. In the deep-inelastic region the DIS cross sections grow slightly for both neutrinos and antineutrinos, indicating refinements of the hadronization model at higher energies. Neutral-current channels follow analogous trends, with weaker RES contributions, mildly larger COH rates, and stable or slightly increased DIS yields. Overall the migration from `NEUT` 5.5 to `NEUT` 6 suppresses the RES sector, enhances multi-nucleon and coherent components, updates the SIS description in the $N\pi$ region, and yields a small upward shift in the high-energy DIS regime.

For oscillation analyses the updated cross sections influence rates, final-state composition, and neutrino-energy reconstruction. In the T2K domain around 0.6 GeV the reduced CCQE and RES strengths combined with the enhanced 2p2h component alter the balance between CCQE-like and non-CCQE-like processes, modifying reconstructed spectra and thus affecting extractions of Δm^2_{32} and $\sin^2\theta_{23}$. For ORCA, which operates at multi-GeV energies where DIS dominates, the impact are expected to have only a slight impact, as the slight DIS increase and suppressed RES contributions primarily adjust hadronic-shower modeling and flavor composition.

C.2. Cross Section Plots

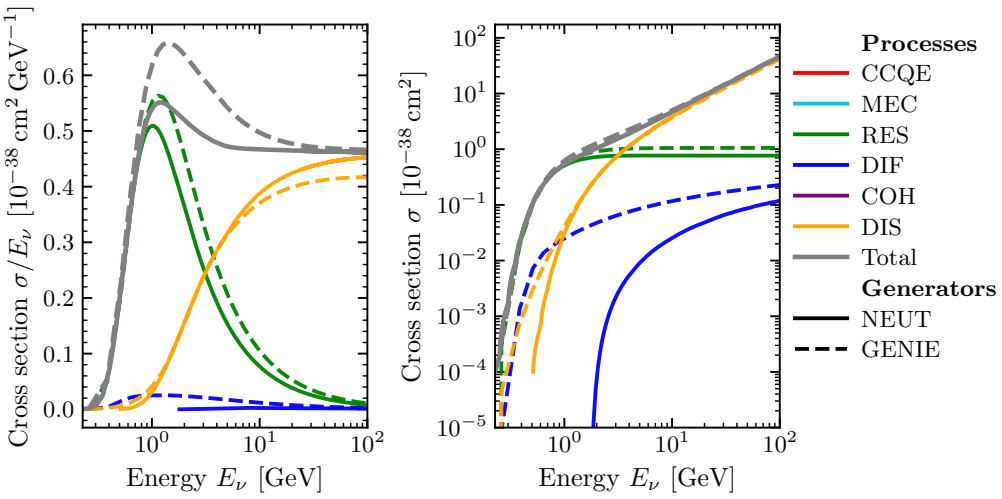

Figure C.3.: Total charged-current cross section for electron neutrinos on hydrogen. Left: σ/E_ν in $10^{-38}\,\mathrm{cm}^2\,\mathrm{GeV}^{-1}$ versus E_ν in GeV. Right: σ in $10^{-38}\,\mathrm{cm}^2$ versus E_ν in GeV (logarithmic y-axis). The curves show the contributions from the different interaction categories and their sum, comparing `NEUT` (solid) and GENIE (dashed).

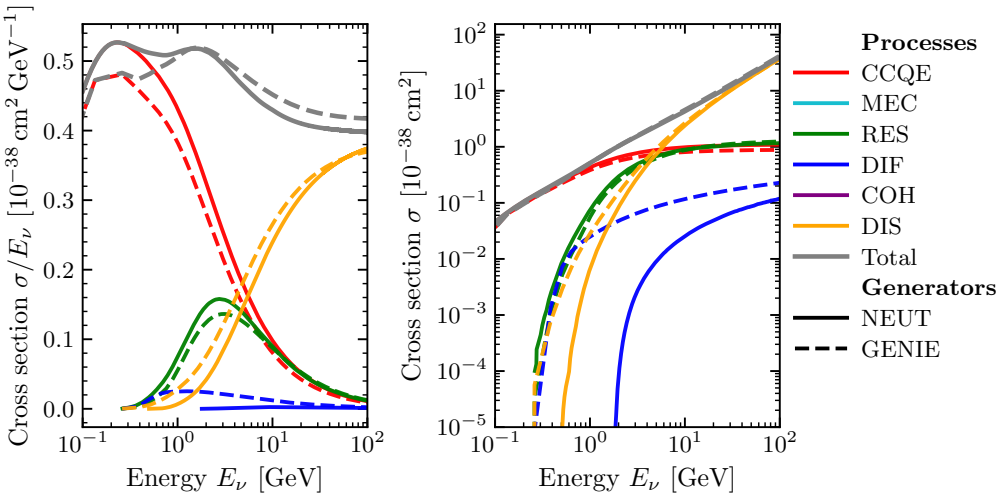

Figure C.4.: Total charged-current cross section for electron antineutrinos on hydrogen. Left: σ/E_ν in $10^{-38}\,\mathrm{cm}^2\,\mathrm{GeV}^{-1}$ versus E_ν in GeV. Right: σ in $10^{-38}\,\mathrm{cm}^2$ versus E_ν in GeV (logarithmic y-axis). The curves show the contributions from the different interaction categories and their sum, comparing `NEUT` (solid) and GENIE (dashed).

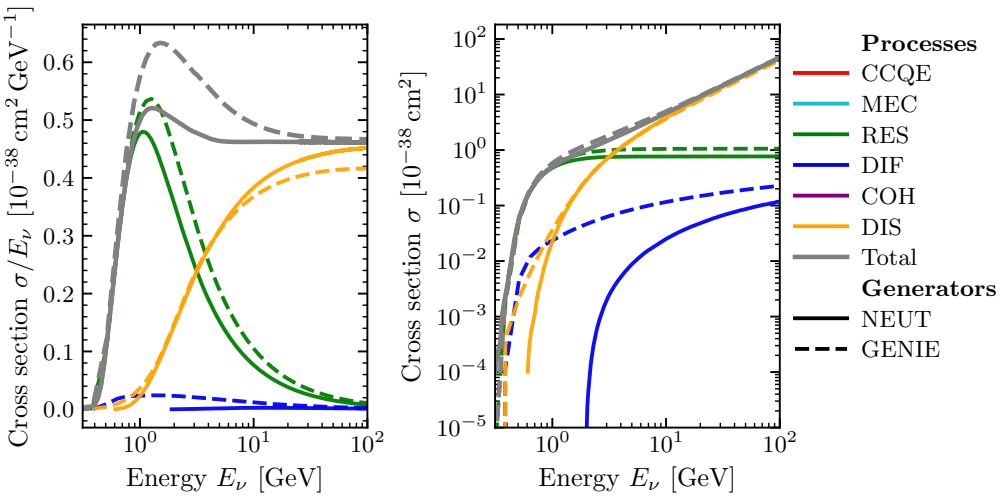

Figure C.5.: Total charged-current cross section for muon neutrinos on hydrogen. Left: σ/E_ν in $10^{-38}\,\mathrm{cm}^2\,\mathrm{GeV}^{-1}$ versus E_ν in GeV. Right: σ in $10^{-38}\,\mathrm{cm}^2$ versus E_ν in GeV (logarithmic y-axis). The curves show the contributions from the different interaction categories and their sum, comparing `NEUT` (solid) and GENIE (dashed).

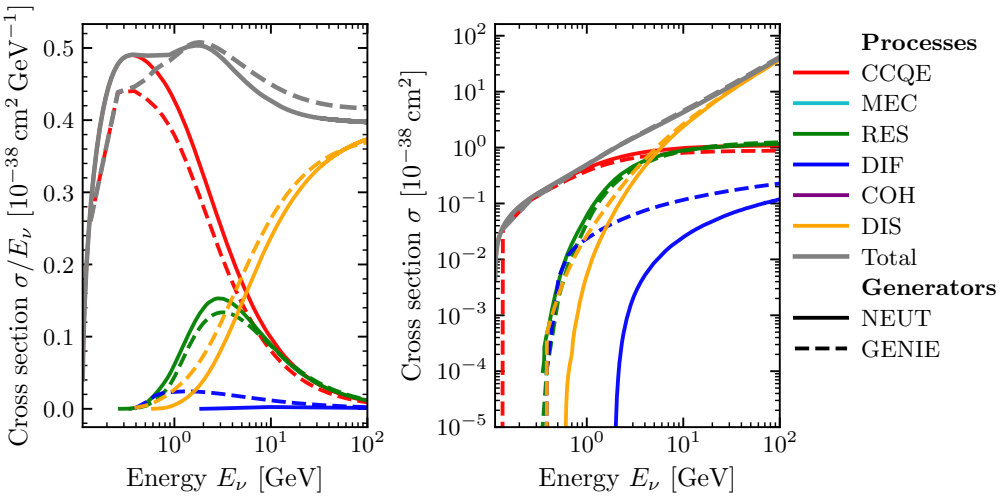

Figure C.6.: Total charged-current cross section for muon antineutrinos on hydrogen. Left: σ/E_ν in $10^{-38}\,\mathrm{cm}^2\,\mathrm{GeV}^{-1}$ versus E_ν in GeV. Right: σ in $10^{-38}\,\mathrm{cm}^2$ versus E_ν in GeV (logarithmic y-axis). The curves show the contributions from the different interaction categories and their sum, comparing `NEUT` (solid) and GENIE (dashed).

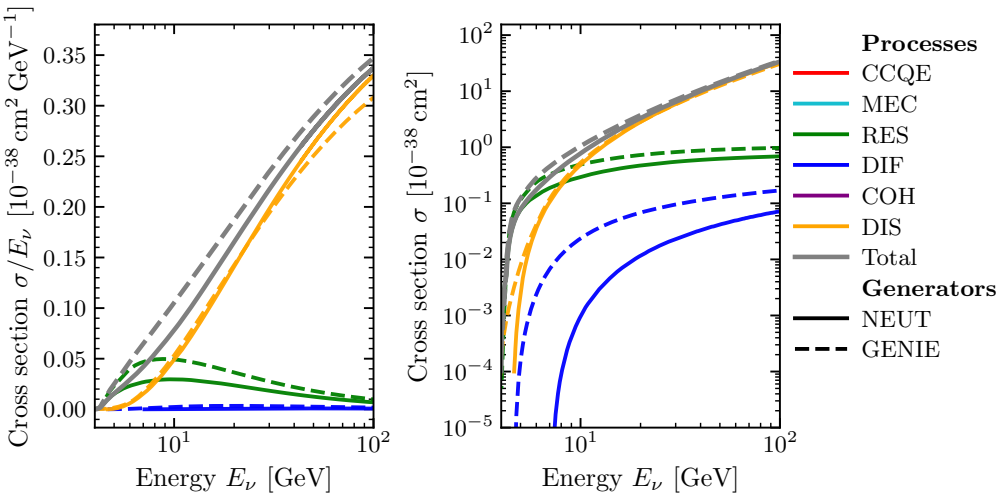

Figure C.7.: Total charged-current cross section for tau neutrinos on hydrogen. Left: σ/E_ν in $10^{-38}\,\mathrm{cm}^2\,\mathrm{GeV}^{-1}$ versus E_ν in GeV. Right: σ in $10^{-38}\,\mathrm{cm}^2$ versus E_ν in GeV (logarithmic y-axis). The curves show the contributions from the different interaction categories and their sum, comparing `NEUT` (solid) and GENIE (dashed).

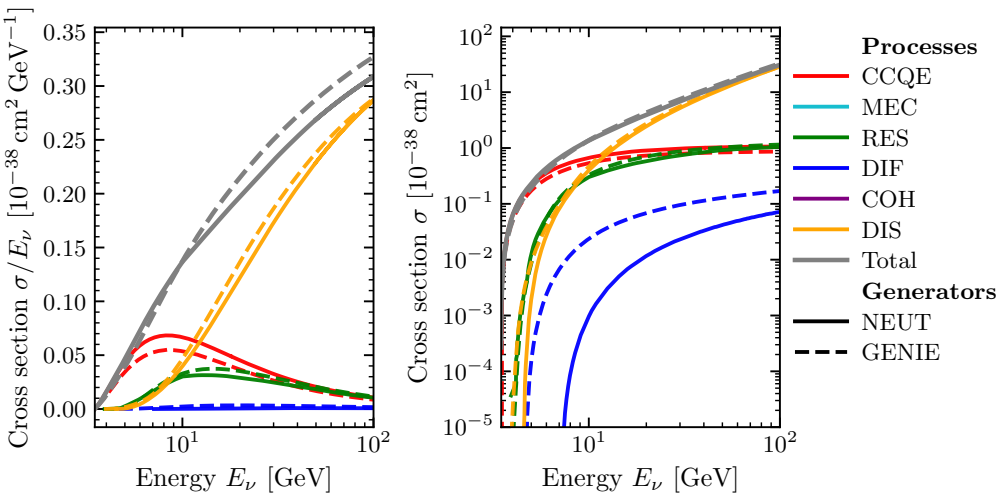

Figure C.8.: Total charged-current cross section for tau antineutrinos on hydrogen. Left: σ/E_ν in $10^{-38}\,\mathrm{cm}^2\,\mathrm{GeV}^{-1}$ versus E_ν in GeV. Right: σ in $10^{-38}\,\mathrm{cm}^2$ versus E_ν in GeV (logarithmic y-axis). The curves show the contributions from the different interaction categories and their sum, comparing `NEUT` (solid) and GENIE (dashed).

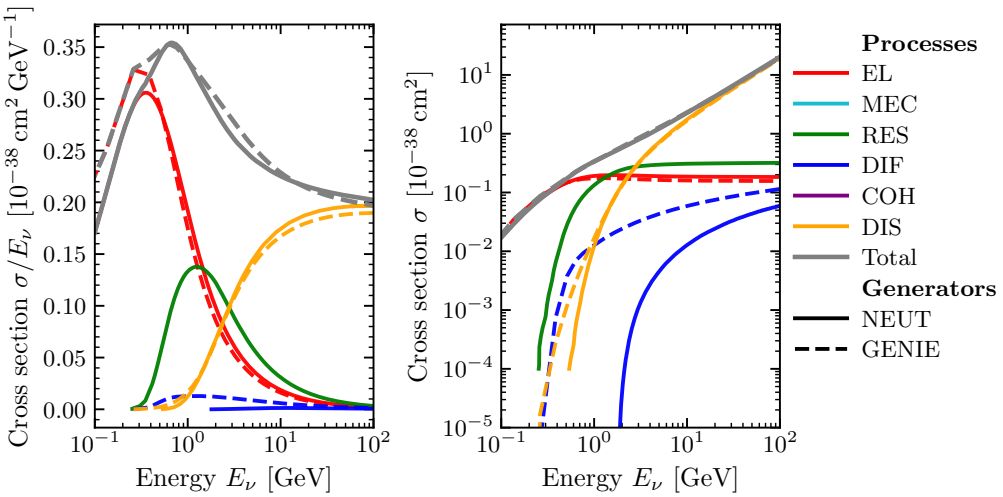

Figure C.9.: Total neutral-current cross section for neutrinos on hydrogen. Left: σ/E_ν in $10^{-38}\,\mathrm{cm}^2\,\mathrm{GeV}^{-1}$ versus E_ν in GeV. Right: σ in $10^{-38}\,\mathrm{cm}^2$ versus E_ν in GeV (logarithmic y-axis). The curves show the contributions from the different interaction categories and their sum, comparing `NEUT` (solid) and GENIE (dashed).

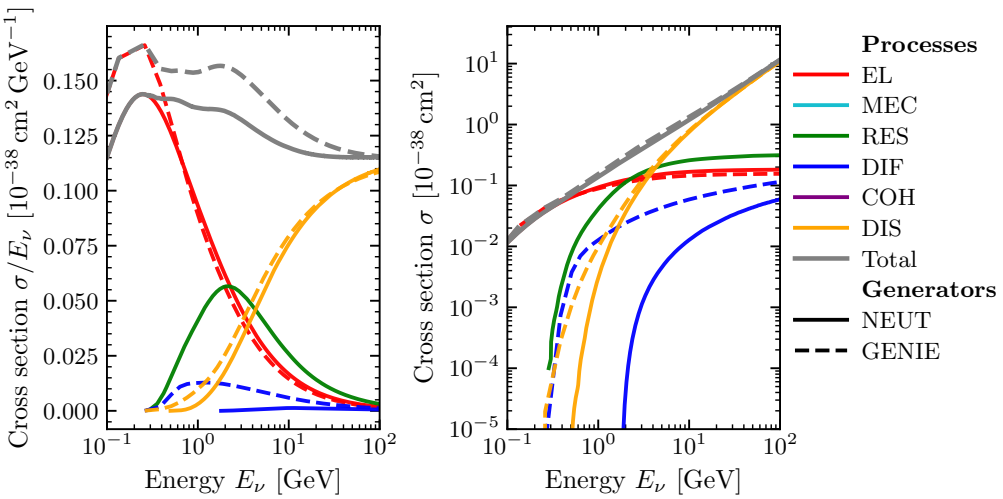

Figure C.10.: Total neutral-current cross section for antineutrinos on hydrogen. Left: σ/E_ν in $10^{-38}\,\mathrm{cm}^2\,\mathrm{GeV}^{-1}$ versus E_ν in GeV. Right: σ in $10^{-38}\,\mathrm{cm}^2$ versus E_ν in GeV (logarithmic y-axis). The curves show the contributions from the different interaction categories and their sum, comparing `NEUT` (solid) and GENIE (dashed).

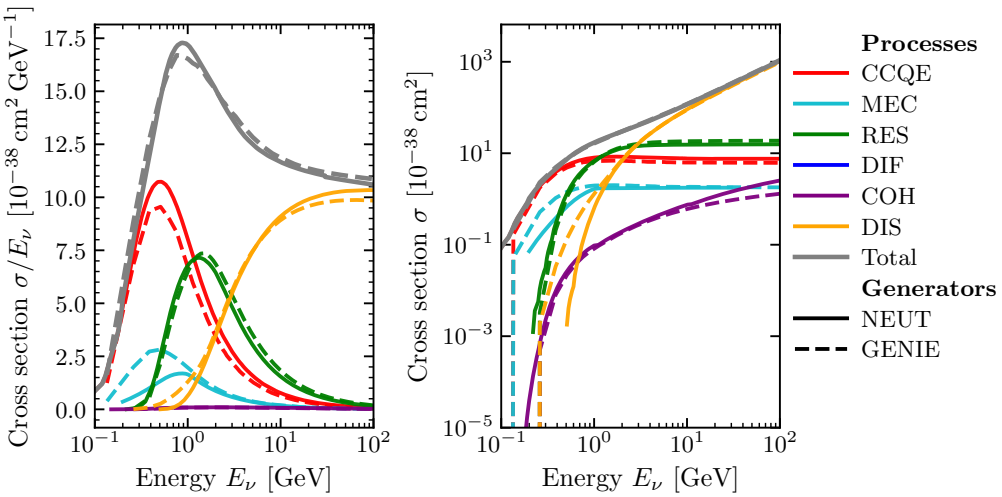

Figure C.11.: Total charged-current cross section per nucleon for electron neutrinos on oxygen. Left: σ/E_ν in $10^{-38}\,\mathrm{cm}^2\,\mathrm{GeV}^{-1}$ versus E_ν in GeV. Right: σ in $10^{-38}\,\mathrm{cm}^2$ versus E_ν in GeV (logarithmic y-axis). The curves show the contributions from the different interaction categories and their sum, comparing `NEUT` (solid) and GENIE (dashed).

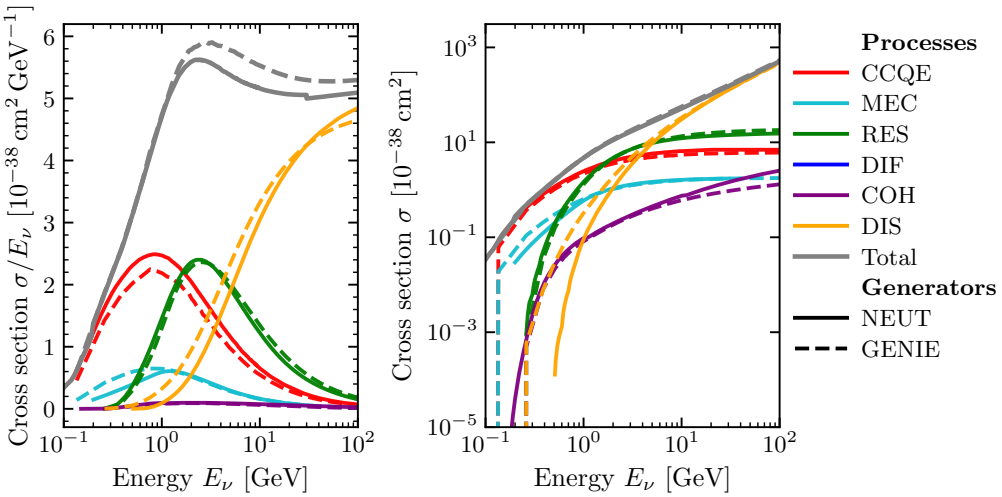

Figure C.12.: Total charged-current cross section per nucleon for electron antineutrinos on oxygen. Left: σ/E_ν in $10^{-38}\,\mathrm{cm}^2\,\mathrm{GeV}^{-1}$ versus E_ν in GeV. Right: σ in $10^{-38}\,\mathrm{cm}^2$ versus E_ν in GeV (logarithmic y-axis). The curves show the contributions from the different interaction categories and their sum, comparing `NEUT` (solid) and GENIE (dashed).

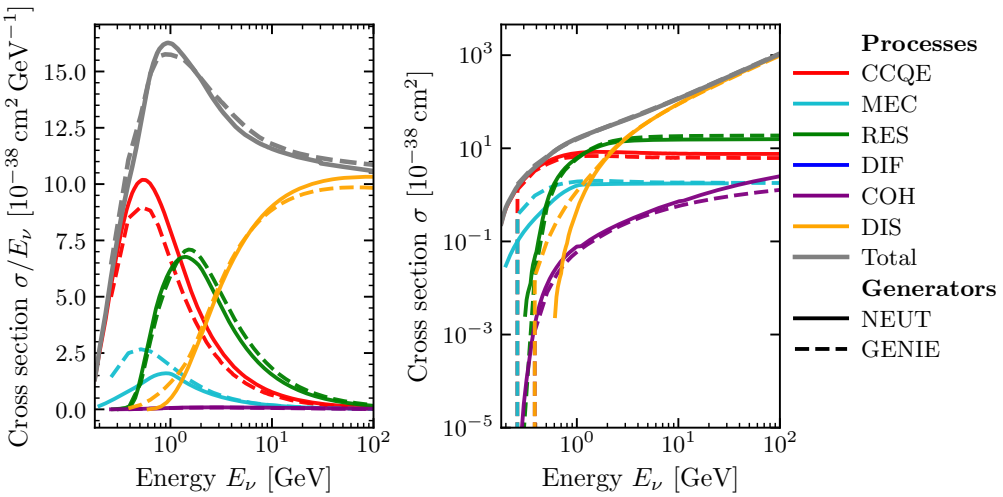

Figure C.13.: Total charged-current cross section per nucleon for muon neutrinos on oxygen. Left: σ/E_ν in $10^{-38}\,\mathrm{cm}^2\,\mathrm{GeV}^{-1}$ versus E_ν in GeV. Right: σ in $10^{-38}\,\mathrm{cm}^2$ versus E_ν in GeV (logarithmic y-axis). The curves show the contributions from the different interaction categories and their sum, comparing `NEUT` (solid) and GENIE (dashed).

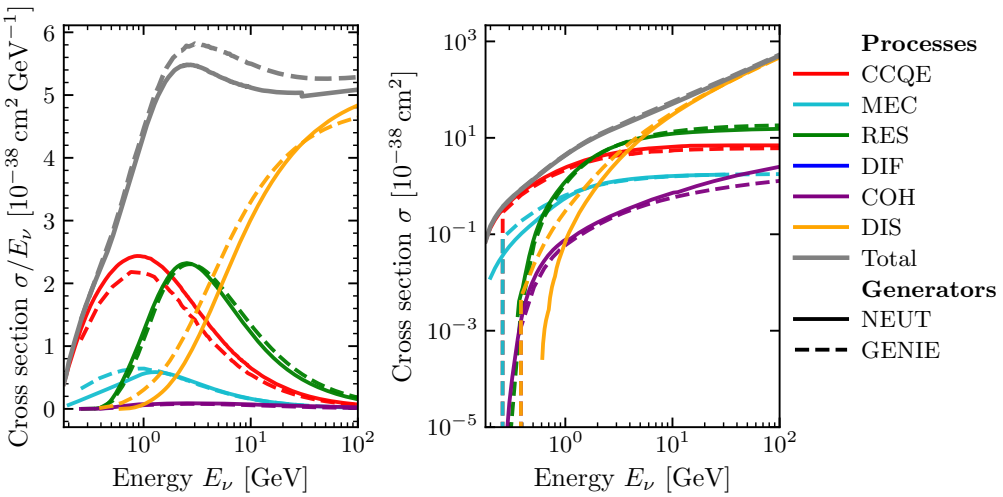

Figure C.14.: Total charged-current cross section per nucleon for muon antineutrinos on oxygen. Left: σ/E_ν in $10^{-38}\,\mathrm{cm}^2\,\mathrm{GeV}^{-1}$ versus E_ν in GeV. Right: σ in $10^{-38}\,\mathrm{cm}^2$ versus E_ν in GeV (logarithmic y-axis). The curves show the contributions from the different interaction categories and their sum, comparing `NEUT` (solid) and GENIE (dashed).

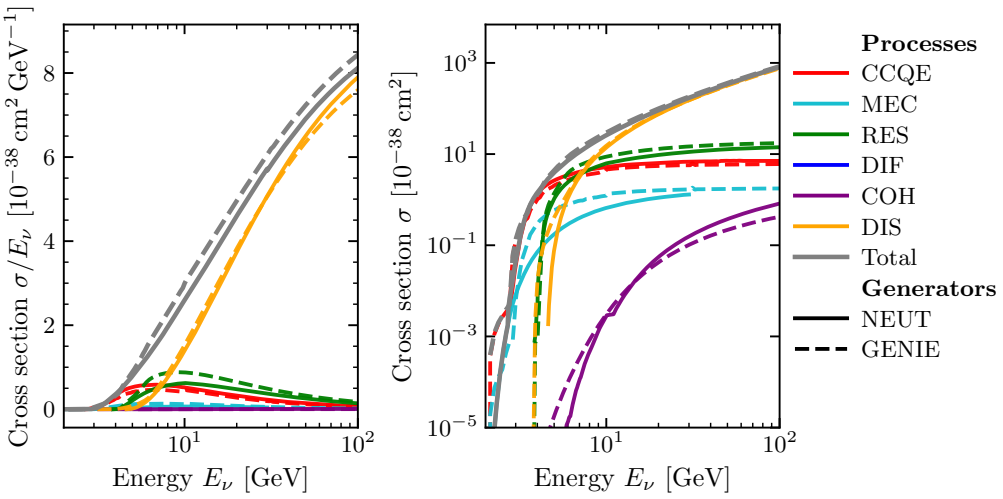

Figure C.15.: Total charged-current cross section per nucleon for tau neutrinos on oxygen. Left: σ/E_ν in $10^{-38}\,\mathrm{cm}^2\,\mathrm{GeV}^{-1}$ versus E_ν in GeV. Right: σ in $10^{-38}\,\mathrm{cm}^2$ versus E_ν in GeV (logarithmic y-axis). The curves show the contributions from the different interaction categories and their sum, comparing `NEUT` (solid) and GENIE (dashed).

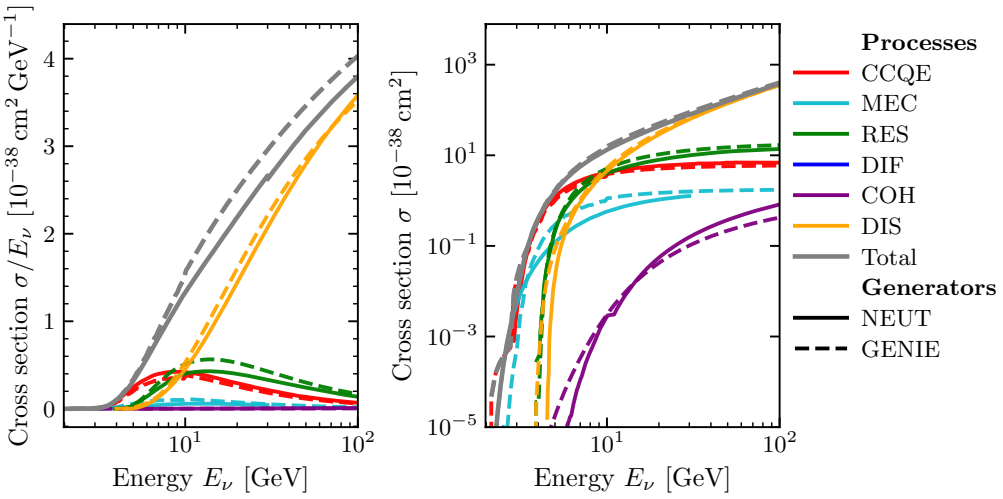

Figure C.16.: Total charged-current cross section per nucleon for tau antineutrinos on oxygen. Left: σ/E_ν in $10^{-38}\,\mathrm{cm}^2\,\mathrm{GeV}^{-1}$ versus E_ν in GeV. Right: σ in $10^{-38}\,\mathrm{cm}^2$ versus E_ν in GeV (logarithmic y-axis). The curves show the contributions from the different interaction categories and their sum, comparing `NEUT` (solid) and GENIE (dashed).

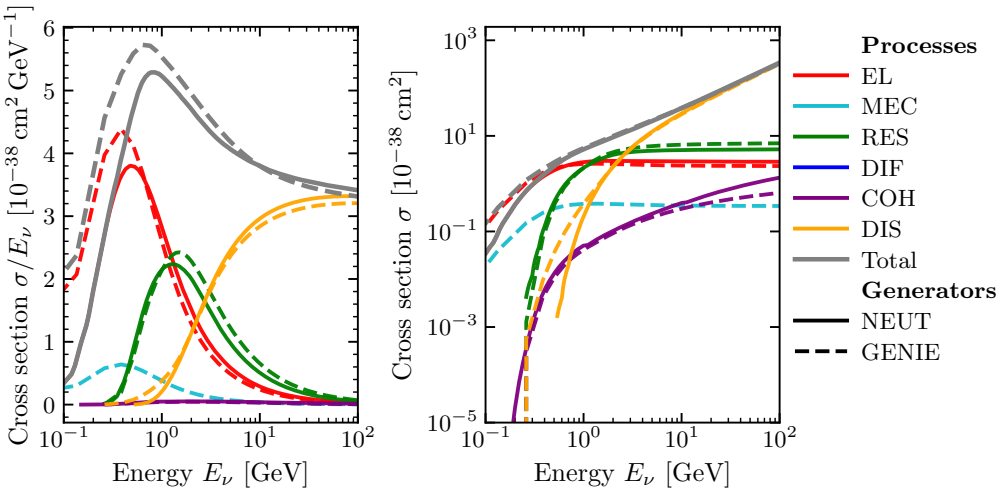

Figure C.17.: Total neutral-current cross section per nucleon for neutrinos on oxygen. Left: σ/E_ν in $10^{-38}\,\mathrm{cm}^2\,\mathrm{GeV}^{-1}$ versus E_ν in GeV. Right: σ in $10^{-38}\,\mathrm{cm}^2$ versus E_ν in GeV (logarithmic y-axis). The curves show the contributions from the different interaction categories and their sum, comparing `NEUT` (solid) and GENIE (dashed).

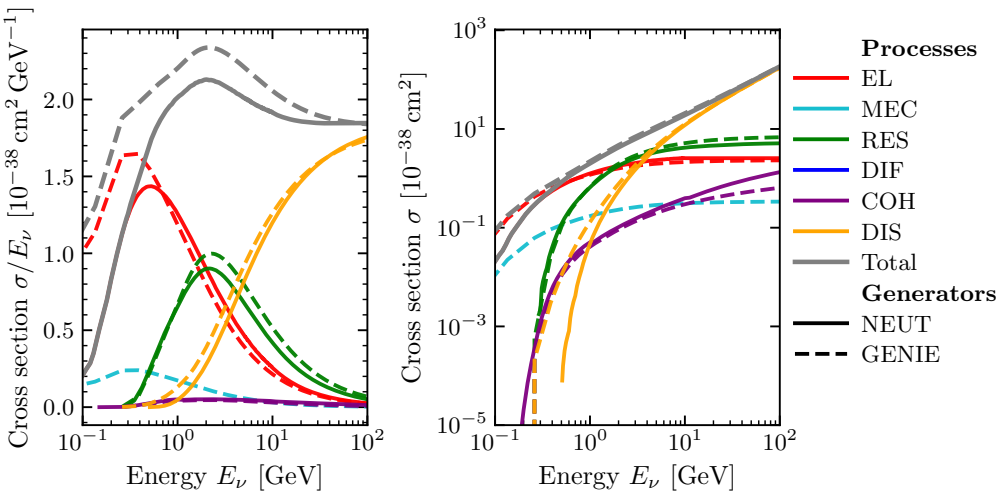

Figure C.18.: Total neutral-current cross section per nucleon for antineutrinos on oxygen. Left: σ/E_ν in $10^{-38}\,\mathrm{cm}^2\,\mathrm{GeV}^{-1}$ versus E_ν in GeV. Right: σ in $10^{-38}\,\mathrm{cm}^2$ versus E_ν in GeV (logarithmic y-axis). The curves show the contributions from the different interaction categories and their sum, comparing `NEUT` (solid) and GENIE (dashed).

Acknowledgements

I would like to thank my supervisors, Dr. Thomas Eberl and Dr. Rodrigo Garcia Ruiz, for giving me the opportunity to work on this thesis and for their guidance and continuous support throughout the project. My sincere gratitude also goes to the NEUT developers, in particular Dr. Luke Pickering and Prof. Yoshinari Hayato, for enabling access to NEUT and for their assistance.

I am grateful to Prof. Dr. Claudio Kopper for the opportunity to present this work at the KM3NeT Collaboration Meeting in Valencia. Essential support with `Snakemake` and the KM3NeT Monte Carlo pipeline was provided by Dr. Kay Graf and Lukas Hennig, which made large parts of this work possible. Many helpful discussions and continued support with the KM3NeT infrastructure came from Tamás Gál and Dr. Jutta Schnabel. I also thank Dr. Johannes Schäfer for his assistance with the high-performance cluster and the ECAP infrastructure.

My sincere thanks go to Dr. Carla Distefano and Johannes Schumann for their help and for patiently answering numerous questions during the continued development of the external generator interface for `gSeaGen`. In particular, Johannes Schumann laid the groundwork that allowed me to further develop and extend the interface.

Finally, I would like to thank my office colleagues Robert Petri and Sebastian Schindler for the many discussions, their encouragement, and for creating a pleasant and motivating working environment.

Declaration of Originality

I, Frederik Andersen, student registration number: 22646501, hereby confirm that I completed the submitted work independently and without the unauthorized assistance of third parties and without the use of undisclosed and, in particular, unauthorized aids. This work has not been previously submitted in its current form or in a similar form to any other examination authorities and has not been accepted as part of an examination by any other examination authority.

Where the wording has been taken from other people's work or ideas, this has been properly acknowledged and referenced. This also applies to drawings, sketches, diagrams and sources from the Internet.

In particular, I am aware that the use of artificial intelligence is forbidden unless its use an aid has been expressly permitted by the examiner. This applies in particular to chatbots (such as ChatGPT) and such programs in general that can complete the tasks of the examination or parts thereof on my behalf.

Any infringements of the above rules constitute fraud or attempted fraud and shall lead to the examination being graded fail (nicht bestanden).

Place, Date	Signature